



**DETECTION OF RESIDUAL STRESS IN SiC
MEMS USING μ -RAMAN SPECTROSCOPY**

THESIS

John C. Zingarelli, First Lieutenant, USAF
AFIT/GEO/ENP/05-06

**DEPARTMENT OF THE AIR FORCE
AIR UNIVERSITY**

AIR FORCE INSTITUTE OF TECHNOLOGY

Wright-Patterson Air Force Base, Ohio

APPROVED FOR PUBLIC RELEASE; DISTRIBUTION UNLIMITED

The views expressed in this thesis are those of the author and do not reflect the official policy or position of the United States Air Force, Department of Defense, or the United States Government.

AFIT/GEO/ENP/05-06

DETECTION OF RESIDUAL STRESS IN SiC MEMS USING μ -RAMAN
SPECTROSCOPY

THESIS

Presented to the Faculty

Department of Engineering Physics

Graduate School of Engineering Physics

Air Force Institute of Technology

Air University

Air Education and Training Command

in Partial Fulfillment of the Requirements for the
Degree of Master of Science in Electrical Engineering

John C. Zingarelli, B.S.E.E.

First Lieutenant, USAF

March 2002

APPROVED FOR PUBLIC RELEASE; DISTRIBUTION UNLIMITED

DETECTION OF RESIDUAL STRESS IN SiC MEMS USING μ -RAMAN
SPECTROSCOPY

John C. Zingarelli, BS
First Lieutenant, USAF

Approved:



Michael A. Marciniak (Chairman)

9 Mar 05

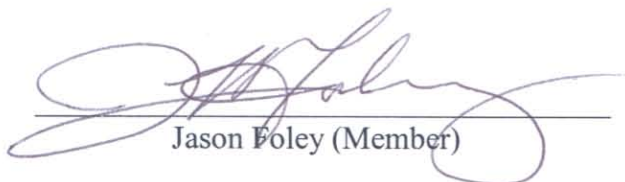
date



LaVern A. Starman (Member)

8 Mar 2005

date



Jason Foley (Member)

7 Mar 2005

date

Abstract

Micro-Raman (μ -Raman) spectroscopy is used to measure residual stress in two silicon carbide (SiC) poly-types: single-crystal, hexagonally symmetric 6H-SiC, and polycrystalline, cubic 3C-SiC thin films deposited on Si substrates. Both are used in micro-electro-mechanical-systems (MEMS). The 6H-SiC structures are bulk micro-machined by back etching a 250- μm -thick, single-crystal 6H-SiC wafer (p-type, 7 $\Omega\text{-cm}$, 3.5° off-axis) to form a 50- μm thick diaphragm. A Wheatstone bridge, patterned of piezoresistive elements, is formed across the membrane from a 5- μm , 6H-SiC (n-type, doped $3.8 \times 10^{18}\text{cm}^{-3}$) epilayer; the output of the bridge is proportional to the flexure of the MEMS diaphragm. For these samples, the μ -Raman spectroscopy is performed using a Renishaw InVia Raman spectrometer with an argon-ion excitation source ($\lambda = 514.5\text{ nm}$, $h\nu = 2.41\text{ eV}$) with an approximate $1\text{-}\mu\text{m}^2$ spot size through the 50x objective. By employing an incorporated piezoelectric stage with submicron positioning capabilities along with the Raman spectral acquisition, spatial scans are performed to reveal areas in the MEMS structures that contain residual stress. Shifts in the transverse optical (TO) Stokes peaks of up to 1 cm^{-1} along the edge of the diaphragm and through the piezoresistors indicate significant material strain induced by the MEMS fabrication process. The phonon deformation potential in both SiC poly-types is measured to quantify the material stress as a function of the shift in the Raman peak position. The line center of the TO Stokes peak is shifted by applying a uniform stress to the sample using a four-point strain fixture and monitoring the applied stress using a strain gauge, while the μ -Raman spectrum is being measured. A spectral analysis code tracks the shift of the Raman peak position with respect to the line center of the Rayleigh peak to account for any thermal drift of the spectrometer during the time of the area scan. 3C-SiC films, with thicknesses ranging from 1.5-5 μm and are deposited by chemical vapor deposition on (100) Si substrates, are also investigated to determine their residual stress via their Raman spectral characteristics. An

ultraviolet excitation source ($\lambda = 325$ nm, $h\nu = 3.82$ eV) is determined to be more effective for the detection of Raman shifts in these thin films than the 514-nm source, do to both resonant Raman effects and since the absorption coefficient in SiC at 300 K at 325 nm is 3660 cm^{-1} , while that at 514 nm is less than 100 cm^{-1} (dependent on doping level). In addition, the Si substrate is less Raman active at 325-nm excitation, leading to a lower relative amplitude than that at 514.5 nm and increasing the signal-to-noise ratio (SNR) of the SiC Raman spectrum. Since SNR is also increased by increasing absorption length, the thicker films ($5.5\text{ }\mu\text{m}$) of the 3C-SiC are preferable for measuring Raman spectra than the thinner films ($1.5\text{ }\mu\text{m}$).

Acknowledgements

The most notable part of my research has been the interaction with so many brilliant and motivated scientists. For the guidance and support making this research possible, I would like to especially thank my advisor Dr. Michael A. Marciniak and Capt LaVern Starman. For the funding and hours of time discussing and analyzing results my appreciation goes to Mr. Jason Foley. For providing samples, materials, data and ideas, I thank Jeff Melzak. Other people I would like to mention who helped me in numerous ways were Capt Tetsuo Kaieda, Jason Reber, John Busbee, David Liptak, Mr. William Fitzgerald Phil Neudack, and Tim Prusnick. Finally and most importantly I would like to thank my wife for her loving support.

John C. Zingarelli

Table of Contents

	Page
Abstract	iv
Acknowledgements	vi
List of Figures	x
List of Tables	xv
List of Abbreviations	xvi
 I. Introduction	 1-1
1.1 Motivation	1-1
1.1.1 Applications: SiC Electronic devices	1-2
1.1.2 Applications: SiC MEMS	1-2
1.2 Current technology limitations	1-4
1.3 Problem Statement and Research Objectives	1-5
1.4 Thesis Organization	1-5
 II. Background Information	 2-1
2.1 μ -Raman Spectroscopy	2-1
2.2 Residual Stress	2-4
2.3 Detection of Residual Stress in poly-Si	2-5
2.4 Background Information on SiC	2-9
2.5 Fabrication of SiC MEMS	2-11
2.6 Crystal Defects of SiC	2-14
2.6.1 Point Defects	2-14
2.6.2 Line Defects	2-15
2.6.3 Area Defects	2-16
2.6.4 Volume Defects	2-16
2.6.5 Micropipes	2-16
2.7 Literature Review	2-17
2.8 Chapter Summary	2-21

	Page
III. Samples	3-1
3.1 NASA crystalline 6H-SiC accelerometer and pressure sensor	3-1
3.1.1 Layout and Function	3-1
3.1.2 Resistivity of the piezoresistors #2 and #4	3-2
3.2 Cree 6H-SiC wafers	3-6
3.3 FLX poly-SiC Thin Films	3-6
3.3.1 1.5- μm SiC on Si	3-7
3.3.2 5.5- μm SiC on Si	3-7
3.3.3 Optical Properties of SiC	3-8
3.4 Chapter Summary	3-9
IV. Equipment and Experiments	4-1
4.1 Probe Station	4-1
4.2 Scanning Electron Microscope	4-2
4.2.1 AMRAY 1810 (1990)	4-3
4.3 Zygo Interferometer	4-4
4.4 InVia Raman Spectrometer	4-4
4.4.1 Spectral Resolution	4-5
4.4.2 Sampling Rate	4-7
4.5 Four-point Strain Fixture	4-8
4.6 Vice	4-9
4.7 P-3 Strain Indicator and Recorder	4-10
4.8 Chapter summary	4-11
V. Results and Data Analysis	5-1
5.1 NASA 550 and 650 6H-SiC MEMS	5-1
5.1.1 Resistance of piezoresistors	5-1
5.1.2 SEM's	5-2
5.1.3 Zygo Interferometer Data	5-4
5.1.4 Raman Spectroscopy on the NASA 550 MEMS	5-6
5.1.5 Phonon Deformation Potential	5-8
5.1.6 Raster Maps of Raman Shift	5-15
5.2 Thin Film poly-SiC	5-20
5.2.1 325-nm versus 514-nm Excitation-Resonant Raman, Resolution and Luminescence	5-20
5.2.2 UV Raman Spectroscopy: Si versus SiC on Si	5-21
5.2.3 Film Thickness – Absorption	5-22

	Page
5.2.4 Substrate Raman Noise	5-23
5.2.5 Stacking Faults in poly-SiC	5-25
5.2.6 Delaminated poly-SiC	5-25
5.3 Chapter Summary	5-27
VI. Conclusions and Recommendations	6-1
6.1 Conclusions	6-1
6.2 Recommendations for Future Work	6-2
Appendix A. Properties of SiC	A-1
Appendix B. Equipment	B-1
Appendix C. Matlab Code	C-1
C.1 Resistivity Program	C-1
C.2 Transmission Program	C-2
C.3 Raman Analysis Program	C-3
Bibliography	BIB-1

List of Figures

Figure		Page
1.1.	Pressure Sensor reported to exhibit stable operation at 500°C . . .	1-3
1.2.	Cross section of a typical gas turbine engine showing atomizer insertion points	1-4
2.1.	Schematic depicting the Raman and Rayleigh scattering of an excitation source due to phonon or vibrational energy present between two atoms.	2-2
2.2.	Energy levels for normal Raman, resonance Raman, and fluorescence spectra.	2-4
2.3.	"Frequency shift of the hydrostatic component for an applied uniaxial stress applied along a 1.5 μm -thick Poly2 cantilever with dimensions of 200 μm -wide by approximately 4000 μm -long." . . .	2-6
2.4.	"Background residual stress profiles for a 100 μm -long by 10 μm -wide unreleased and released fixed-fixed beam. (a) Poly1 beam, (b) Poly2 beam and (c) Poly1-Poly2 stacked beam."	2-7
2.5.	"Analytical stress model for a MEMS fixed-fixed beam."	2-8
2.6.	"Analytical stress profile of a fixed-fixed beam with a uniform load"	2-9
2.7.	Lattice structure of cubic and hexagonal SiC.	2-10
2.8.	Representation of stacking order for 6H-SiC.	2-11
2.9.	"Cross-section schematic if a SiC micromotor fabricated using the MUSIC process"	2-13
2.10.	"SEM micrograph of a SiC salient-pole micromotor fabricated using the MUSIC process."	2-13
2.11.	Point defect. (a) Substitutional impurity. (b) Interstitial impurity. (c) Lattice vacancy. (d) Frenkel-type defect.	2-15
2.12.	(a) Edge and (b) screw dislocations in cubic crystals.	2-15
2.13.	Stacking fault in semiconductor. (a) Intrinsic stacking fault. (b) Extrinsic stacking fault.	2-16
2.14.	Etched micropipe in a SiC diaphragm.	2-17
2.15.	Raman Spectrum of 6H-SiC using 266-nm and 488-nm excitation sources.	2-18
2.16.	Raman spectra, 3C-SiC.	2-19
2.17.	The transversal optical (TO) mode of bulk poly-3C-SiC by Lee <i>et al.</i> [1].	2-20
2.18.	μ -stress maps collected of the epitaxially grown 3C-SiC film by Lee <i>et al.</i> [1].	2-20
2.19.	TO peak in 3C poly-SiC (a) as deposited and (b) after laser annealing at 1700 K.	2-21

Figure		Page
3.1.	(a) Cross-section of 6H-SiC MEMS diaphragm indicating points of stress from a shock. (b) Layout of the resistive elements forming a Wheatstone bridge. (c) Top view of the NASA 600 sample with highlights over the piezoresistive elements.	3-2
3.2.	The resistance of piezoresistors #2 and #4, which are PECVD deposited 6H-SiC strips of 5- μm epitaxial layers (n-type, doped $3.8 \times 10^{18} \text{ cm}^{-3}$) on the top surface of the wafer. The length of the resistors is $l = 400 \mu\text{m}$ and the cross-sectional area is $A = 40\mu\text{m} \times 5\mu\text{m}$. The dopant for the epitaxial layer is N.	3-5
3.3.	Layout and specifications of two Cree 6H-SiC wafers used to determine phonon deformation potentials.	3-6
3.4.	(a) Cross-section of the 1.5 μm thick poly-SiC deposited by low-pressure chemical vapor deposition (LPCVD) on a Si substrate. (b) Microscope image of the top of the FLX micro 1.5- μm poly-SiC on a Si substrate. The comb drive is a metal mask deposited onto the thin film.	3-7
3.5.	(a) A cross-section of the 5.5 μm thick poly-SiC deposited by low-pressure chemical vapor deposition (LPCVD) on a Si substrate. The Si substrate is back-etched to produce a suspended membrane of SiC. (b) Optical micrograph of the top surface of the 5.5 μm thin film. The membrane was fractured during transport and dropped below the support structure revealing the edge of the diaphragm. Intact samples were used for all Raman measurements.	3-8
3.6.	Percent of light transmitted as a function of thickness of SiC by the 325 nm and 512 nm lasers for both 6H and 3C polytypes. 3C-SiC absorption values come from Figures A.1 and A.4. 6H-SiC absorption values come from Figures A.2 and A.3.	3-9
4.1.	Four-point probe station used to measure the resistance of piezoresistive elements.	4-1
4.2.	The text boxes label the measurement taken and the arrows indicate where the probe needle for the resistance measurement was placed on the device.	4-2
4.3.	AMRAY 1810 SEM.	4-3
4.4.	Diagram of the New View Zygo interferometer system.	4-4
4.5.	Diagram of a Renishaw Raman spectrometer.	4-5
4.6.	(a) Raman spectrum of diamond powder using a 325-nm excitation source. (b) Raman peak of diamond powder at 1331 cm^{-1} showing the range between sampling points. (c) Raman spectrum of 6H-SiC using a 514-nm excitation source. (d) LO peak of 6H-SiC a 966 cm^{-1} using a 325-nm excitation source.	4-8
4.7.	(a) Top view of the four-point strain fixture. (b) Sideview of the four-point strain fixture.	4-9
4.8.	Vice setup used to apply stress to a 1-cm x 1-cm square of 6H-SiC with a strain gauge epoxied to the back side and used to measure the phonon deformation potentials.	4-10

Figure		Page
4.9.	Photograph of the P-3 strain indicator and recorder.	4-11
5.1.	(a) SEM of the NASA 550 pressure sensor in packaging at 11.3X magnification. (b) SEM at 33.2X magnification (c) SEM of resistors #2 and #4 at 123X magnification (d) Closeup of resistor #2 where a residual stress was identified using Raman spectroscopy. .	5-3
5.2.	(a) SEM of resistor #3 on the NASA 550 pressure sensor in the location where it crosses the diaphragm. (b) SEM of the NASA 550 pressure sensor showing the location of (a)	5-4
5.3.	An interferogram and a optical micrograph of the resistors #2 and #4 on the NASA 550 sample in a location where isolated residual stress was detected using Raman analysis.	5-5
5.4.	An interferogram and an optical micrograph of resistor # 3 on the NASA 550 sample. Residual stress was identified where the resistor crosses the diaphragm by using Raman spectroscopy.	5-5
5.5.	(a) Raman spectrum of crystalline 6H-SiC with a 514-nm excitation source using the InVia Renishaw spectrometer. (b) Raman spectrum of crystalline 6H-SiC with a 325-nm excitation source.	5-7
5.6.	6H-SiC Raman spectrum from the edge of the NASA 550 pressure sensor.	5-8
5.7.	The top graph shows the line center of the TO2 peak as a function of uniaxial pressure applied normal to the c-axis of 6H-SiC. The bottom graph shows the residuals of the linear least squares fit to the measured data points.	5-10
5.8.	The top graph shows the line center of the TO1 peak as a function of uniaxial pressure applied normal to the c-axis of 6H-SiC. The bottom graph shows the residuals of the linear least squares fit to the measured data points.	5-11
5.9.	(a) Location of line scan on resistor #3. (b) Location of resistor #3 on NASA 550 pressure sensor.	5-12
5.10.	The line center of the TO 1 and TO 2 6H-SiC Raman peaks as a function of position.	5-13
5.11.	The estimated amount of residual stress as a function of position of the line scan shown in Figure 5.9. The estimates were found using phonon deformation potentials for the TO 1 and TO 2 peaks and mapping them to the results shown in Figure 5.10.	5-14
5.12.	Typical Raman spectrum of the 6H-SiC as measured during the determination of the phonon deformation potential. The raised baseline is due to background noise from a piece of foam the sample was placed on.	5-15
5.13.	(a) Micrograph of diaphragm edge through a 20X objective with a coordinate system that matches the raster map location in (c). (b) Micrograph of the NASA 550 pressure sensor depicting the location of the edge of the diaphragm. (c) The residual stress measured using of a raster scan across the edge of the diaphragm.	5-16

Figure		Page
5.14.	(a) Micrograph of resistors #2 and #4 through a 20X objective with a coordinate system that matches the raster map location in (c). (b) Micrograph of the NASA 550 pressure sensor depicting the location of resistors #2 and #4 on the device. (c) The residual stress measured using of a raster scan across resistor #2.	5-17
5.15.	(a) Micrograph of resistors #2 and #4 through a 20X objective with a coordinate system that matches the raster map location in (c). (b) Micrograph of the NASA 550 pressure sensor depicting the location of resistors #2 and #4 on the device. (c) The results of a raster scan across resistor #4 showing the amounts of residual stress in the resistor.	5-18
5.16.	(a) and (b) Zoom in on the defect location on resistor #4 identified by Raman mapping (c) Observation of the identified defect optically by changing the depth of focus on the microscope and recording the image.	5-19
5.17.	The blue spectral lines are from the Raman spectrum of a 1.5- μm poly-SiC layer on a (100) Si substrate measured using a 514-nm excitation source. The red spectral lines are of the same 1.5- μm poly-SiC film with a 325-nm excitation source.	5-21
5.18.	The Raman spectrum of a 1.5- μm poly-SiC on a Si (100) substrate is compared with the Raman spectrum of Si (100) both of which were excited by a 325-nm excitation source.	5-22
5.19.	Raman spectrum of poly-SiC films of thickness 1.5 μm and 5.5 μm using a 325-nm excitation source.	5-23
5.20.	(a) A cross-section of a 5.5- μm poly-SiC thin film grown on a (100) Si substrate. Pyramidal pits of the Si substrate were anisotropically back-etched creating suspended membranes of the poly-SiC (Region 1). Portions of the poly-SiC delaminated revealing the Si substrate (Region 3). (b) The Raman spectrum of the three regions shown in the cross-section (a) using a 325-nm excitation source.	5-24
5.21.	The spectrum of 5.5- μm SiC on Si and SiC on Plexiglas.	5-26
5.22.	The shift of peaks of 5.5- μm poly-SiC as a function of compressive stress	5-27
A.1.	Electron Hall mobility vs. donor density. Used to determine resistivity of 6H-SiC piezoresistors.	A-1
A.2.	Absorption coefficient of 6H-SiC vs photon energy. Use to determine transmission length of 325-nm photons in crystalline 6H-SiC MEMS.	A-2
A.3.	Absorption coefficient of 6H-SiC vs photon energy . Used to determine transmission length of 514-nm photons in crystalline 6H-SiC MEMS.	A-2
A.4.	"Absorption of cubic SiC crystals 1 and 1 (solid) at 300K. Crystal 1 is relatively pure; crystal 2 is strongly n-type (perhaps $10^{19}/cm^3$ donors)"	A-3

Figure		Page
A.5.	Band Structure of 3C-SiC. Important minima of the conduction band and maxima of the valence band.	A-4
B.1.	Four Point Strain Fixture	B-1
B.2.	Parameters of InVia Raman spectrometer configured for the 514-nm excitation source	B-2
B.3.	Parameters of InVia Raman spectrometer configured for the 325-nm excitation source	B-2

List of Tables

Table		Page
2.1.	Raman Shift peak locations for common polytypes of SiC [2] . . .	2-5
2.2.	Material Properties of 3C and 6H SiC at 300K [3]	2-12
4.1.	Renishaw InVia Raman spectrometer advertised capabilities. . . .	4-7
5.1.	Measured resistances of the piezoressitors on the NASA 550 and 650 MEMS sensors with the coresponding standard deviation of the measurements.	5-2
A.1.	Absorption coefficients and depth penetration for 3C-SiC [4] . . .	A-3

List of Abbreviations

Abbreviation	Page
(TO) transverse optical	iv
(SiC) Silicon Carbide	1-1
(MEMS) micro-electrical-mechanical systems	1-1
NASA National Air and Space Administration	1-1
(AFRL/MN) Munitions Directorate Air Force Research Laboratory	1-1
(JFET) junction field-effect transistor	1-2
(MESFET) metal-semiconductor field-effect transistor	1-2
(MOSFET) metal-oxide-semiconductor field-effect transistor	1-2
(CMOS) complementary MOSFET	1-2
(IC's) integrated circuits	1-2
(RF) Radio Frequency	1-3
(Q) Quality factor	1-3
(ARA) Applied Research Associates	1-4
(NDE) Non-Destructive Evaluation	1-5
(IR) Infrared	2-3
(AFIT) Air Force Institute of Technology	2-5
(MUSIC) Multi-User Silicon Carbide	2-12
(MUMPs) Multi-User MEMS Processes	2-12
(DRIE) Deep Reactive Ion Etching	2-12
(CVD) chemical vapor deposition	2-12
(FTO) Folded Transverse Optical	2-17
(FLO) Folded Longitudnal Optical	2-17
(PECVD) Plasma Enhanced Chemical Vapor Deposition	3-2
(N) Nitrogen	3-2
(poly-SiC) polycrystalline 3C-SiC	3-6

Abbreviation	Page
(LPCVD) low-pressure chemical vapor deposition	3-6
(SiO ₂) Silicon Dioxide	3-7
(Si ₃ N ₄) Silicon Nitride	3-7
(KOH) Potassium hydroxide	3-7
(I-V) current-voltage	4-1
(SEM) Scanning Electron Microscope	4-2
(PC) personal computer	4-3
(UV) ultra violet	5-6
(FTO) Folded Transverse Optical	5-7
(FLO) Folded Longitudnal Optical	5-7
(SNR) signal to noise ratio	5-20

DETECTION OF RESIDUAL STRESS IN SiC MEMS USING μ -RAMAN SPECTROSCOPY

I. Introduction

Silicon Carbide (SiC) micro-electro-mechanical-systems (MEMS) structures are being studied by NASA Glenn Research Center researchers in conjunction with the Munitions Directorate, Air Force Research Laboratory (AFRL/MN) as engine pressure sensors/accelerometers for munition fuzes. SiC is recognized for its superior mechanical, electrical and chemical properties, making it a good choice for applications in the harsh environments of these applications [5]. SiC is characterized as a semiconductor with a "wide band gap, high acoustic velocity, high thermal conductivity, high electrical breakdown strength, and low chemical reactivity [6]." The characteristics of SiC that make it useful in harsh environment applications also make it difficult to fabricate MEMS [7]. However, recent advances in fabrication technologies have enabled the micromachining of SiC to a comparable level of sophistication as Si devices.

1.1 Motivation

The Air Force has an increasing demand for semiconductor devices that can withstand a wide range of harsh environments. For example, sensors are being developed for the monitoring of parameters within gas turbine, rocket and internal combustion engines. Also, hardened electronics and transducers are required for the space environment where radiation effects and vast temperature differences exist. Current semiconductor devices primarily require the use of Si-based electronics which are limited in their temperature range of operation to less than 250 °C [7]. Due to many of the excellent material properties of SiC, SiC electronic and MEMS devices have the potential to replace Si in harsh environment applications.

1.1.1 Applications: SiC Electronic devices. SiC has a high breakdown electric field which makes it ideal for high-power devices. Several different prototype electronic devices have been fabricated from SiC and there are indications that they will see improved success. There are four different classifications, which are described in Andrew Attwell's PhD. dissertation, [8]. The first one he describes is a junction field-effect transistor (JFET) used in radiation environments such as space. The second is the metal-semiconductor field-effect transistor (MESFET) designed for high frequency applications. The third group is high-power devices which includes p-n junctions, Schottky barrier diodes and power metal-oxide-semiconductor field-effect transistors (MOSFET). The last group is SiC complementary MOSFET (CMOS) integrated circuits (IC's) for harsh environment applications. Other electronic applications are described in detail by Phil Neudeck in his SiC technology reviews [9, 10].

The major limitations to all of these devices has been attributed to a large defect density in the SiC wafers and the difficulty in obtaining consistently good ohmic contacts to p-type SiC [8]. Recently, however, Nakamura *et al.* reported "a new method to reduce the number of dislocations in SiC single-crystals by two to three orders of magnitude, rendering them virtually dislocation-free [11]." The need for defect characterization is still important to advance the use of SiC for electronics.

1.1.2 Applications: SiC MEMS. There are also several prototype SiC MEMS devices which illustrate the advantages of using SiC materials. A range of sensors have been fabricated and tested for the measurement of temperature, gas species, pressure, and various other parameters in harsh environments [7]. One such device is the pressure sensor in Figure 1.1. The center square is a flexible diaphragm, which flexes with increased pressure, changing the conductivity of the material producing a measurable response.

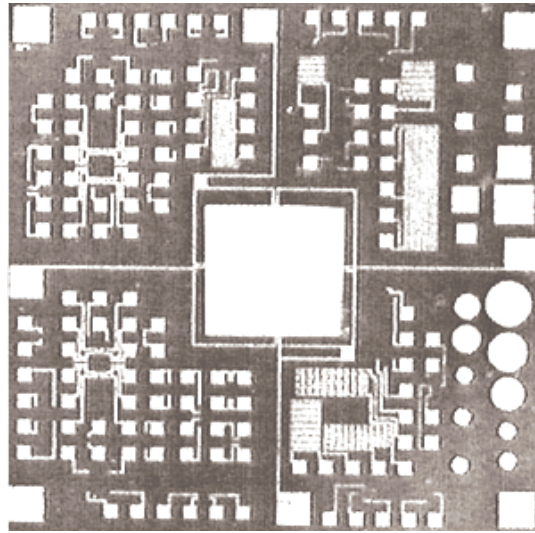


Figure 1.1 Pressure Sensor reported to exhibit stable operation at 500°C [3] .

A third application of SiC MEMS has been in the area of radio frequency (RF) MEMS devices such as microfabricated switches, micromechanical resonators and filters [6]. There have been efforts to improve Si-based resonators resulting in devices with vibrational frequencies greater than 100 MHz. Even with the advances in Si technologies, there still is increasing desire to develop material other than Si for MEMS devices that can resonate at higher frequencies and still have a high quality factor (Q). SiC is one of the most promising materials for these RF application due to its high acoustic velocity and recent advances in fabrication technologies [6].

Another SiC MEMS application that has had considerable success is the SiC MEMS atomizer for gas turbine engines depicted in Figure 1.2. The SiC atomizer has been tested against a similar nickel atomizer for performance and erosion. While both atomizers performed well in excess of 2.5 MPa, the SiC device exhibited higher erosion resistance at those high pressures [12].

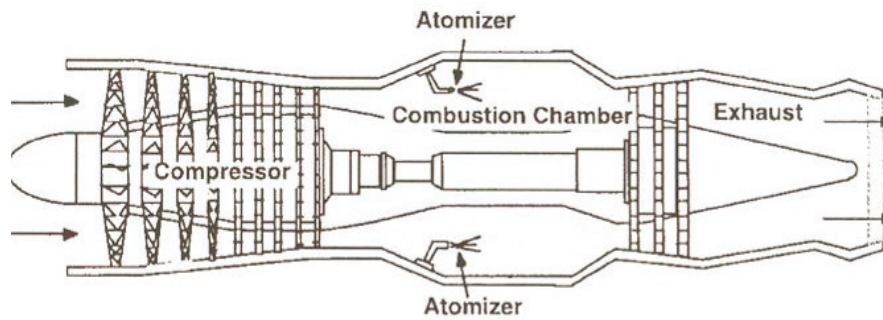


Figure 1.2 Cross section of a typical gas turbine engine showing atomizer insertion points [12].

An application of high interest and value is the development of SiC piezoresistive MEMS accelerometers. The piezoresistive MEMS accelerometer is of great value as a sensor for fuzes for penetrating weapons that see forces greater than 10^4 g's. The fuze was developed under the AFRL/MN in conjunction with NASA Glenn Research Center, Cornell University, and Applied Research Associates (ARA) [13]. The first generation device was tested and remained operational with over 40,000-g's applied in a strong EM field at temperatures reaching 600°C , all well beyond the capability of Si based fuzes [14].

1.2 Current technology limitations

Phil Neudeck [10], described the current technological limitations of SiC devices saying:

Improvements in epilayer quality are needed as SiC electronics upscale toward production integrated circuits, as there are presently many observable defects present in state-of-the-art SiC homoepilayers. Non-ideal surface morphological features, such as "growth pits", 3C-SiC triangular inclusions ("triangle defects"), are generally more prevalent in 4H-SiC epilayers than 6H-SiC epilayers. Most of these features appear to be manifestations of non-optimal "step flow" during epilayer growth arising from substrate defects, non-ideal substrate surface finish, contamination, and/or unoptimized epitaxial growth conditions. While by no means trivial, it is anticipated that SiC epilayer surface morphology will greatly improve as refined substrate preparation and epilayer growth processes are developed.

In a 2002 IEEE paper, "Silicon Carbide for MEMS and NEMS-An Overview" the authors C. Zorman and M. Mehrgany [5] from Case Western University, outline the state-of-the-art fabrication techniques for SiC MEMS. In that paper, they stated some of the limitations that fabricators are experiencing, saying:

Despite the initial success in fabricating devices using the multilayer micromolding process, several technical issues must be addressed before the process is at the level of poly-Si surface micromachining. In terms of residual stress, the measured values for the atmospheric pressure chemical vapor deposition (APCVD) poly-SiC films was not unreasonably high (140MPa). However, the films suffered from excessive stress gradients, which leads to significant bending of beams, especially for long, narrow structures. Such bending had harmful effects on comb-drive actuators and other devices that require coplanar structures [5].

1.3 Problem Statement and Research Objectives

The objective of this research is to determine a non-destructive evaluation (NDE) method of identifying residual stress, stress gradients and defects in SiC MEMS. A correlation between variations the Raman spectrum of SiC and stress in the crystal structure is to be shown. An NDE technique that employs the spatial mapping of the Raman spectrum across SiC MEMS will allow for visual identification of areas containing residual stress and defects.

1.4 Thesis Organization

This thesis is broken into five chapters. Chapter II contains background information including: a description of the basics of Raman spectroscopy, the causes of residual stress, background on SiC MEMS, general knowledge about SiC crystals, and a thorough literature review. In Chapter III, there is a description of the SiC samples that were investigated. Chapter IV contains a brief description the experimental equipment and procedures. Chapter V presents the results of the experiments and discusses the results. In Chapter VI, the conclusions from the results are drawn and future work is laid out.

II. Background Information

Chapter I gave an introduction to the problem being addressed by this work. This chapter explains the background information on: (1) μ -Raman spectroscopy, (2) residual stress, (3) the previous characterization of residual stress in Si using μ -Raman spectroscopy, (4) basic knowledge of the material characteristics of SiC, and (5) a literature review on important topics related to the detection of residual stress in SiC using μ -Raman spectroscopy.

2.1 μ -Raman Spectroscopy

μ -Raman was chosen to investigate residual stress in SiC MEMS because it is an established technique for investigating crystal defects in SiC. According to E. Martin *et al.*, μ -Raman has been shown capable of : "(i) micrometer size lateral resolution, (ii) polytype identification, (iii) it is sensitive to crystal disorder, (iv) it is sensitive to stress, and (v) it is sensitive to doping" [15].

Raman spectroscopy is a material characterization technique utilizing the third-order nonlinear optical effect of Raman scattering depicted in Figure 2.1. Raman scattering is the diffraction of light due to vibrations in the lattice of a crystal. The momentum of these vibrations is described by an optical phonon. When a photon of light interacts with the vibration phonon, the light is scattered at a shifted frequency. The scattering of light can be used to characterize crystalline and poly-crystalline materials. In addition, residual stress in the lattice will also cause a shift in the phonon energies of the lattice proportional to the strain in the lattice. The shift in frequency of the scattered light is used to measure the stress in MEMS devices [13].

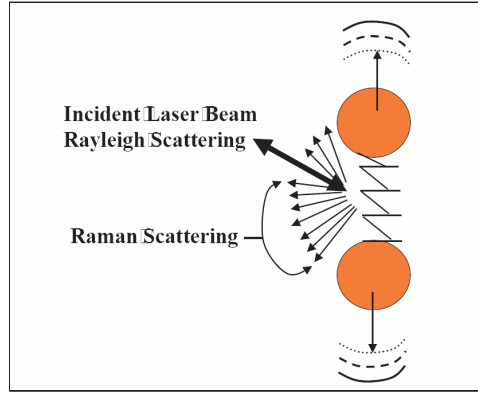


Figure 2.1 Schematic depicting the Raman and Rayleigh scattering of an excitaion source due to phonon or vibrational energy present between two atoms [16].

The classical approach to describing the Raman effect was developed by Ferraro *et al.* in [17].

The electric field strength (E) of the electromagnetic wave (laser beam) fluctuates with time (t) as shown by Eq. (2.1):

$$E = E_o \cos 2\pi v_o t \quad (2.1)$$

where E_o is the vibrational amplitude and v_o is the frequency of the laser. If a diatomic molecule is irradiated by this light, an electric dipole moment, P , is induced:

$$P = \alpha E = \alpha E_o \cos 2\pi v_o t \quad (2.2)$$

Here, α is a proportionality constant and is called *polarizability*. If the molecule is vibrating with a frequency, v_m , the nuclear displacement, q , is written

$$q = q_o \cos 2\pi v_m t, \quad (2.3)$$

where q_o is the vibrational amplitude. For a small amplitude of vibration, α is a linear function of q . Thus, we can write

$$\alpha = \alpha_o + \left(\frac{\partial \alpha}{\partial q} \right) q_o + \dots \quad (2.4)$$

Here, α_o is the polarizability at the equilibrium position, and $(\partial \alpha / \partial q)_o$ is the rate of change of α with respect to the change in q , evaluated at the equilibrium position.

Combining (2.2) with (2.3) and (2.4), we obtain

$$\begin{aligned}
P &= \alpha E_o \cos 2\pi v_o t \\
&= \alpha_o E_o \cos 2\pi v_o t + \left(\frac{\partial \alpha}{\partial q} \right)_o q E_o \cos 2\pi v_o t \\
&= \alpha_o E_o \cos 2\pi v_o t + \left(\frac{\partial \alpha}{\partial q} \right)_o q E_o \cos 2\pi v_o t \cos 2\pi v_m t \\
&= \alpha E_o \cos 2\pi v_o t \\
&\quad + \frac{1}{2} \left(\frac{\partial \alpha}{\partial q} \right)_o q E_o [\cos 2\pi(v_o + v_m)t + \cos 2\pi(v_o - v_m) \cdot t] \quad (2.5)
\end{aligned}$$

According to classical theory, the first term represents an oscillating dipole that radiates light of frequency, v_o , (Rayleigh scattering), while the second term corresponds to the Raman scattering of frequency, $v_o + v_m$ (anti-Stokes) and $v_o - v_m$ (Stokes). If $(\partial \alpha / \partial q)_o$ is zero, the vibration is not Raman-active. Namely, to be Raman-active, the rate of change of polarizability (α) with the vibration must not be zero.

In Figure 2.2, Raman shifts are depicted in terms of allowed energy states. The infrared (IR) transitions are shown from the electronic ground state to the first vibrational state, v_1 . The Rayleigh frequency is equal to the excitation frequency, v_o . For normal Raman, the Rayleigh transitions occur between a virtual state (indicated by the dashed line) and the electronic ground state ($v = 0$), with an energy level less than the first electronic excited state ($v' = 0$). For the Stokes shift, v_s , there is a transition from the same virtual state as the Rayleigh line, however, the return transition ends at the first vibrational state ($v = 1$). For the anti-Stokes frequency, v_s , an excitation of carriers in the first vibration state ($v = 1$) occurs and the return transition is to the electronic ground state generating a slightly higher frequency than the excitation source. In addition, the population density of the first vibrational state ($v = 1$) is much less than the ground state; therefore, the anti-Stokes transitions are much less likely to occur [17].

Resonant Raman transitions occur when the excitation energy exceeds the band gap energy causing transitions above the electronic excited state. In solid materials, such as SiC, the vibrational levels above the excited state are broadened into a continuum of states. Excitation into the continuum produces resonant effects, which can enhance Raman lines

by a factor of 10^3 or 10^4 relative to normal Raman (see reference [17]). Fluorescence is another effect that can occur if a carrier is excited to an electronic state. In the case of fluorescence, an excited carrier decays to the lowest excited state ($v' = 0$) and then transitions to either the ground state or a vibrational level.

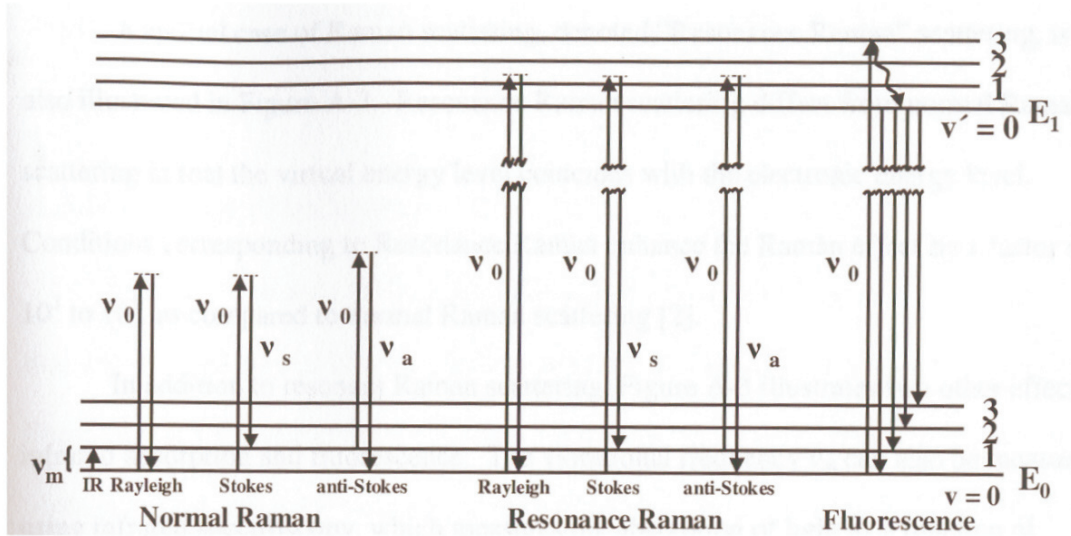


Figure 2.2 Energy levels for normal Raman, resonance Raman, and fluorescence spectra [17].

The 6H-SiC material used to fabricate the bulk single-crystal MEMS devices has a unique Raman shift that has been measured in previous experiments such as the results seen in Table 2.1. The transverse optical (TO) phonons generate three Raman shifts in 6H-SiC, TO1 at 766 cm^{-1} and TO2 at 788 cm^{-1} and 796 cm^{-1} . The longitudinal optical (LO) phonons generate a Raman shift in 6H-SiC at 966 cm^{-1} [18].

2.2 Residual Stress

Residual stress is the stress that occurs in a material due to the manufacturing process. Residual stress in 3C-SiC structures deposited on Si comes from two main sources: differing lattice constants and different thermal expansion coefficients. Other

Table 2.1 Raman Shift peak locations for common polytypes of SiC [2]

	Frequency (cm ⁻¹)			
	TA	TO	LA	LO
3C(β)		796		972
2H	264	799 764		688
4H	204	796 767	610	964
6H	145	797 767	504 514	965
15R	167 173	797 785 769	569 577	965

sources include impurities introduced during the deposition process, variations in process, and interstitial atoms or vacancies in the crystal lattice further discussed in Section 2.6 [5].

2.3 Detection of Residual Stress in poly-Si

Research into residual stress in SiC MEMS has many advantages including providing information that could help in the designing of reliable SiC MEMS fuze sensor. Studies of the properties of both thin film 3C-SiC and 6H-SiC have been utilized by MEMS developers and thus are the focus of this study. The measurement of residual stress in MEMS structures was initially performed at the Air Force Institute of Technology (AFIT) by Capt L. Starman in his dissertation, "Characterization of residual Stress in Microelectromechanical Systems (MEMS) devices using Raman Spectroscopy" [16]. The work done by Capt Starman, which includes methods for characterization and mitigation of residual stress in poly-Si MEMS, was considered in the characterization of the residual stress in both poly-SiC and bulk SiC MEMS.

Some of the results of Starman's experiment [16] on stressed poly-Si MEMS can be seen in Figure 2.3 which shows the shift in Raman peak signal of a poly-Si sample as stress is applied. The error bars are representative of shifts in the peak Raman signal for each applied stress over a series of three measurements. The variation was explained by

the polycrystalline nature of the material. While the global stress was uniaxial, the stress on the 30-nm grains simulated hydrostatic pressure. The Raman signal was measured over several grains, thus slightly different Raman shifts were sampled. Note the linear relation between applied stress and Raman shift.

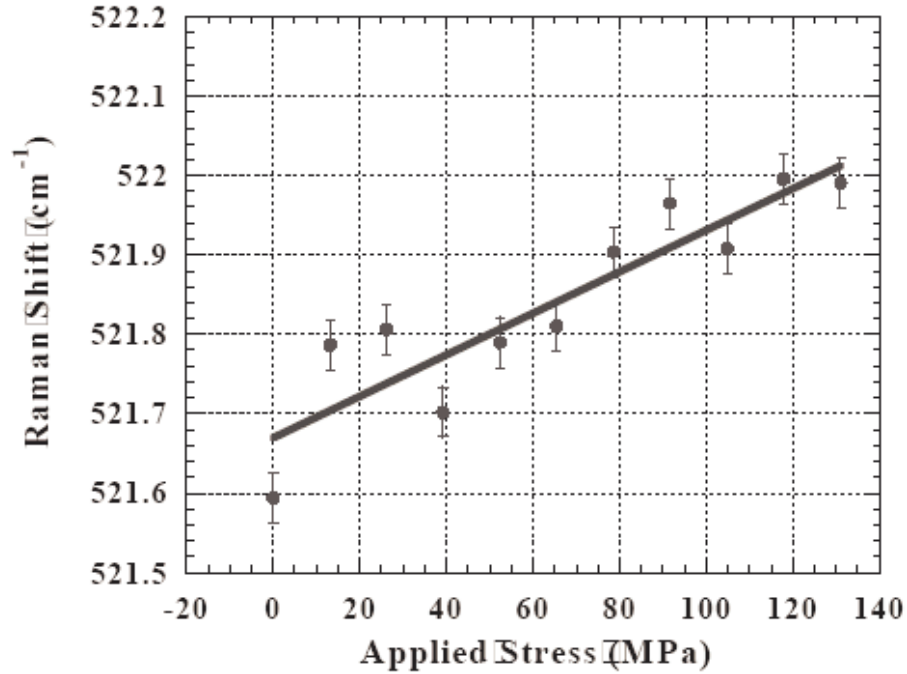


Figure 2.3 "Frequency shift of the hydrostatic component for an applied uniaxial stress applied along a 1.5 μm -thick Poly2 cantilever with dimensions of 200 μm -wide by approximately 4000 μm -long" [16].

Once Starman found the phonon deformation potential corresponding to the poly-Si, he was able to measure the residual stress in poly-Si MEMS structures such as beams and cantilevers before and after they were released from the substrate. Figure 2.4 below presents three different thicknesses of beams. Poly1 is 2.0- μm , Poly2 is 1.5- μm and Poly1-Poly2 is 3.5- μm thick. The amount of stress clearly decreases after release. Therefore, the structures were determined to be appropriate for testing methods of mitigating the stress, such as ion implantation of the MEMS structures. For the thin-film SiC MEMS, the same method should apply once the phonon deformation potential can be quantified.

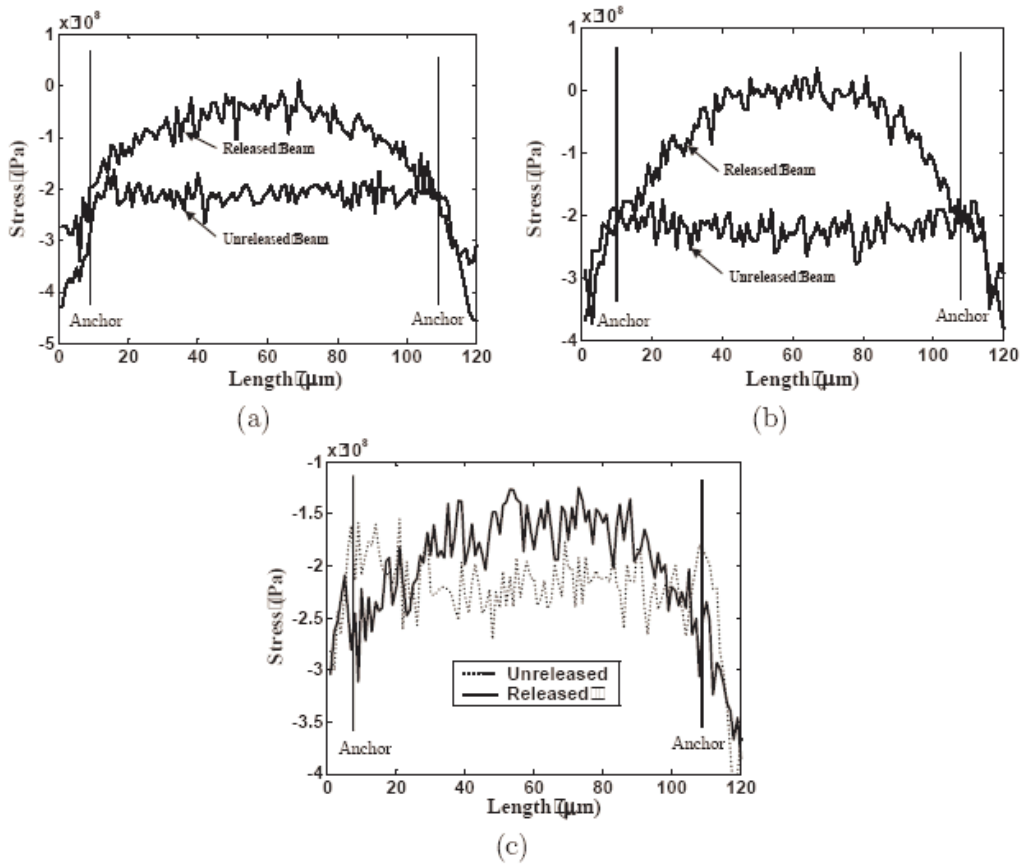


Figure 2.4 "Background residual stress profiles for a 100- μ m-long by 10- μ m-wide un-released and released fixed-fixed beam. (a) Poly1 beam, (b) Poly2 beam and (c) Poly1-Poly2 stacked beam" [16].

The following analytical model was developed in order to compare the results of the Raman stress profiles measured on the test beams. Figure 2.5 shows the diagram used to determine the residual stress profile for a fixed-fixed beam with a uniform load, g , due to an applied force. $R1$ and $R2$ are the resultant forces, and $M1$ and $M2$ are the moments about the beam [16].

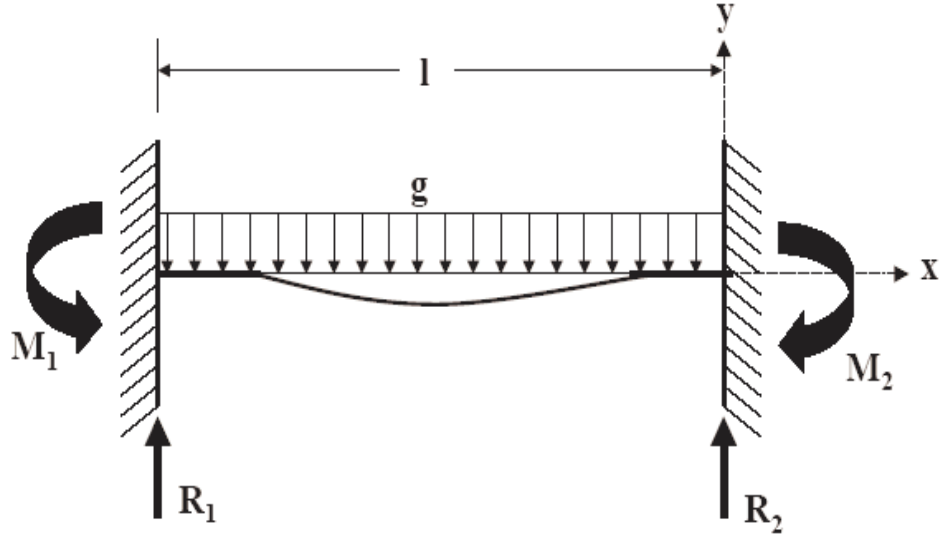


Figure 2.5 "Analytical stress model for a MEMS fixed-fixed beam" [16].

After the fixed-fixed beam is released, if a uniform distributed load is applied, then residual stress can be calculated by the following equation [16],

$$\sigma = \frac{M(x)y}{I} (Pa) \quad (2.6)$$

where $M(x)$ is the moment about the beam and is given by [16]

$$M(x) = \frac{g}{12}(6lx - 6x^2 - l^2) (N/m) \quad (2.7)$$

where g (N/m) is the distributed load, l (μm) is the beam length, and x (μm) is the selected position along the length of the beam [16]. Figure 2.6 show the stress profile that was plotted from the analytical model of the beam with a uniform load which matches the results of the stress profile of the actual beams.

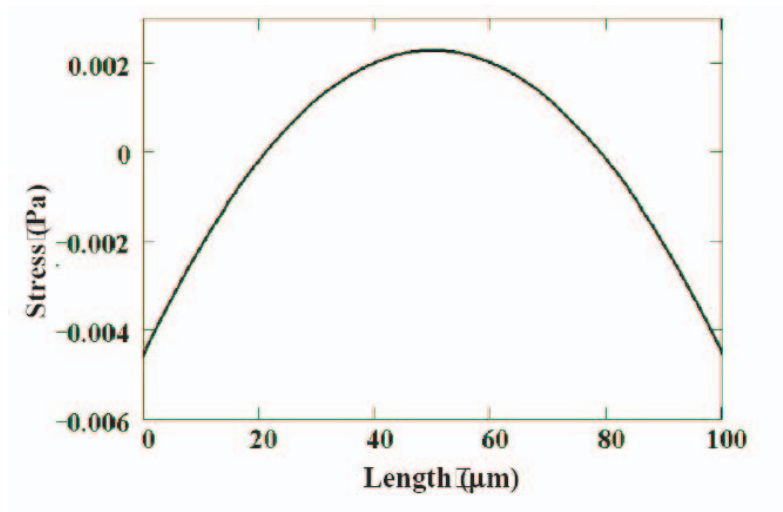


Figure 2.6 "Analytical stress profile of a fixed-fixed beam with a uniform load [16]."

2.4 Background Information on SiC

In order to understand SiC as a material for microdevices, it is necessary to study the properties of SiC. SiC possesses one-dimensional polymorphism which is known as polytypism. The different polytypes of SiC have the same planar arrangement of Si and C atoms. The only difference in the polytypes is in the stacking arrangement of the identical planes along either the $\langle 111 \rangle$ or $\langle 0001 \rangle$ crystal axes. These different arrangements result in more than 250 SiC polytypes. Even though there are 250+ polytypes, there are only three crystalline structures: cubic, hexagonal, and rhombohedral. In the past, the cubic phase of SiC was called beta-SiC, and the hexagonal and rhombohedral structures were called alpha-SiC. The modern, more descriptive nomenclature has been adopted that identifies both the crystalline symmetry and stacking periodicity (C = cubic, H = hexagonal, and R = rhombdahedral). Using this system, beta-SiC is called 3C-SiC. 3C-SiC is the only cubic polytype known to exist. The most common alpha-SiC polytypes have hexagonal symmetries and are called 6H-SiC, 4H-SiC, and 2H-SiC [5] (see Figure 2.7).

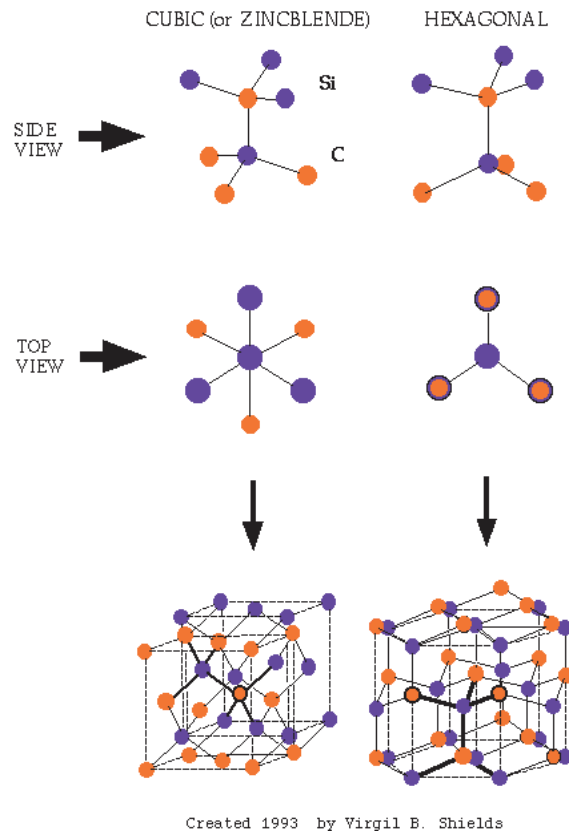


Figure 2.7 Lattice structure of cubic and hexagonal SiC [19].

The various polytypes of SiC are comprised of multiple arrangements of stacking orders of Si-C double layers. The Si-C double layers form planar sheets of Si atoms and planar sheets of C atoms. A plane of either of the double layers of Si and C atoms is called the basal plane, the normal direction to the basal plane is named the c-axis, which is designated the $[0001]$ direction. Figure 2.8 shows the stacking order of the 6H-SiC polytype. The unit cell is defined by six double layers of Si-C along the c-axis or $[0001]$ direction. The $[1\bar{1}00]$ direction seen in Figure 2.8 is called the a-axis direction. The Si atoms in Figure 2.8 that are labeled “h” or “k” indicate the Si-C double layers. SiC is a considered a polar semiconductor because one surface that is normal to the c-axis is all Si atoms while the next layer normal to the c-axis surface is all C atoms. As shown in Figure 2.8, these planes of Si or C are referred to as the “Si face” and “C face” surfaces [10].

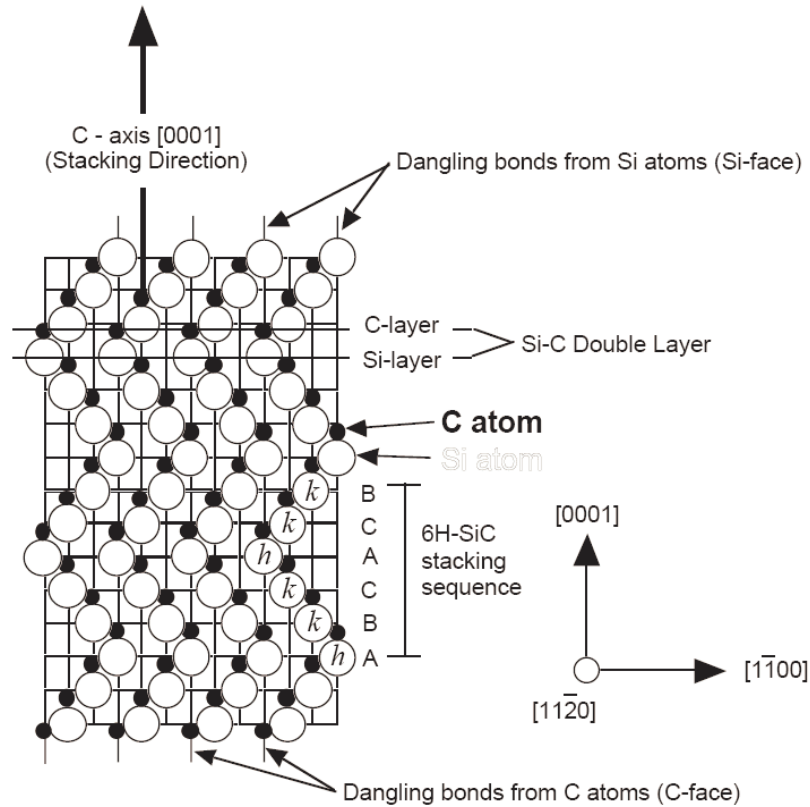


Figure 2.8 Representation of stacking order for 6H-SiC [10].

Even though the SiC polytypes are comprised of the same atomic composition, the electrical properties are quite different and should be taken into account when designing devices with these materials. From Table 2.2, the bandgap for 3C-SiC is 2.2 eV while for 6H-SiC it is 2.9 eV. The 3C-SiC has a smaller bandgap, but it has a higher electron mobility ($1000 \text{ cm}^2/\text{V}\cdot\text{s}$) and a saturation drift velocity (107 cm/s) as a result of its cubic crystalline symmetry [5].

2.5 Fabrication of SiC MEMS

The same techniques used for poly-Si MEMS, such as bulk micromachining, surface micromachining and micromolding, can be applied in the design of SiC MEMS [5].

Table 2.2 Material Properties of 3C and 6H SiC at 300K [3]

Property	3C-SiC	6H-SiC	Si
Melting Point ($^{\circ}C$)	1825(sublimes)	1825(sublimes)	1414
Max. Operating Temp. ($^{\circ}C$)	873	1240	300
Thermal Conductivity ($^{\circ}C$)	4.9	4.9	1.5
Thermal Expansion Coeff. ($\ast 10^{-6} \text{ }^{\circ}C^{-1}$)	3.8	4.2	2.6
Young's Modulus (GPa)	448	448	190
Physical Stability	Excellent	Excellent	Good
Energy Gap (eV)	2.2	2.9	1.12
Electron Mobility ($\text{cm}^2/V - s$)	1000	500	1350
Hole Mobility ($\text{cm}^2/V - s$)	40	50	600
Sat. Electron Drift Vel ($\ast 10^7 \text{ cm/s}$)	2.5	2	1
Breakdown Voltage ($\ast 10^7 \text{ cm/s}$)	3	4-6	.3
Dielectric Constant	9.7	13.2	11.9
Lattice Constant (\AA)	4.36	5.65	5.43

One such process that has been developed is known as the Multi-User Silicon Carbide (MUSIC) process, which combines micromolding and micromachining techniques. The MUSiC process is very similar to the Multi-User MEMS Processes (MUMPs) process often used for micromachining poly-Si [5].

Bulk micromachining of SiC structures is normally done on 3C-SiC films on Si substrates using Si bulk micromachining techniques. The technique is described as relatively easy due to the chemical stability of SiC against Si anisotropic wet etchants like KOH. However, for bulk micromachining of bulk SiC, no current anisotropic wet-etch techniques have been identified [5].

With the limitations of bulk micromachining, SiC researchers have turned to micro-molding techniques of poly-SiC to produce the same structures produced in Si MEMS. Si molds are formed using deep reactive ion etching (DRIE), then coated with a thick poly-SiC film deposited by chemical vapor deposition (CVD). The surface is then mechanically polished to remove the layer of poly-SiC exposing the Si mold. To release the poly-SiC structure, the Si mold is chemically etched [5].

Surface micromachining of SiC using chemical etching and RIE has proven difficult. Developers have turned again to combinations of micromolding and mechanical polishing to create microstructures such as lateral resonator structures and double layer micromotors (see Figure 2.9 and Figure 2.10) [5].

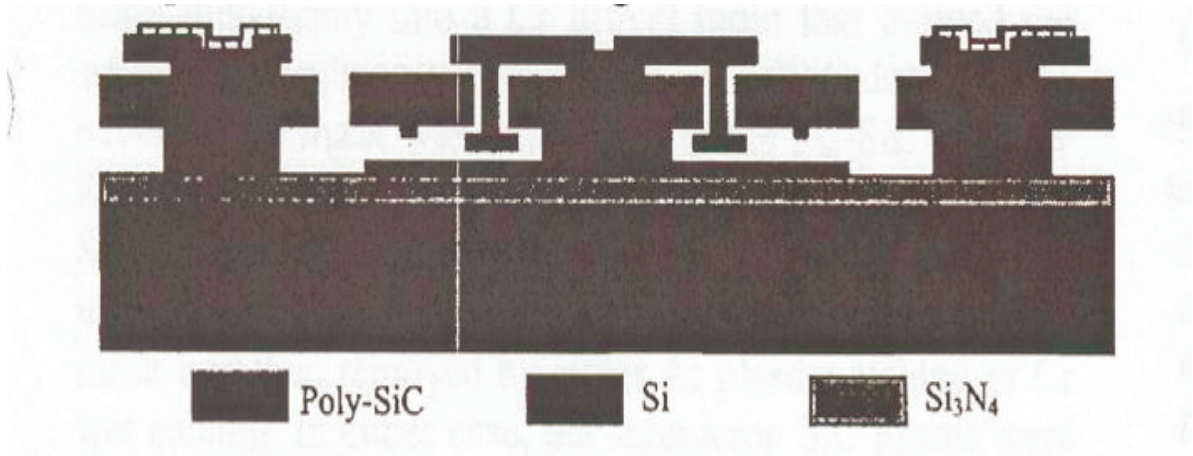


Figure 2.9 "Cross-section schematic of a SiC micromotor fabricated using the MUSiC process" [5].

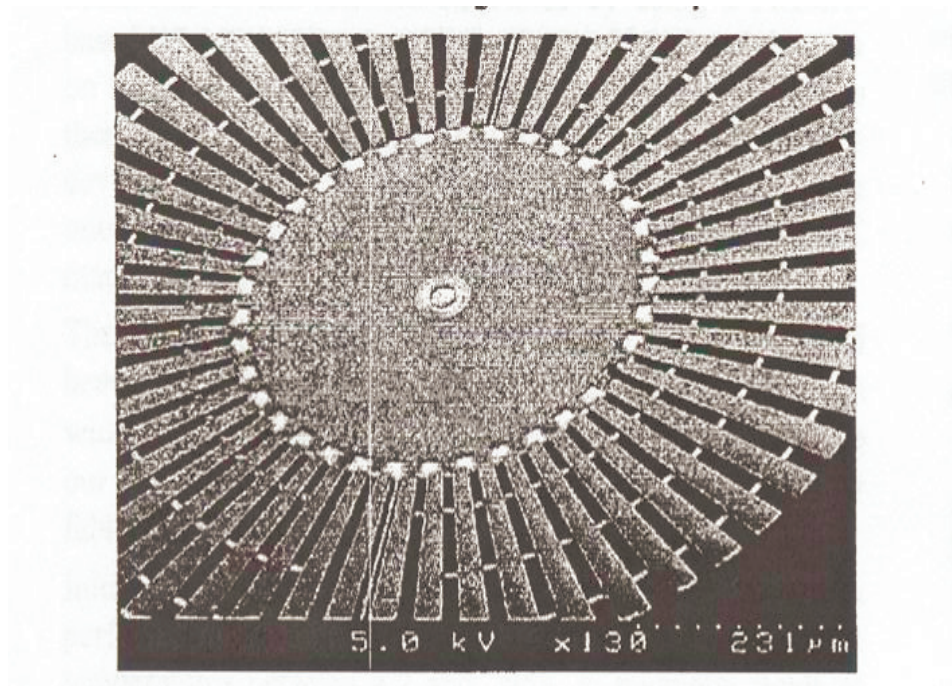


Figure 2.10 "SEM micrograph of a SiC salient-pole micromotor fabricated using the MUSiC process" [5].

The concept of micromolding has been developed further in the MUSiC process. The process contains four poly-SiC layers for surface micromachining, which utilizes the same design as for the MUMPs process, although the devices cannot be directly designed using the same steps. The MUSiC process instead uses the previously described micro-molding techniques [5].

2.6 *Crystal Defects of SiC*

Defects in SiC crystals are a major limiter in the realization of SiC electronics and MEMS. Defects can be classified into four types: point, line, area and volume. It is important to be able to characterize and understand the influence of defects in crystals such as SiC because they effect its optical, electrical and mechanical properties [20]. They are also of interest because they introduce stress into the crystal lattice.

2.6.1 Point Defects. There are four types of point defects, which are represented in Figure 2.11. One defect occurs when an impurity atom is located at a lattice site (Figure 2.11 (a)) and another defect exists when an impurity is between lattice sites (Figure 2.11 (b)). If an atom is missing from a lattice site, it is called vacancy defect (Figure 2.11 (c)), and if an atom from the crystal moves out from its lattice site, it is considered a Frenkel-type defect (Figure 2.11 (d)) [20]. For details on point defects in SiC and their effects, see "Electron paramagnetic resonance of electronic grade SiC substrates" by M. Zvanut [21].

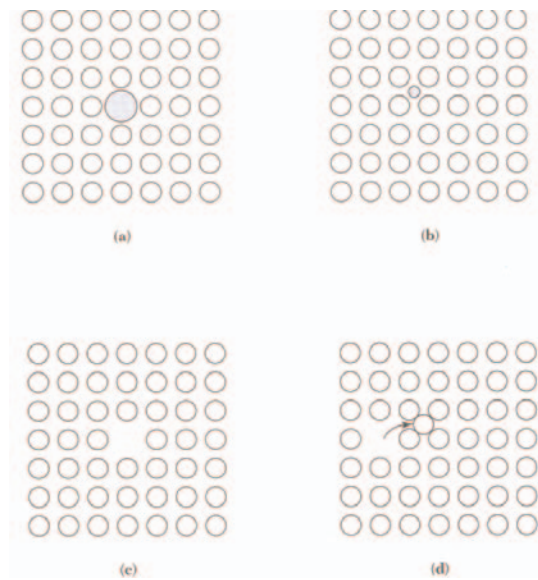


Figure 2.11 Point defects: (a) substitutional impurity; (b) interstitial impurity; (c) lattice vacancy; and (d) Frenkel-type defect [22] .

2.6.2 Line Defects. A line defect is typically called a dislocation. The two types of line defects are screw and edge. An edge dislocation of a cubic lattice is shown in Figure 2.12 (a) where an extra plane of atoms (AB) is present in a portion of the lattice. A screw dislocation is represented in Figure 2.12 (b) showing that the crystal plane is shifted one part of the crystal one space over [20].

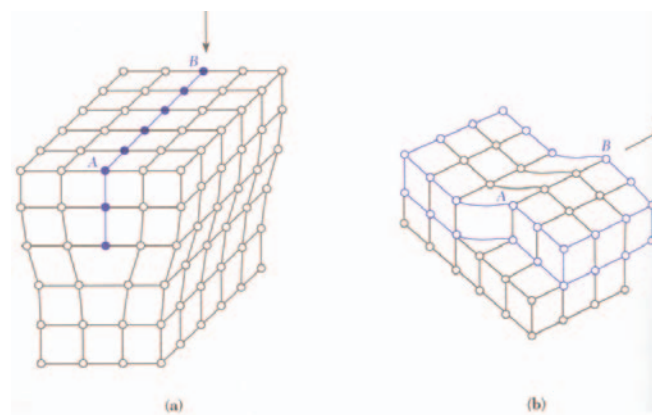


Figure 2.12 (a) Edge and (b) screw dislocations in cubic crystals [23].

2.6.3 Area Defects. Area defects are large areas of the crystal which are discontinuous. Grain boundaries such as the ones in polycrystalline material can be considered defects. Another defect which will be considered in the results of this thesis are stacking faults in which the stacking periodicity of the atom planes changed. If a plane is missing, it is called an intrinsic stacking fault. If an extra plane is present, it is called an extrinsic stacking fault [20].

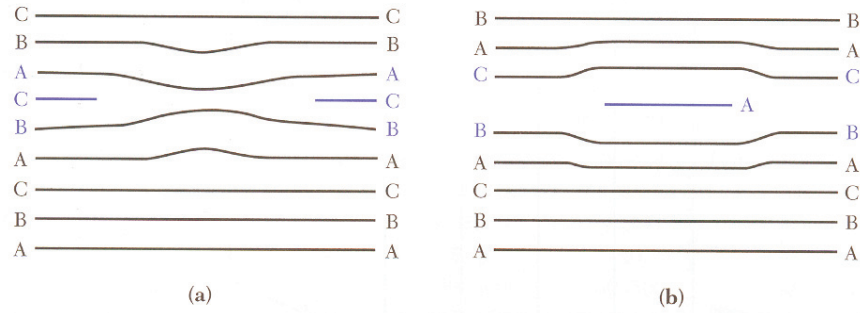


Figure 2.13 Stacking faults in semiconductors: (a) intrinsic stacking fault; and (b) extrinsic stacking fault [22].

2.6.4 Volume Defects. Volume defects are formed from precipitants from impurities. When the crystal is formed, there exists a maximum concentration of impurities that the crystal can allow. The impurities that exceed this level of concentration precipitate and form the volume defects [20].

2.6.5 Micropipes. Micropipes are screw dislocations with a hollow core which form hexagonal tube-like cavities that have diameters in the neighborhood of a few μm , and form parallel to the c-axis of the hexagonal structure [24]. Most SiC experts agree that micropipes are the most harmful defect in SiC. An image of an etched micropipe is shown in Figure 2.14. Under the current growth techniques used to produce 4H- and 6H-SiC wafers, there exist high densities of screw dislocations defects which, like micropipes, cause a considerable amount of localized strain in the SiC. The strain will effect the operation of both SiC MEMS and electronics [10].

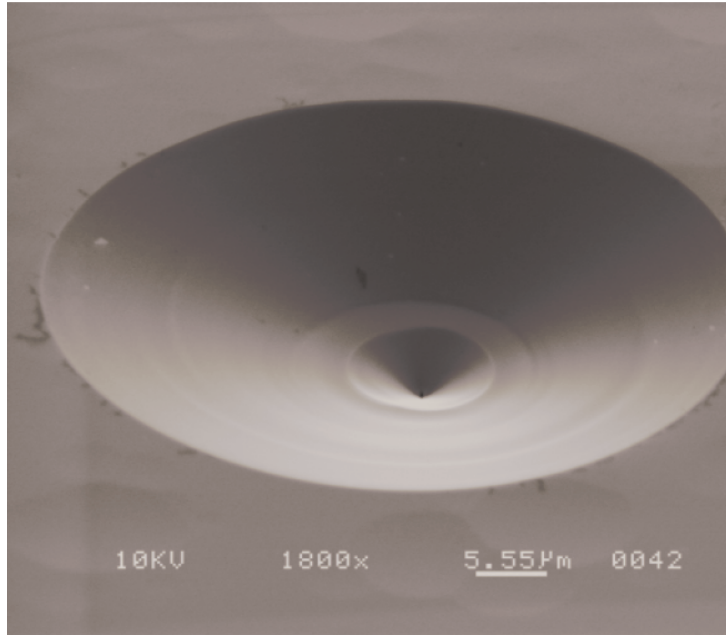


Figure 2.14 Etched micropipe in a SiC diaphragm [8].

2.7 Literature Review

There has been an on going effort in the materials research community to correlate the Raman spectrum of SiC to defects and stress in the SiC. Initial studies into the Raman spectrum of 6H-SiC using laser excitation sources date back to 1968 with Feldman *et al.* [25]. Since that time, many advances have been made in 6H-SiC crystal quality and Raman spectrum techniques. The Raman spectrum for 6H-SiC is well characterized and the peaks are shown in Figure 2.15 for a comparison to the Raman spectrum collected in this research. The folded transverse optical (FTO) lines are $x = 1$ at 766-cm^{-1} , $x = 1/3$ at 788-cm^{-1} , and $x = 0$ at 796-cm^{-1} . The folded longitudinal optical (FLO) line is for $x = 0$ at 966-cm^{-1} [18].

Where according to Feldman *et al.*:

For long-wavelength phonons we need to consider only the axial direction of the large zone. (SiC polytype structures are characterized by a one-dimensional stacking sequence of planes. Consequently, the large zone is extended in only one direction, the axial direction, and all long wavelength

modes are found on the large-zone axis.) The standard large zone for 6H-SiC extends to $6\pi/c$, where c is the axial dimension of the unit cell. Since $2\pi/c$ is a reciprocal lattice vector, the pseudomomentum vectors $q = 0, 2\pi/c, 4\pi/c$, and $6\pi/c$ are all equivalent to $q = 0$ in the Brillouin zone. Thus, if we define a reduced momentum $x = q/q_{\max}$, the values of x accessible to Raman scatter measurements are $x = 0, 0.33$, and 1 [25].

Raman spectroscopy can only detect the fundamental modes of vibration that are at the center of the Brillouin zone where the momentum vector is $k = 0$. For that reason, only the fundamental modes of vibration that occur at $x = 0, 0.33$ and 1 can be measured by using Raman techniques [17]. For convenience, the intense lines at 766-cm^{-1} , 788-cm^{-1} and 966-cm^{-1} will be called TO1, TO2 and LO, respectively.

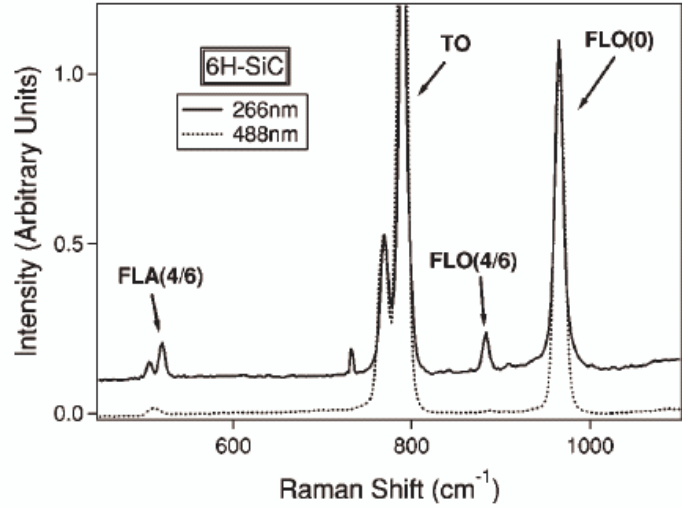


Figure 2.15 Raman Spectrum of 6H-SiC using 266-nm and 488-nm excitation sources [26].

According to Ferrero *et al.* [27], Figure 2.16 represents the Raman spectrum for both 3C-SiC and 4H-SiC. The Raman peaks for the 4H-SiC were observed at 776 cm^{-1} for the FTO mode and at 964 cm^{-1} for the FLO mode. The Raman peaks for the 3C-SiC were observed at 796 cm^{-1} for the FTO mode and 972 cm^{-1} for the FLO mode.

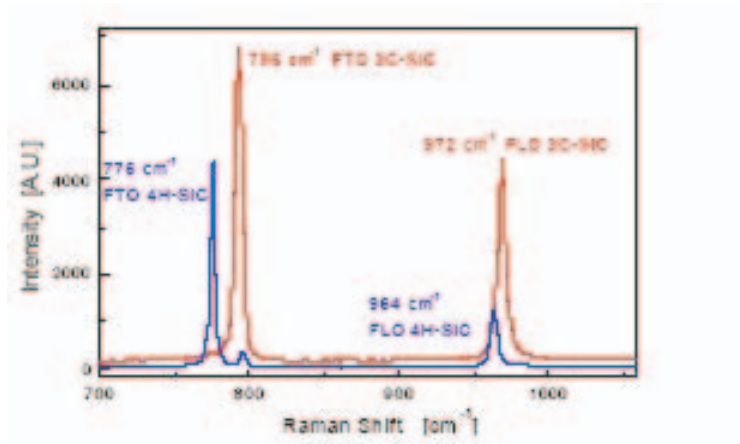


Figure 2.16 Raman spectra, 3C-SiC [27].

Defect studies have been conducted extensively in 6H-SiC using Raman spectroscopy in order to help improve crystal quality [15,27]. However, little has been done in the way of residual stress measurements of 6H-SiC MEMS. The work focused on the characterization of defects has provided some basic information needed for the detection of residual stress in SiC MEMS such as a measurement of the phonon deformation potential of 6H-SiC at ultra high pressures by Liu *et al.* [28]. They demonstrated that for their 6H-SiC crystal, the TO2 mode frequencies held the relationship that

$$\omega_{TO2} = 789.2 + 3.11P - 0.009P^2 \quad (2.8)$$

where, P is a positive compressive pressure measured in GPa. This information is a useful reference to compare the results of the phonon deformation potential measured in this work. (However, the 6H-SiC crystals were manufactured by different crystal growers resulting in slight differences.)

In contrast, more work has been done in the way of detecting residual stress in 3C-SiC thin films by Lee *et al.*. They were able to map the phonon deformation potential for poly-crystalline 3C-SiC using a four-point bending fixture. The result is in the inset in Figure 2.17. Spectrum (A) in Figure 2.17 shows the spectrum of the bulk poly-crystalline

3C-SiC that was used to find the phonon deformation potential. Spectrum (B) shows the spectrum of their thin film polycrystalline SiC samples on a (111) Si substrate [1].

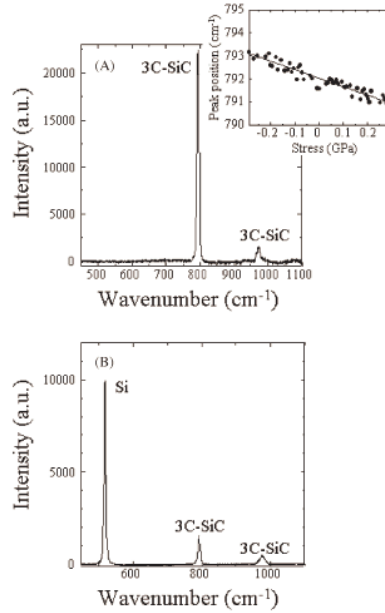


Figure 2.17 The transversal optical (TO) mode of bulk poly-3C-SiC by Lee *et al.* [1].

Lee *et al.* were able to take the knowledge of the phonon deformation potential in Figure 2.17 and map residual stress in thin-film structures as shown in Figure 2.18.

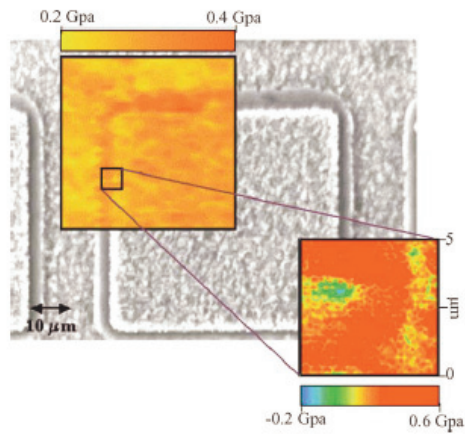


Figure 2.18 μ -stress maps collected of the epitaxially grown 3C-SiC film by Lee *et al.* [1].

It should be noted that the TO mode frequency of the polycrystalline 3C-SiC recorded by Lee *et al.* was red shifted 3 cm^{-1} from the crystalline 3C-SiC TO mode frequency of 796 cm^{-1} . Lee *et al.* attributed the red shift to stacking faults in the polycrystalline SiC based on the results from Romfeld *et al.* [29]. Romfeld *et al.* illustrated the TO peak of polycrystalline 3C-SiC as deposited in Figure 2.19 (a). Then, by laser annealing the sample, they were able to remove the stacking faults. Figure 2.19 (b) shows the narrowing the line shape, removal of the shoulder and a blue shift in the peak to match the TO mode frequency of crystalline 3C-SiC after the laser anneal. They further demonstrated the effects of stacking faults by computer simulation [29]. This information becomes important because the Raman spectrum of the poly-SiC used for this work appears to have a large amount of stacking faults with a red shift of the TO peak of 5 cm^{-1} .

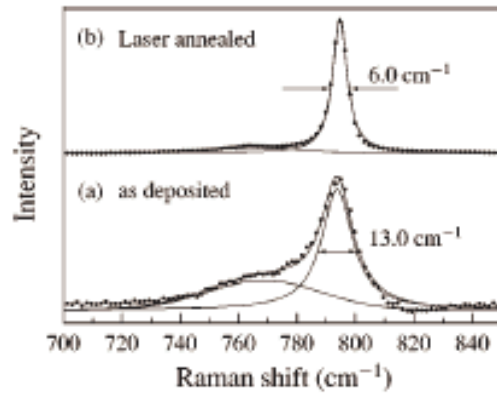


Figure 2.19 TO peak in 3C poly-SiC (a) as deposited and (b) after laser annealing at 1700 K [29].

2.8 Chapter Summary

Chapter I gave an introduction to the problem of detecting residual stress in SiC MEMS. This chapter explained the background information necessary to understand the problems faced in the characterization of residual stress in SiC MEMS. Chapter III will introduce the specific SiC structures that were evaluated in this research.

III. Samples

The introduction discussed the objective of this research, which is the detection of residual stress in SiC MEMS. A review of the history and characteristics of SiC MEMS was also covered. In this chapter, the materials that were investigated in this research are described. The samples evaluated were fabricated from two different polytypes of SiC. The first set of samples were MEMS fabricated from 6H-SiC and the second were thin films of polycrystalline 3C-SiC deposited on (100) Si substrates (referred to as poly-SiC). This chapter describes the structure of the samples.

3.1 NASA crystalline 6H-SiC accelerometer and pressure sensor

The NASA MEMS pressure sensors are described in detail to provide enough background to appreciate and understand the results of the experimental analysis. For a complete description of the device function see references [8, 30].

3.1.1 Layout and Function. The design of the NASA MEMS pressure sensor/accelerometer tested in this thesis is shown in Figure 3.1. Figure 3.1 (a) shows the cross-section of the MEMS pressure sensor fabricated from a high resistivity ($7\ \Omega\text{-cm}$) p-type SiC 6H-SiC $50\text{-}\mu\text{m}$ thick diaphragm, and the $250\text{-}\mu\text{m}$ thick edges. As a load is applied normal to the diaphragm, both compressive and tensile forces can be monitored by piezoresistive elements formed from an n-type epitaxial layer ($3.8 \times 10^{18}\ \text{cm}^{-3}$) on the top surface of the diaphragm (see Figure 3.1 (c)). The piezoresistive elements are arranged into a Wheatstone bridge (see Figure 3.1 (b)) so that a change in the resistance of the piezoresistors, due to flexing of the diaphragm, results in a corresponding change in voltage across the bridge. From Figure 3.1 (c), the (highlighted) resistors labeled #1 and #3 are identical in dimensions and they cross the edge of the diaphragm at the same point. Likewise, resistors labeled #2 and #4 are identical and are placed at the mirrored positions on the diaphragm. Therefore, the resistances of piezoresistors #1 and #3 and the resistances of #2 and #4 are intended to be identical. Due to the matching of resistances,

an enhancement of the output of the Wheatstone bridge should occur. In Figure 3.1 (c), the diaphragm is apparent in the optical micrograph as a dark circle, due to the material's transparency. The rectangular dark regions that the resistive elements are connected to are metal contacts. The device is packaged and the carrier leads are wire bonded to the metal contacts [31]. There are two different devices that are tested: one with a diaphragm radius of $650\text{ }\mu\text{m}$, and another with a diaphragm radius of $550\text{ }\mu\text{m}$.

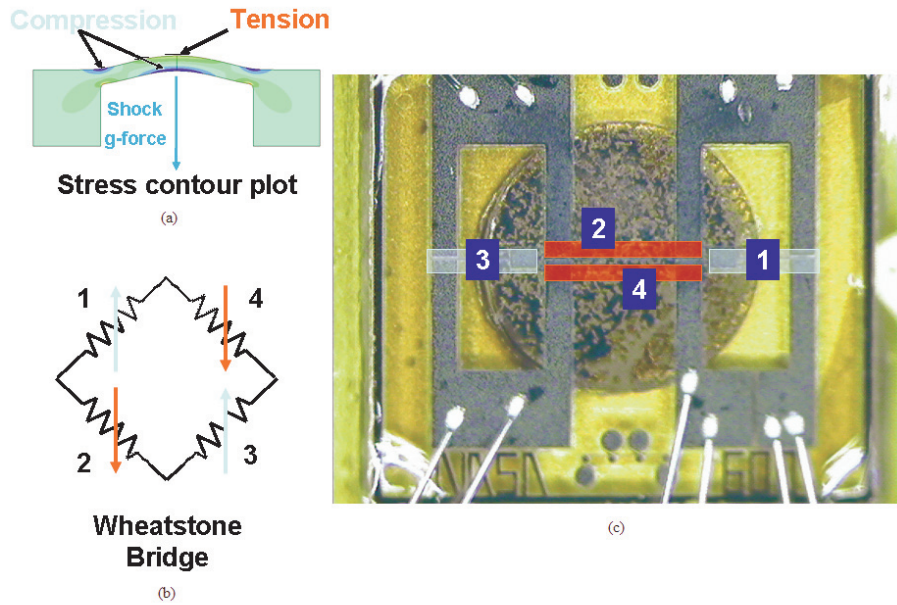


Figure 3.1 (a) Cross-section of 6H-SiC MEMS diaphragm indicating points of stress from a shock. (b) Layout of the resistive elements forming a Wheatstone bridge. (c) Top view of the NASA 600 sample with highlights over the piezoresistive elements [31].

3.1.2 Resistivity of the piezoresistors #2 and #4 . The 6H-SiC structures are bulk micro-machined by back-etching a $250\text{-}\mu\text{m}$ thick single-crystal 6H-SiC wafer (p-type, $7\text{ }\Omega\text{-cm}$) that includes a plasma enhanced chemical vapor deposition (PECVD) deposited 6H-SiC $5\text{-}\mu\text{m}$ epitaxial film ("epi-layer") (n-type, doped $3.8 \times 10^{18}\text{ cm}^{-3}$) on the top surface of the wafer. The length of the piezoresistors #2 and #4 is $400\text{ }\mu\text{m}$ and the cross-sectional area is $40\text{ }\mu\text{m} \times 5\text{ }\mu\text{m}$. The dopant for the epitaxial layer is nitrogen (N) [32]. N

is a shallow donor in 6H-SiC with ionization energies that have been measured between 0.085 and 0.125 eV [33].

According to Sze [20], the resistivity for an n-type semiconductor is defined as

$$\rho = \frac{1}{qn\mu_n} \quad (3.1)$$

where μ_n is electron Hall mobility in ($cm^2V^{-1}s^{-1}$), q is the elementary charge, $1.602 \times 10^{-19}C$, and n is the electron or majority carrier concentration (cm^{-3}). The resistance, R , of an element of length, l , and area, A , is

$$R = \rho \frac{l}{A} = \frac{l}{Aqn\mu_n}. \quad (3.2)$$

With a donor dopant level $N_D = 3 \times 10^{18}cm^{-3}$ at $T = 300^\circ K$, the electron Hall mobility is $\mu_n \approx 100 - 300(cm^2V^{-1}s^{-1})$ (see Figure A.1). Since the donor ionization energies are greater than $3kT$, where k is Boltzman's constant, $1.38 \times 10^{-23} \frac{J}{K}$, and T is temprature (K), away from the conduction band (i.e., $0.085 eV > 3kT = 0.075 eV$), the dopants will not be fully ionized.

To determine the number of ionized majority carriers, the following equation from Wolf *et al.* [34] must be balanced since

$$n + N_A^- = p + N_D^+ \quad (3.3)$$

where p is the hole or minority carrier concentration (cm^{-3}), n is the electron or majority carrier concentration, N_A^- is the number of fully ionized acceptors, and N_D^+ is the number of fully ionized donors. From Sze [20],

$$n = N_c e^{-(E_C - E_F)/kT} \quad (3.4)$$

and

$$p = N_v e^{-(E_f - E_v)/kT}, \quad (3.5)$$

where N_c is the density of states in the conduction band (cm^{-3}), N_v is the density of states in the valence band, E_f is the Fermi energy level (eV), E_v is the energy of top the edge of the valance band, E_c is the energy of the bottom edge of the conduction band. From Levinshtein *et al.* [33],

$$N_c \cong 1.73 \times 10^{16} \times T^{3/2} (cm^{-3}) \quad (3.6)$$

and

$$N_v \cong 4.8 \times 10^{15} \times T^{3/2} (cm^{-3}). \quad (3.7)$$

The number of ionized dopants are found by [34]

$$N_A^- = \frac{N_A}{1 + 4e^{(E_A - E_f)/kT}} \quad (3.8)$$

and

$$N_D^+ = \frac{N_D}{1 + 2e^{(E_f - E_D)/kT}}. \quad (3.9)$$

Finally, the Varshney equation, which gives the energy gap as a function of lattice temprature, for 6H-SiC is [33]

$$E_g = E_g(0) - 6.5 \times 10^{-4} \times \frac{T^2}{T + 1200} (eV). \quad (3.10)$$

By substituting (3.4)-(3.9) into (3.3) [35]:

$$0 = N_v e^{-(E_f - E_v)/kT} - N_c e^{-(E_c - E_f)/kT} + \frac{N_D}{1 + 2e^{(E_f - E_D)/kT}} - \frac{N_A}{1 + 4e^{(E_A - E_f)/kT}}, \quad (3.11)$$

the value of E_f can be found relative to both E_c and E_v . By setting $E_v = 0$ and , then $E_c = E_g$; Equation (3.11) becomes

$$0 = N_v e^{-E_f/kT} - N_c e^{(E_f-E_g)/kT} + \frac{N_D}{1 + 2e^{(E_f-E_g+E_D)/kT}} - \frac{N_A}{1 + 4e^{(E_A-E_f)/kT}}. \quad (3.12)$$

E_f is found by finding the roots of Equation (3.12). Equation (3.9) is solved to determine the number of ionized majority carriers. By substituting the value of $n = N_D^-$, ρ and R can be found. Figure 3.2 is a plot of the ideal resistances for piezoresistors #2 and #4 on the 550 NASA sample based on these equations and calculations. (Matlab code is included in Appendix C. Measured resistances for these piezoresistors will be given in Section 5.1.1)

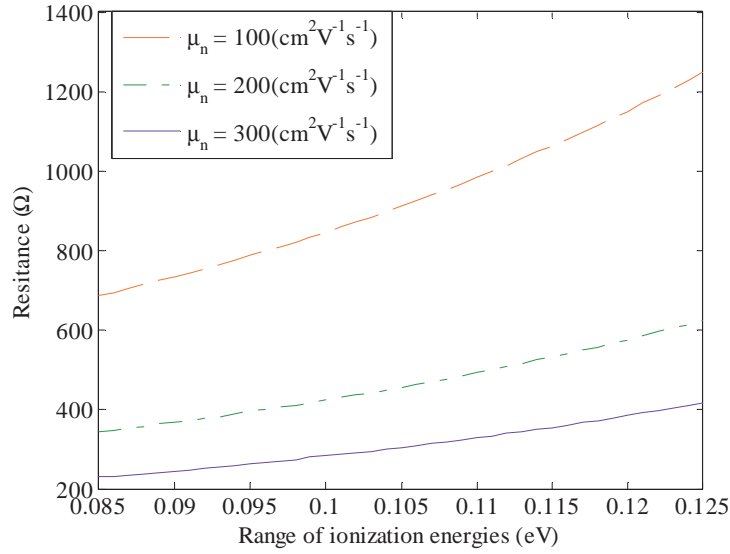


Figure 3.2 The resistance of piezoresistors #2 and #4, which are PECVD deposited 6H-SiC strips of 5- μm epitaxial layers (n-type, doped $3.8 \times 10^{18} \text{cm}^{-3}$) on the top surface of the wafer. The length of the resistors is $l = 400 \mu\text{m}$ and the cross-sectional area is $A = 40 \mu\text{m} \times 5 \mu\text{m}$. The dopant for the epitaxial layer is N.

3.2 Cree 6H-SiC wafers

The NASA MEMS pressure sensors are fabricated from 3.52° off-axis Cree wafers of 6H-SiC with an n-type epitaxial layer deposited on the top surface. In order to investigate the phonon deformation potential, two wafers of the 6H-SiC were acquired and are depicted in Figure 3.3. The CR07809-43 wafer is cut at 0.39° off axis and was used for the phonon deformation potential experimental determinations.

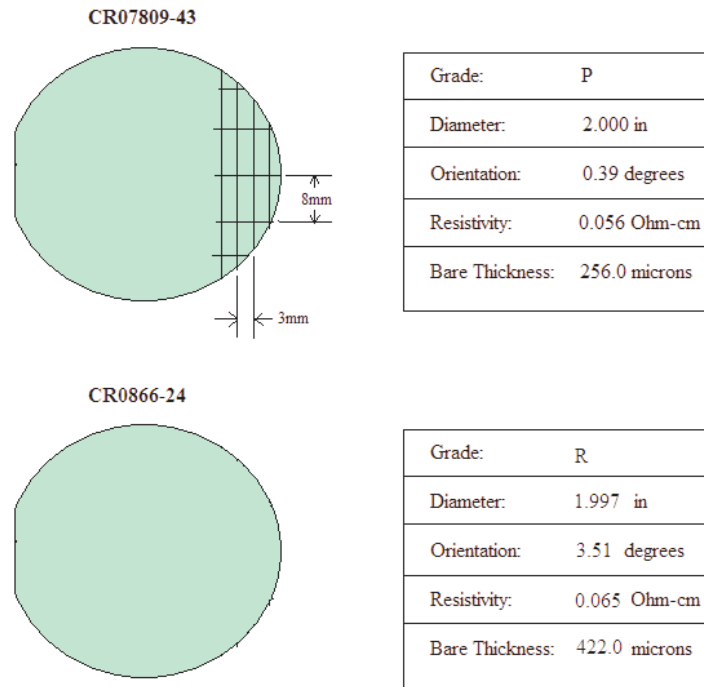


Figure 3.3 Layout and specifications of two Cree 6H-SiC wafers used to determine phonon deformation potentials.

3.3 FLX poly-SiC Thin Films

Flx Micro Inc. produced the thin films of polycrystalline 3C-SiC (poly-SiC) deposited by low-pressure chemical vapor deposition (LPCVD) [36] on the (100) Si substrates, used for evaluation by Raman spectroscopy in this research. Poly-SiC has an advantage over single-crystal SiC in the fabrication of MEMS because it can be deposited

on a sacrificial layer of Si dioxide (SiO_2) or an electrically insulating layer of Si Nitride (Si_3N_4) film [6]. Thus, the interest in measuring the Raman Shift for the characterization of stresses in poly-SiC for MEMS structures was of interest here.

3.3.1 1.5- μm SiC on Si. A schematic cross-section of the 1.5- μm poly-SiC on Si substrate is illustrated in Figure 3.4 (a). In Figure 3.4 (b), an optical micrograph was taken displaying a metal mask of a comb drive that was deposited on top of the poly-SiC. The magnification is 5X and the green dot in the middle is the laser spot of a 514-nm argon-ion laser through the confocal microscope. (For more details on the microscope setup, see the equipment chapter on the Raman spectrometer.)

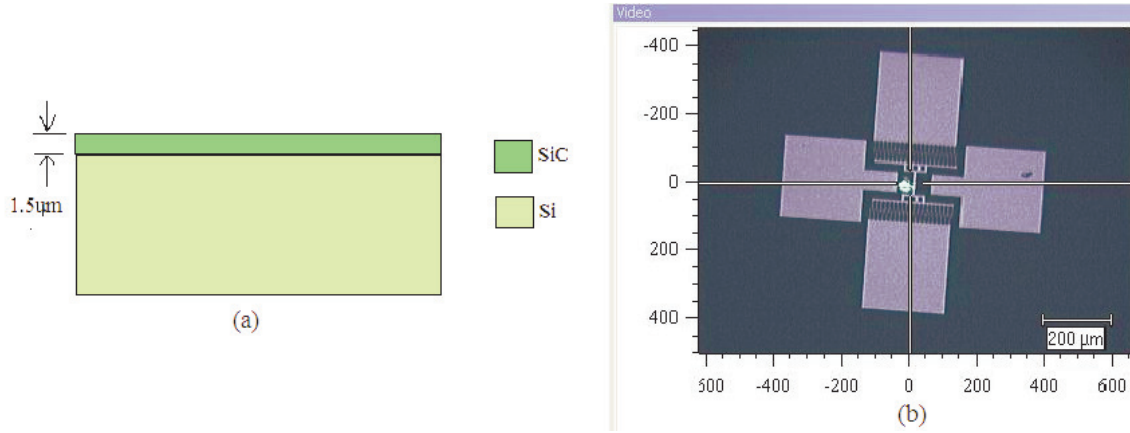


Figure 3.4 (a) Cross-section of the 1.5- μm thick poly-SiC deposited by LPCVD [36] on a Si substrate. (b) Microscope image of the top of the FLX Micro inc. 1.5- μm poly-SiC on a Si substrate. The comb drive is a metal mask deposited onto the thin film.

3.3.2 5.5- μm SiC on Si. A schematic cross-section of the 5.5- μm SiC thin films is depicted in Figure 3.5 (a). After the films were deposited, the back side of the wafers were anisotropically etched by potassium hydroxide (KOH), leaving a suspended membrane of SiC. In 3.5 (b), an optical micrograph of the top surface of the 5.5- μm thin film is shown. The membrane was fractured during transport and dropped below the support structure (the dark shape in the middle of the picture). The picture is shown to reveal the edge of the diaphragm. Intact samples were used for all Raman spectral

analysis. The image was again taken through a 5X objective showing the suspended membrane to be 1 mm x 1 mm.

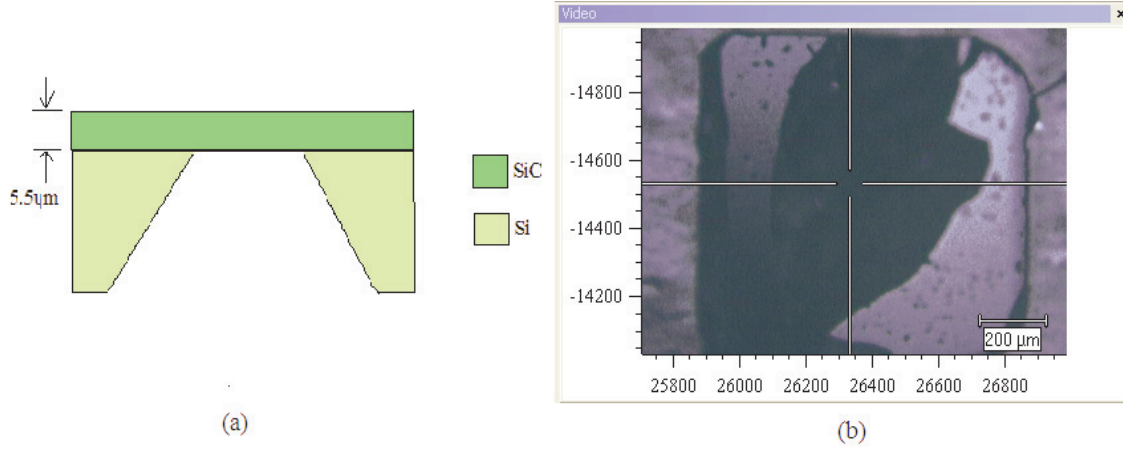


Figure 3.5 (a) A cross-section of the 5.5- μm thick poly-SiC deposited by LPCVD [36] on a Si substrate. The Si substrate is back-etched to produce a suspended membrane of SiC. (b) Optical micrograph of the top surface of the 5.5- μm thin film. The membrane was fractured during transport and dropped below the support structure. The image is shown to reveal the edge of the diaphragm. Intact samples were used for all Raman measurements.

3.3.3 Optical Properties of SiC . One important factor to consider when determining the Raman spectrum of SiC is the material's absorption coefficient, α . At a laser wavelength of $\lambda_{uv} = 325 \text{ nm}$, the photon energy, $E_{uv} = 3.81 \text{ eV}$, is 1.45 eV above the bandgap energy of 3C-SiC, $E_{g_{3C}} = 2.36 \text{ eV}$ (see Figure A.5). Correspondingly, the absorption, $\alpha = 3660 \text{ cm}^{-1}$, is high (see Table A.1). Conversely, for a laser wavelength, $\lambda_{green} = 514 \text{ nm}$, the photon energy, $E_{green} = 2.4 \text{ eV}$, is only 0.04 eV above $E_{g_{3C}}$. Due to the fact that 3C-SiC is an indirect bandgap material and E_{green} is only 0.04 eV, above the $E_{g_{3C}}$, its absorption is $\alpha \approx 100 \text{ cm}^{-1}$ at a wavelength, $\lambda_{green} = 514\text{-nm}$ (see Figures A.4 and A.5). In Figure 3.6, the amount of light that is transmitted through the SiC, T, is plotted as a function of thickness, d. For both of the absorptions at 514-nm and at 325-nm wavelengths (see Appendix C for .m file), the following relationship was used to produce Figure 3.6:

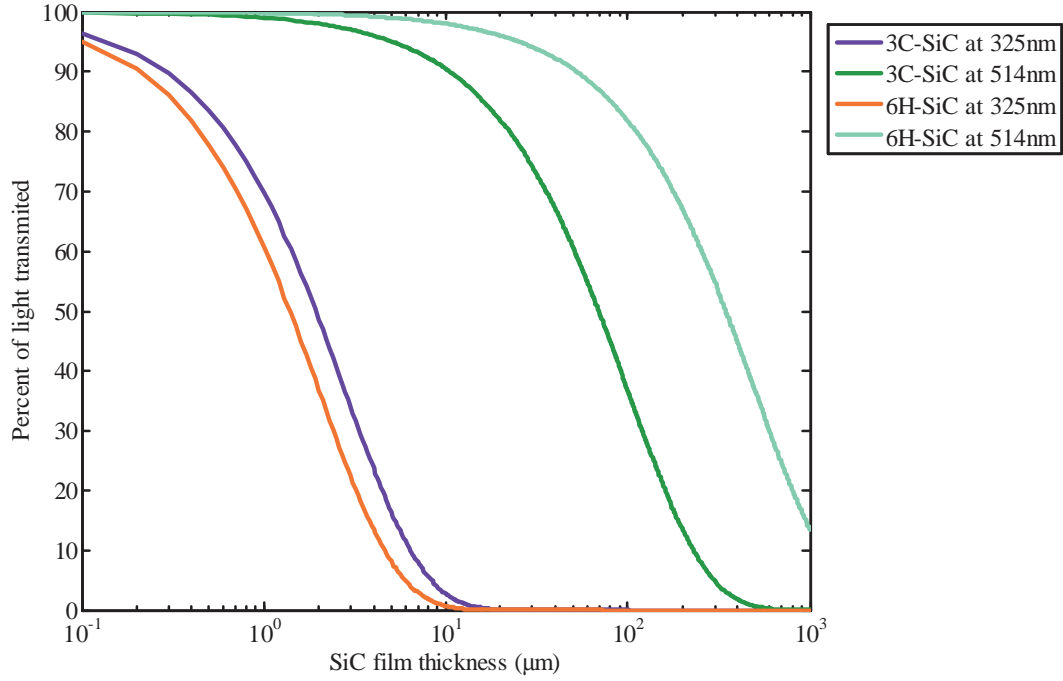


Figure 3.6 Percent of light transmitted as a function of thickness of SiC by the 325 nm and 512 nm lasers for both 6H and 3C polytypes. 3C-SiC absorption values come from Figures A.1 and A.4. 6H-SiC absorption values come from Figures A.2 and A.3.

$$T = e^{-\alpha d} \quad (3.13)$$

The data become important when looking at thin films by Raman spectroscopy because it gives an indication of how much light will reach the Si substrate which is highly Raman active for many wavelengths. Also included is the absorption of 6H-SiC for both wavelengths at $\lambda = 514 \text{ nm}$, $\alpha \approx 20 \text{ cm}^{-1}$ (See Figure A.3) and at $\lambda = 325 \text{ nm}$, $\alpha \approx 5 \times 10^3 \text{ cm}^{-1}$ (See Figure A.2).

3.4 Chapter Summary

In this chapter, samples fabricated from two different polytypes of SiC that were investigated were described. The first one was MEMS fabricated from 6H-SiC and

the second set of samples were thin films of polycrystalline 3C-SiC deposited on (100) Si substrates (referred to as poly-SiC). The next chapter describes the characterization methods used to study the samples.

IV. Equipment and Experiments

The equipment for characterization of the SiC samples described in Chapter III are introduced in this section. More detailed information is available on most of the equipment through the manufacturers. Experimental procedures are also outlined.

4.1 Probe Station

A four-point probe station seen in Figure 4.1 was used to measure the resistances of the piezoresistive elements on both the NASA 550 and 650 MEMS pressure sensors. The probe station is powered with a Hewlett Packard 41501A source/monitor unit (SMU) and pulse generator expander, and the current-voltage (I-V) curves are recorded by a Hewlett Packard 4155A semiconductor analyzer. (For more information see

http://www.home.agilent.com/upload/cmc_upload/All/55A90015.pdf)

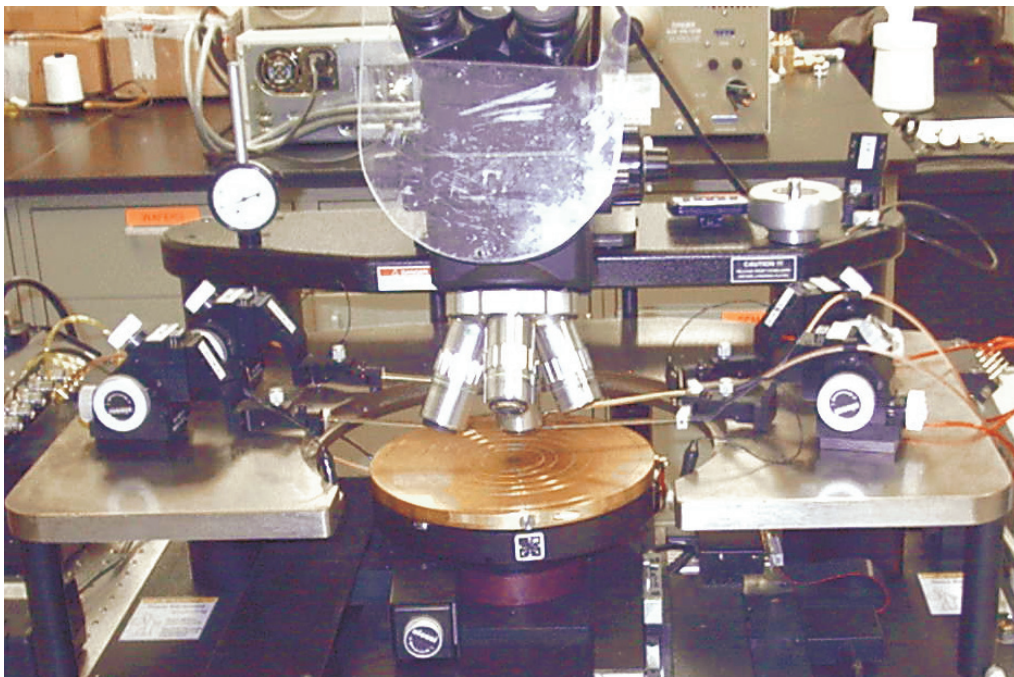


Figure 4.1 Four-point probe station used to measure the resistance of piezoresistive elements.

One probe needle was placed in contact with the metal contact pad on either side of the piezoresistive element as illustrated in Figure 4.2. Once the contacts were in place, the voltage was swept from 0 to 10 V and the corresponding current was recorded. The resistance was in turn determined by the slope of the I-V line. Three measurements were taken across each resistive element.

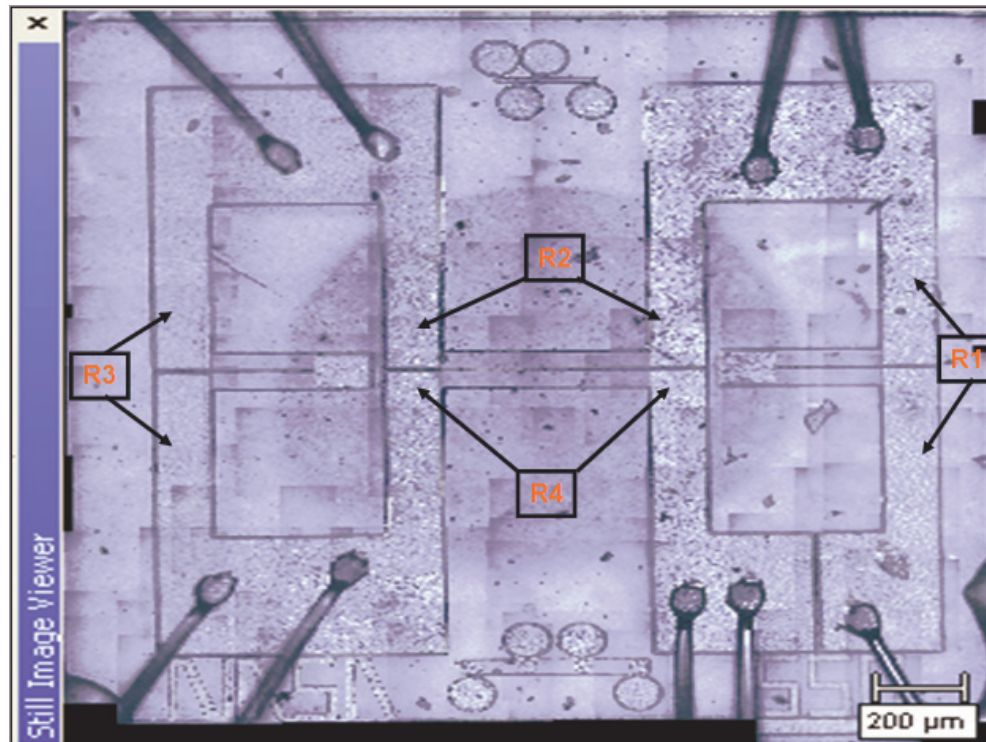


Figure 4.2 The text boxes label the measurement taken and the arrows indicate where the probe needle for the resistance measurement was placed on the device.

4.2 Scanning Electron Microscope

The scanning electron microscope (SEM) creates images of surface features of the NASA pressure sensors which look three-dimensional and help to investigate the visible features. The SEM has the advantage over optical microscopy because of its large depth of field and many different levels of magnifications. The SEM requires the samples to be in a stable vacuum condition for the electron irradiation. To view insulating materials,

a gold coating is needed to produce a conducting surface and to prevent electrical charge effects. For SiC, the coating is not required because of its conduction properties [37].

4.2.1 AMRAY 1810 (1990). The AMRAY 1810 is considered a "bottom of the range SEM but with the advantage of being of the new generation of digital imaging instruments having many automatic features [37]." The AMRAY SEM has a resolution of 5 nm with an efficient back scattered detector for the atomic number imaging. The SEM has a personal computer (PC) controlled system and a thin window germanium detector which can detect elements above beryllium in the periodic table. Several software packages were available: SEMQUANT - quantitative bulk analysis, AUTOBEAM - basic electron image acquisition, SPEEDMAP - high speed X-ray mapping, and IMQUANT - image processing. The system PC runs on Windows NT 4.0, which allows the user to capture and transfer digital images [37]. A digital image of the AMRAY 1810 can be seen in Figure 4.3.



Figure 4.3 AMRAY 1810 SEM.

4.3 Zygo Interferometer

The Zygo NewView was used to acquire three-dimensional surface structure data of the pressure sensor for analysis. The system combines graphic images and high resolution numerical analysis to accurately characterize the surface structure of the samples. The NewView utilizes scanning white light interferometry in order to image and measure the micro-structure and topography of surfaces in three dimensions [38]. A schematic of the NewView Zygo interferometer system is shown in Figure 4.4.

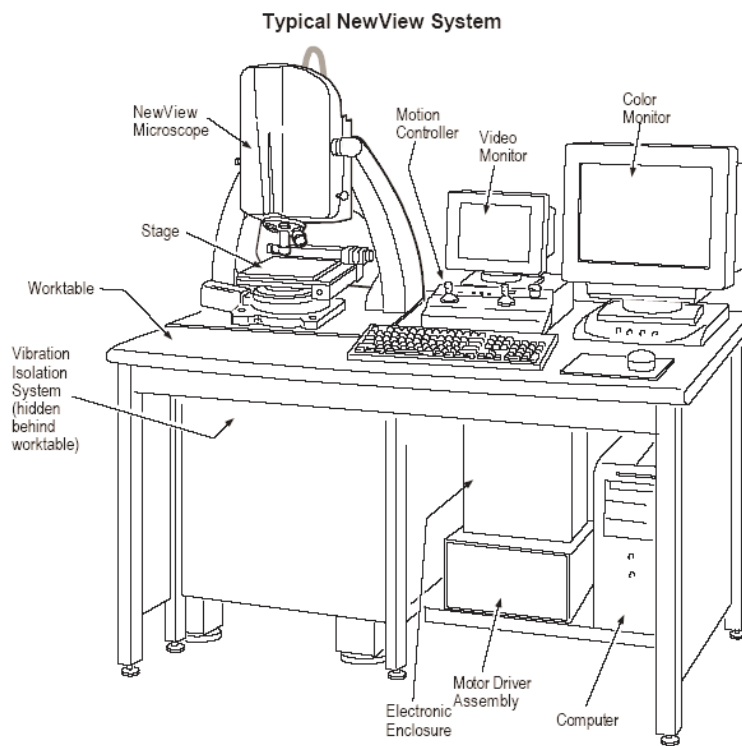


Figure 4.4 Diagram of the New View Zygo interferometer system [38].

4.4 InVia Raman Spectrometer

A schematic of the InVia Raman spectrometer, produced by Renishaw Inc., is shown in Figure 4.5. The laser light enters the system and first passes through a beam expander (labeled E) in order to collimate the light. The beam is guided through to the confocal microscope where it is focused through by an objective onto the investigated sample (with

50X objective, the spot size is $\sim 1\ \mu\text{m}$ in the focal plane). The samples are placed on the piezoelectric stage in the focal plane of the microscope (labeled A). The light reflects off the samples back through the microscope, and is passed through a notch filter (D) to reduce the intensity of the Rayleigh line without affecting the Raman shift intensity. The light then passes through the entrance slit (B) to the monochromator. Light reflects off of the triangle mirror and is dispersed by a grating with a number of lines per mm corresponding to the excitation wavelength. The dispersed light is then passed through the $50\text{-}\mu\text{m}$ exit slit onto a CCD array (F) [39].

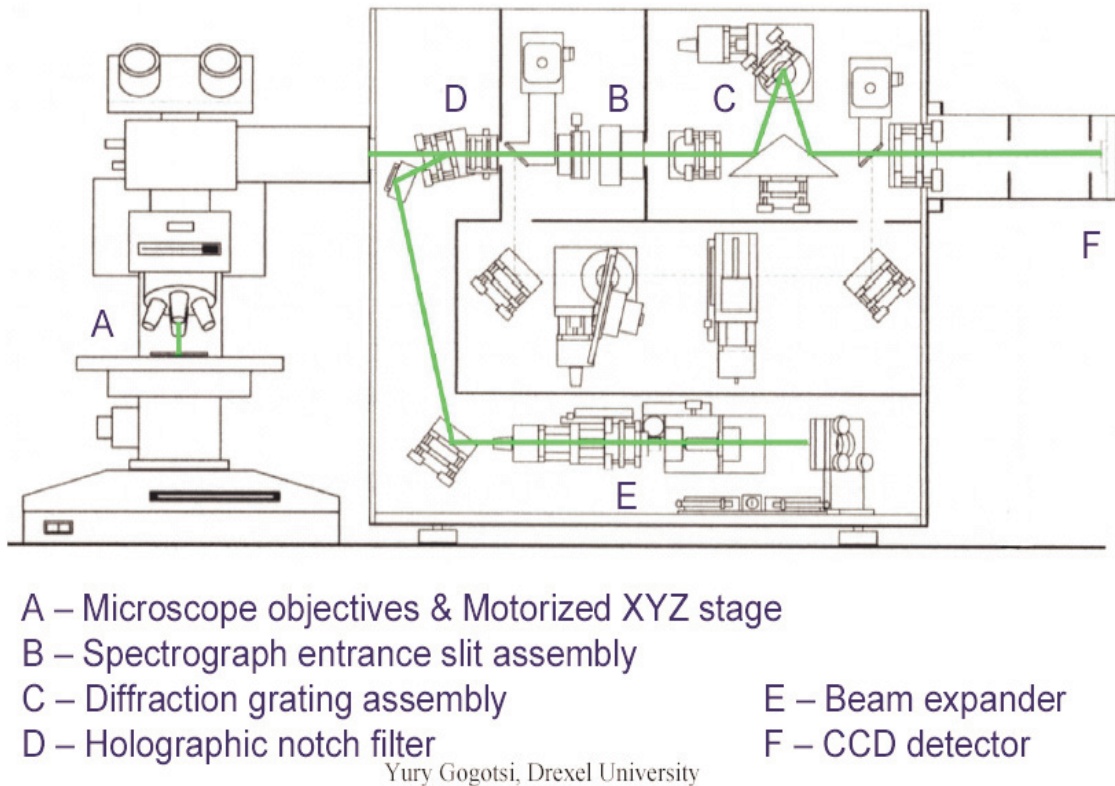


Figure 4.5 Diagram of a Renishaw Raman spectrometer [39].

4.4.1 Spectral Resolution. The InVia Raman spectrometer is based on a single monochromator. Therefore, the resolution of the spectrometer for the wavelengths of 325-nm (UV) and 514-nm (green) may be calculated using the following equation:

$$\Delta\lambda = \frac{wa}{fm}, \quad (4.1)$$

where w is the slit width, a is grating tooth spacing, f is the focal length of the monochromator and m is the diffraction order. Examples for some of the wavelengths relevant to this work are worked out below using the data from Renishaw.

Example 1 $\lambda = 325 \text{ nm}$;

$$\Delta\lambda = \frac{a}{fm}w = \frac{1}{200 \text{ mm} \times 2400(1/\text{mm})} 50 \mu\text{m} = 1.0417 \times 10^{-10} \text{ m}$$

$$\Delta\nu = \frac{1}{\lambda^2} \Delta\lambda = \frac{1}{(325 \text{ nm})^2} \times 1.0417 \times 10^{-10} \text{ m} = 9.8622 \text{ cm}^{-1}$$

Example 2 $\lambda = 514 \text{ nm}$;

$$\Delta\lambda = \frac{a}{fm}w = \frac{1}{200 \text{ mm} \times 1800(1/\text{mm})} 50 \mu\text{m} = 1.3889 \times 10^{-10} \text{ m}$$

$$\Delta\nu = \frac{1}{\lambda^2} \Delta\lambda = \frac{1}{(514 \text{ nm})^2} \times 1.3889 \times 10^{-10} \text{ m} = 5.2571 \text{ cm}^{-1}$$

Example 3 $\lambda = 1064 \text{ nm}$;

$$\Delta\lambda = \frac{a}{fm}w = \frac{1}{200 \text{ mm} \times 1200(1/\text{mm})} 50 \mu\text{m} = 2.0833 \times 10^{-10} \text{ m}$$

$$\Delta\nu = \frac{1}{\lambda^2} \Delta\lambda = \frac{1}{(1064 \text{ nm})^2} \times 2.0833 \times 10^{-10} \text{ m} = 1.8402 \text{ cm}^{-1}$$

Table 4.1 shows some of the advertised capabilities of the InVia Raman spectrometer found on the world wide web (<http://www.renishaw.com/UserFiles/acrobat/UKEnglish/SPD-TN-014.pdf>). It should be noted that the advertised spectral resolution is only for the configuration with the infrared (IR) laser, and that the laser wavelengths used for the Raman experiments (325 nm and 514 nm) do not provide the advertised spectral resolution. Four different lasers with the following wavelengths; 830 nm, 633 nm, 514 nm and 325 nm, are available at AFRL/ML. Renishaw Inc. has provided a spread sheet that will calculate the spectral resolution and other important parameters. A snap shot of the results for 514-nm and 325-nm wavelengths can be found in the Appendix B Figures B.3 and B.2. The spectral resolution computed by the Renishaw's spread sheet closely matches the results of the spectral resolution based on the monochromator equations above.

Table 4.1 Renishaw InVia Raman spectrometer advertised capabilities.

Description	Renishaw's inVia Raman microscope
Wavelength coverage	$\sim 10 \text{ cm}^{-1}$ to 9000 cm^{-1}
Laser options	multiple, from 244 nm to 830 nm
Detector	Si CCD
Noise limitation	signal shot noise limited
Microscope spatial resolution	$< 1 \text{ }\mu\text{m}$ (depending on configuration)
Spectral resolution	$\sim 1 \text{ cm}^{-1}$ (depending on configuration)

4.4.2 Sampling Rate. The InVia Raman spectrometer has variable spectral resolution based on the wavelength of the excitation source. Therefore, the sampling rate must be dynamic. Raman spectra will be explained further in the results section, but Figure 4.6 (a) and (c) depict the two typical spectra. Figure 4.6 (a) is the Raman spectrum of diamond powder, which has a main Raman peak with a line center at 1331 cm^{-1} relative to the 325-nm laser line defined as 0 cm^{-1} . Figure 4.6 (b) is a close up view of the Raman line of the diamond powder showing only the data points collected which demonstrates the sampling rate of the InVia Raman spectrometer using a 325-nm source to be 3 cm^{-1} . Figure 4.6 (c) is the Raman spectrum of 6H-SiC which has an LO Raman peak line center at 966 cm^{-1} and is excited using a 514-nm laser. Figure 4.6 (d) is a close-up view of the LO peak showing the sampling rate with a 514-nm source to be 2 cm^{-1} .

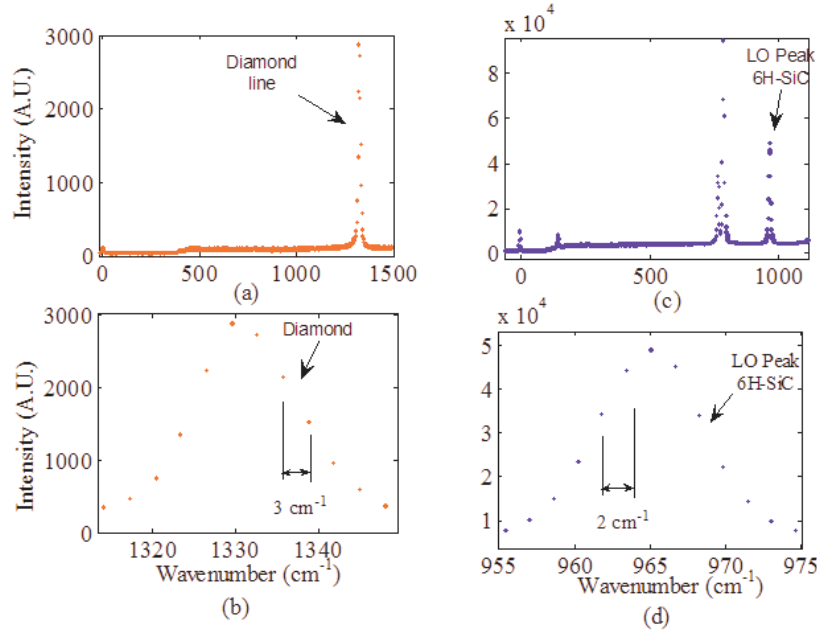


Figure 4.6 (a) Raman spectrum of diamond powder using a 325-nm excitation source. (b) Raman peak of diamond powder at 1331 cm^{-1} showing the range between sampling points. (c) Raman spectrum of 6H-SiC using a 514-nm excitation source. (d) LO peak of 6H-SiC a 966 cm^{-1} using a 325-nm excitation source.

4.5 Four-point Strain Fixture

Two methods were attempted to quantify the phonon deformation potential for the 6H-SiC. The first method utilized a four-point strain fixture (Figures 4.7 (a) and (b)) that is similar to the methods used by Starman and Lee *et al.* [1, 16]. The dimensions can be found in Appendix B, Figure B.1. Strips of 6H-SiC were cut from the CR07809-43 Cree wafer as shown in Figure 3.3 and epoxied to a piece of Plexiglas along with a Vishay EA-06-125AD-120 precision strain gauge using M-bond 200 epoxy, also from Vishay Inc. The Plexiglas piece is placed above the V-shaped part and below the metal cross rods. The V-shaped part is pushed upwards by a bolt (seen in the back of Figure 4.7 (b)). A compressive force is applied to the Plexiglas piece between the two metal cross rods. The strip of 6H-SiC and the strain gauge epoxied to the top surface of the Plexiglas are also compressed, resulting in a strain that can be monitored by a P-3 strain indicator and recorder, discussed in detail later.

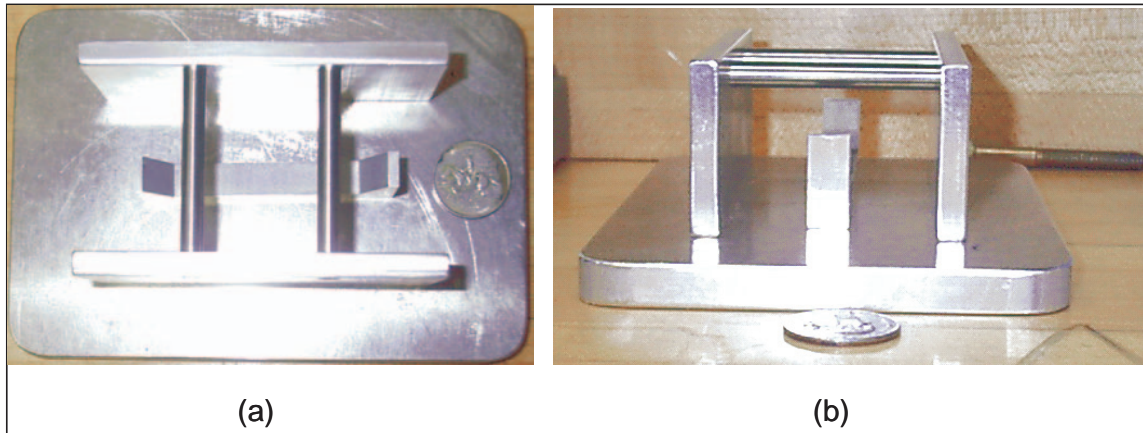


Figure 4.7 (a) Top view of the four-point strain fixture. (b) Sideview of the four-point strain fixture.

4.6 Vice

A second experimental setup to determine the phonon deformation potential of 6H-SiC utilized a vice. A 1-cm² sample of the CR07809-43 Cree wafer had an EA-06-125AD-120 precision strain gauge was epoxied to the unpolished side of the sample using M-bond 200. The sample was placed in a vice as shown in Figure 4.8. A stress was applied directly to the crystal, and the strain on the crystal and strain gauge was monitored by a P-3 strain indicator described in the next section. For each increment of stress applied to the crystal, the corresponding Raman spectrum of the crystal was recorded and curve fit to the line shape using Wire 2.0[®] software to track the shift in the Raman peaks as a function of the applied stress. Note, as the pressure was applied to the crystal the sample slightly buckled upwards producing a tensile stress on the top surface. The buckling was determined optically as a change in the focal plane of the microscope.

A third method for mapping the phonon deformation potential would be to use a diamond anvil cell as reported by Liu *et al.* [28].

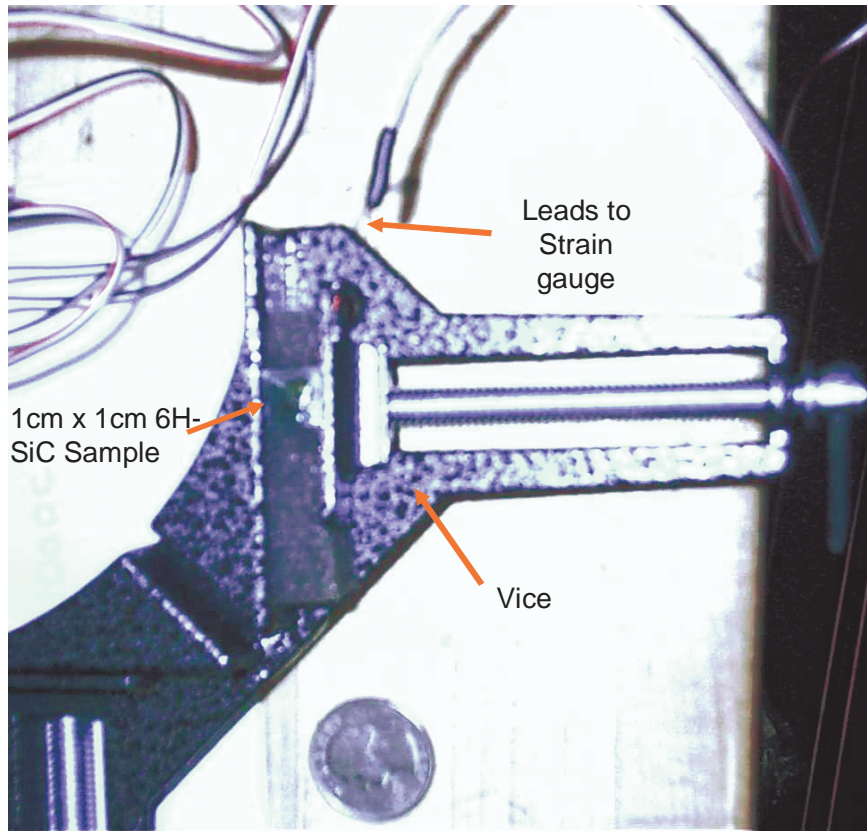


Figure 4.8 Vice setup used to apply stress to a 1-cm x 1-cm square of 6H-SiC with a strain gauge epoxyed to the back side and used to measure the phonon deformation potentials.

4.7 P-3 Strain Indicator and Recorder

The model P3 Strain Indicator and Recorder is an instrument that can measure the strain placed on resistive strain gages. "Proprietary scaling and linearization algorithms provide sophisticated data reduction for strain gauge measurements" [40]. In both experiments used to determine the phonon deformation potential, the strain gauges were wired to a model P-3 strain indicator and recorder (Figure 4.9). In the four-point strain fixture setup, the P-3 was able to monitor the strain applied to the Plexiglas, the strain gauge and the 6H-SiC sample. In the vice setup, it was also able to monitor the strain directly applied to the 6H-SiC crystal 1-cm \times 1-cm square.



Figure 4.9 Photograph of the P-3 strain indicator and recorder from [40].

4.8 Chapter summary

The equipment and methods for characterization of the SiC samples described in Chapter III were discussed in this Chapter. The next chapter will explain the results of these experiments.

V. Results and Data Analysis

The previous chapters introduced the idea that μ -Raman spectroscopy can be used as a method of detecting residual stress in SiC MEMS. The different sample materials were described in Chapter III. This chapter presents and discusses the results of the experiments outlined in Chapter IV.

5.1 NASA 550 and 650 6H-SiC MEMS

The investigation of the NASA MEMS samples led to promising results that are described in the following sections.

5.1.1 Resistance of piezoresistors. In order to determine whether the residual stress measured in the NASA 550 pressure sensor piezoresistors had any effect on the balance of the Wheatstone bridge, the resistances of the piezoresistors were determined by measuring the current-voltage (I-V) relationship using the four-point-probe station (see Section 4.1). From the I-V information, Ohms law,

$$V = i \times R \quad (5.1)$$

was used to back out the resistances. Three measurements were recorded and averaged across each resistor.

Table 5.1 shows the average measured resistances of the four piezoresistors on the NASA 550 and 650 pressure sensors. In Figure 4.2, it was shown where the measurements were taken. On each resistor the resistance was measured three times and the standard deviation was computed using the following spread sheet function

$$\sqrt{\frac{\sum (x - \bar{x})^2}{(n - 1)}} \quad (5.2)$$

where \bar{x} is the average and n is the sample size. The large standard deviation may be attributed to the probe needles penetrating the metal contact pads. Although the range of resistances measured is large, 611-1312 Ω , it does correspond to the resistances predicted for these samples in Section 3.1.2.

Table 5.1 Measured resistances of the piezoressitors on the NASA 550 and 650 MEMS sensors with the corresponding standard deviation of the measurements.

Piezoresistors	R1 (Ω)	SD1(Ω)	R2 (Ω)	SD2(Ω)	R3 (Ω)	SD3(Ω)	R4 (Ω)	SD4(Ω)
NASA 650	1312	455	874	45.3	993	38.3	997	63
NASA 550	1256	6	806	223	611	80	646	173

5.1.2 SEM's. SEM's of the NASA 550 pressure sensor were taken to identify any irregular features in the MEMS device, and to show some of the MEMS features and packaging (Figure 5.1). Note in Figure 5.1 (a) that the NASA 550 MEMS structure is epoxied into a package and the piezoresistors are wired to the package pins. The red boxes indicate the location of the subsequent magnification. The MEMS devices that were magnified and imaged were those that had been identified as having residual stress through Raman spectroscopy (see Figures 5.14 and 5.15). Although a larger amount of stress was identified in the section of resistor #4 (shown circled in red in Figure 5.1 (d)) no irregularities in the chip were found in that location by the SEM.

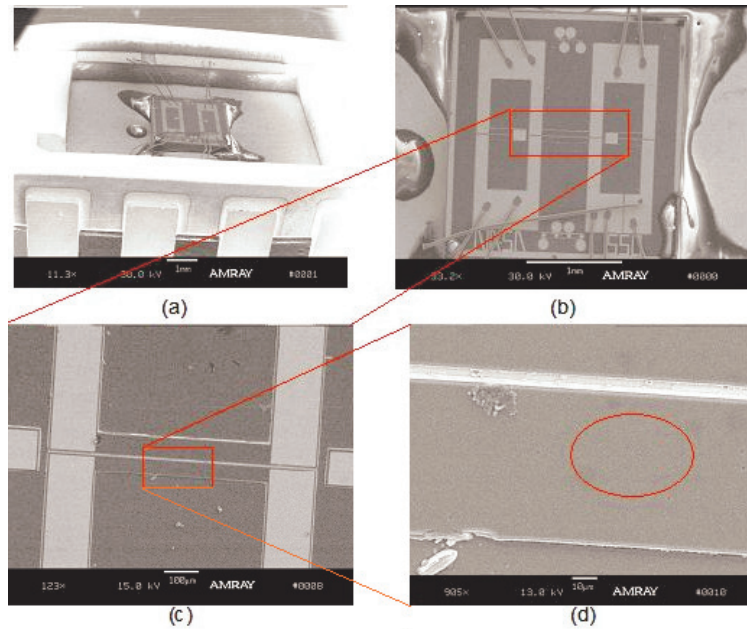


Figure 5.1 (a) SEM of the NASA 550 pressure sensor in packaging at 11.3X magnification. (b) SEM at 33.2X magnification (c) SEM of resistors #2 and #4 at 123X magnification (d) Closeup of resistor #2 where a residual stress was identified using Raman spectroscopy.

Figure 5.2 (a) shows an SEM of the third piezoresistor on the NASA 550 pressure sensor in the location where it crosses the diaphragm. Figure 5.2 (b) shows this location in relation to the rest of the chip. Considerable amounts of residual stress were identified using the Raman spectrometer (see Figure 5.10), yet no visible signs of deformation were observed in the SEM.

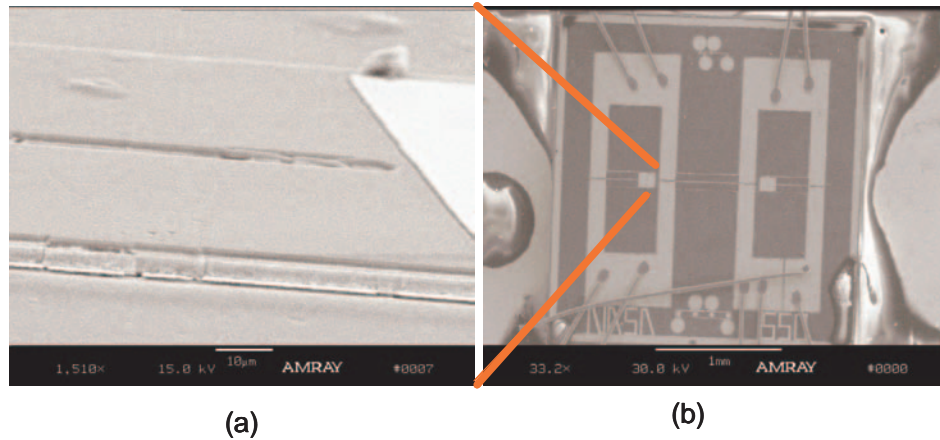


Figure 5.2 (a) SEM of resistor #3 on the NASA 550 pressure sensor in the location where it crosses the diaphragm. (b) SEM of the NASA 550 pressure sensor showing the location of (a)

5.1.3 Zygo Interferometer Data. An interferogram was made with a Zygo interferometer to substantiate that a shift in the Raman spectrum of the resistive element labeled #4 on the 550 NASA sample was caused by residual stress and not by an uneven surface of that piezoresistor. The reason that the surface morphology is important in Raman spectroscopy is that changes in the distance from the objective of the Raman microscope to the object plane can cause a Raman shift if the laser is not refocused. The Zygo, when operated properly, gives accurate measurements of the change in height of the MEMS structures. In Figure 5.3, an interferometric measurement of resistors labeled #2 and #4 (see Figure 3.1) were taken in an area identified as having residual stress by Raman spectroscopy. It can be seen that there are only changes in their height where the epilayer is grown, but that those structures are level on top and would not cause a Raman shift. The two ellipses in green can be used as a reference to compare the interferogram with the Raman map in Figure 5.15. Note that there are no visible defects in Figure 5.3 in the location of the residual stress shown in Figure 5.15, and that the area is completely level from the interferogram.

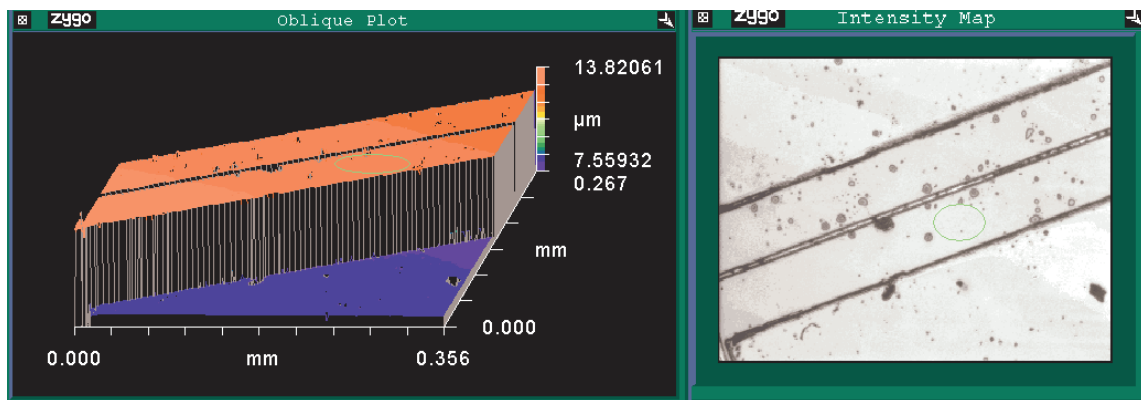


Figure 5.3 An interferogram and a optical micrograph of the resistors #2 and #4 on the NASA 550 sample in a location where isolated residual stress was detected using Raman analysis.

Another interferometric measurement was recorded on resistor # 3 on the NASA 550 pressure sensor as shown in Figure 5.4. By Raman analysis, it was shown that as the piezoresistor crosses the edge of the diaphragm, a considerable amount of residual stress was detected (see Figure 5.10) that can effect the operation of the device. However, through simple evaluation of the morphology of the structure, no variations could be detected.

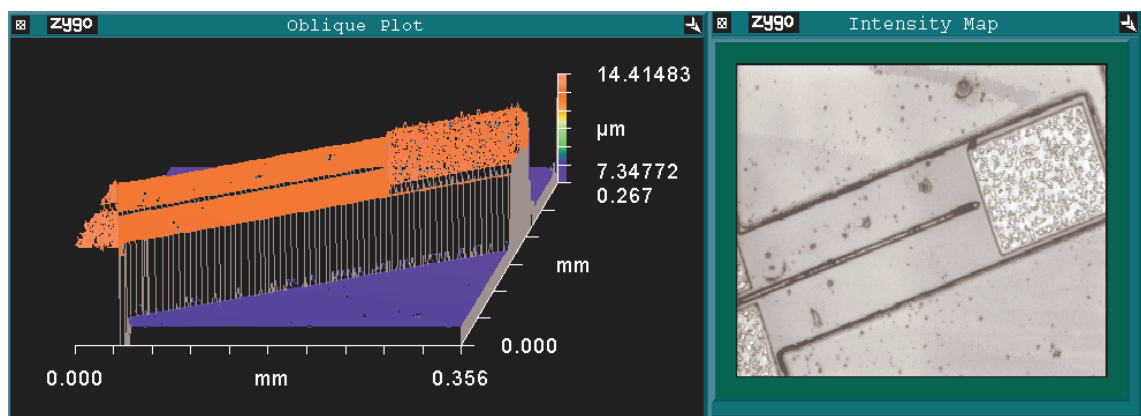


Figure 5.4 An interferogram and an optical micrograph of resistor # 3 on the NASA 550 sample. Residual stress was identified where the resistor crosses the diaphragm by using Raman spectroscopy.

5.1.4 Raman Spectroscopy on the NASA 550 MEMS. Several steps were taken to determine the best way to collect the Raman spectral analysis data on sections of the NASA 550 sample. The successful results are outlined in this section.

5.1.4.1 325-nm versus 514-nm Excitation. In order to determine which frequency of light would be better to perform Raman spectral measurements on the crystalline 6H-SiC MEMS, both an Ar-ion laser with a wavelength of 514 nm and an ultra-violet (UV) laser with a wavelength of 325 nm were used. For the 514 nm laser, a 1800/mm grating is designated and, for the 325-nm laser, a 2400/mm grating is designated. Even though the spectral resolution increases when a grating with a higher density of lines is used, the system configuration still has better spectral resolution by using a 514-nm laser than the setup using the 325-nm laser. In Figure 5.5 (a), the spectrum of crystalline 6H-SiC was recorded using the 514-nm excitation source. The TO1 peak at 766-cm^{-1} , the TO2 peak at 788-cm^{-1} and the LO peak at 966-cm^{-1} are clearly discernible. Each subplot in Figure 5.5 is zoomed in closer onto the TO peaks. In Figure 5.5 (b), the Raman spectrum of crystalline 6H-SiC with a 325-nm laser excitation source is shown. Notice that the spectral lines are less clearly resolved. The two reasons for this are that the spectral resolution of the monochromator in the Raman system is lower for the 325-nm excitation source than for the 514-nm source, and the 325-nm source can cause fluorescence because it exceeds the 3.0 eV band gap of 6H-SiC.

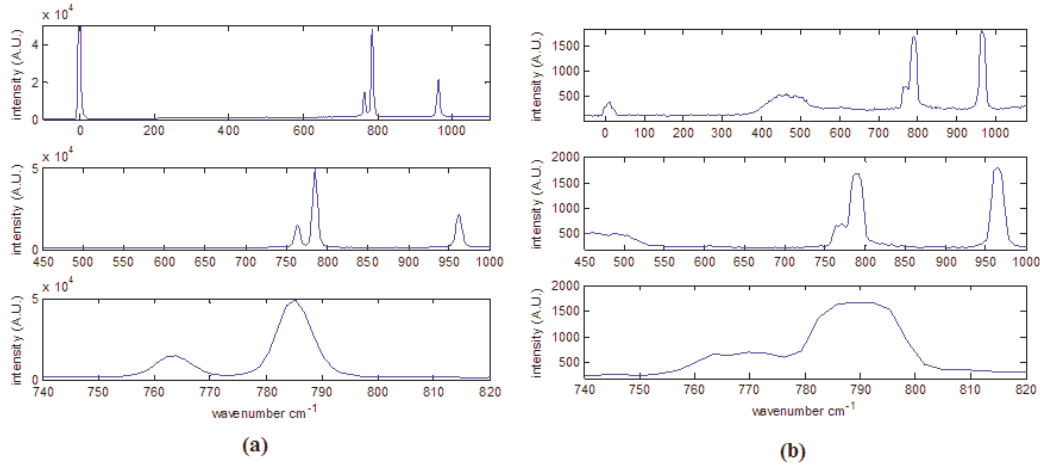


Figure 5.5 (a) Raman spectrum of crystalline 6H-SiC with a 514-nm excitation source using the InVia Renishaw spectrometer. (b) Raman spectrum of crystalline 6H-SiC with a 325-nm excitation source.

5.1.4.2 Baseline Raman Spectra. In order to record the baseline Raman shift of unstressed 6H-SiC, a spectral acquisition was collected on the edge of the 550 NASA sample, away from the diaphragm. The spectral lines match those reported by Brink *et al.* [18]. The spectral lines of the baseline spectrum are labeled in Figure 5.6. The Rayleigh line, also called the laser line, is the reference point for the Raman shift and is centered at 0 cm^{-1} . The folded transverse optical (FTO) lines are $x = 1$ at 766 cm^{-1} , $x = 1/3$ at 788 cm^{-1} , and $x = 0$ at 796 cm^{-1} . The folded longitudinal optical (FLO) line is for $x = 0$ at 966 cm^{-1} . (For convenience, the intense lines at 766 cm^{-1} , 788 cm^{-1} and 966 cm^{-1} will be called TO1, TO2 and LO, respectively.)

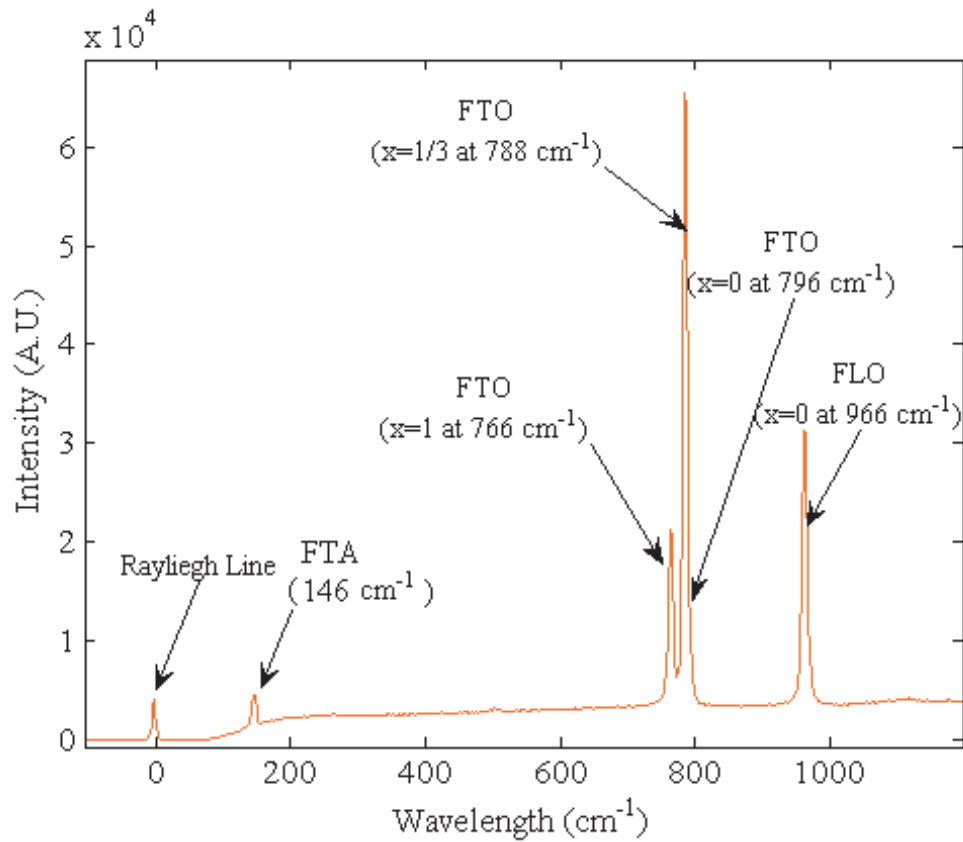


Figure 5.6 6H-SiC Raman spectrum from the edge of the NASA 550 pressure sensor.

5.1.5 Phonon Deformation Potential. The phonon deformation potential is a relationship between strain in a material and the shift in its Raman spectrum. The results show a linear correlation between strain and shift in the Raman spectrum.

5.1.5.1 Four-Point Strain Fixture. Attempts were made to use a four-point strain fixture to determine the phonon deformation potential as described by Capt Starman [16]. However, little or no measurable changes in the Raman spectrum of the 6H-SiC samples were observed when using this technique. One possibility for the failure of this method may be due to the high Young's modulus of SiC in comparison to that of Si (see Table 2.2). Young's modulus relates how much a material will deform under a given stress. If the M-Bond 200 stretched before the SiC deformed no strain would be induced

on the crystal. In Starman and Lee *et al.* [1, 16] experiments, they used thin films (1-2 μm) which typically have a lower Young's modulus than bulk samples [41]. In comparison, the crystals that were tested in this experiment were 250- μm thick.

5.1.5.2 Vice. Measurement of the phonon deformation potential was also attempted by the vice technique described in Chapter IV. The 6H-SiC sample was experimentally determined to have a shift in the TO1, TO2 and LO peaks as a function of applied stress. As tensile stress was applied to the crystal, the peaks shifted to a lower wavenumber in a linear fashion as seen in Figures 5.7 and 5.8; the data points were indicated by blue circles. One important fact to note is that the resolution of the InVia Raman spectrometer is larger than the smallest measurement tracked when measuring the Raman shift in SiC as a function of stress. Because the Raman system is oversampled (refer to Section 4.4.2) and each spectral peak is statistically fit with a Voigt profile using Wire 2.0[®], the mean position of the peak is determined with resolution below the instrument resolution. It is the mean positions that are plotted in Figures 5.7 and 5.8(top). The data points were linearly fit using a least squares fit algorithm. The residuals chart (Figures 5.7 and 5.8 bottom) gives an indication of how closely the fit matched with the actual data points. From the fit to the data shown in Figures 5.7 and 5.8, the TO1 and TO2 mode frequencies are determined to be:

$$\begin{aligned}\omega_{TO2}(cm^{-1}) &= -3.02P + 788.4 \\ \omega_{TO1}(cm^{-1}) &= -1.62P + 766.6\end{aligned}\tag{5.3}$$

where P is a positive tensile pressure measured in GPa. The linearity of the TO2 mode frequency is close to same as the results of Liu *et al.* [28]. The slight differences in the two equations could be from different crystal faces, doping levels, crystal quality, experimental setup or curve fitting techniques.

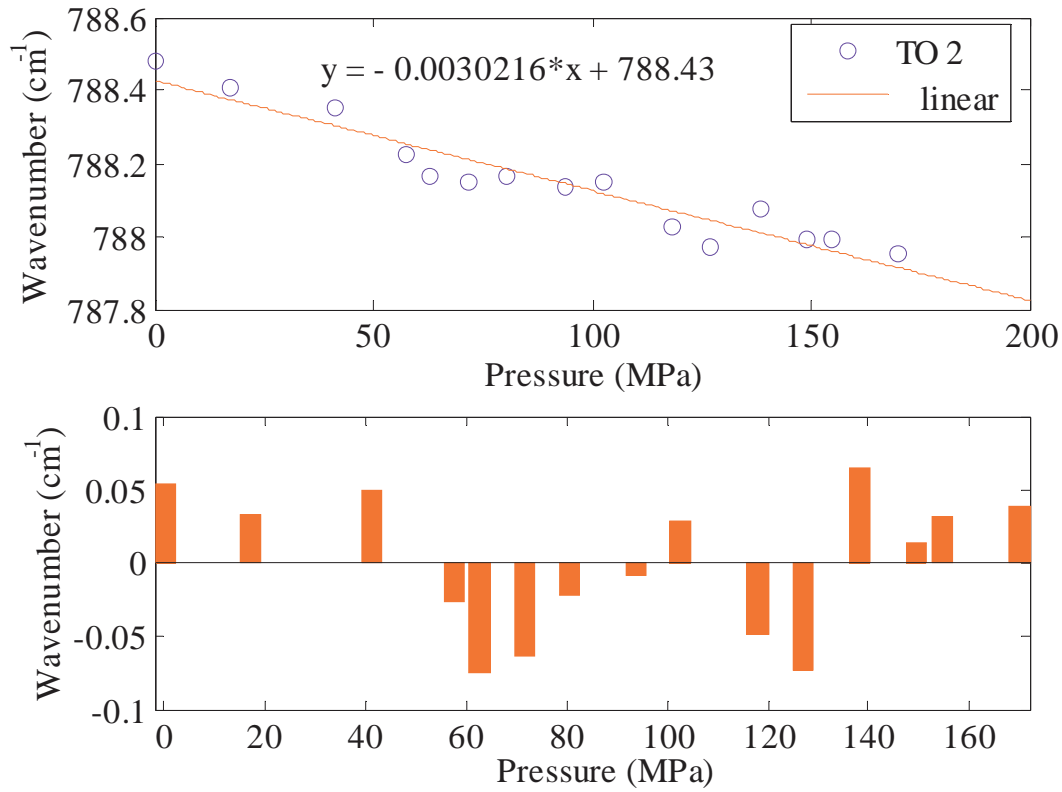


Figure 5.7 The top graph shows the line center of the TO2 peak as a function of uniaxial pressure applied normal to the c-axis of 6H-SiC. The bottom graph shows the residuals of the linear least squares fit to the measured data points.

Figure 5.8 shows the line centers of the TO1 peak as a function of applied stress, with a linear least squares fit and a plot of the corresponding residuals. By comparing the slope of the TO1 line in Figure 5.8 with the slope of TO2 line in the Figure 5.7, it becomes apparent that the TO2 line has a greater shift with respect to stress than the TO1 peak. The fact that the TO1 peak shifts less than the TO2 peak was further confirmed in line scans across the edge of the diaphragm of the NASA 550 pressure sensor, where the shift of the line center of the two peaks was tracked separately (see Figure 5.10). From these results, the TO2 peak is chosen to map areas of changes in the Raman shift due to residual stress.

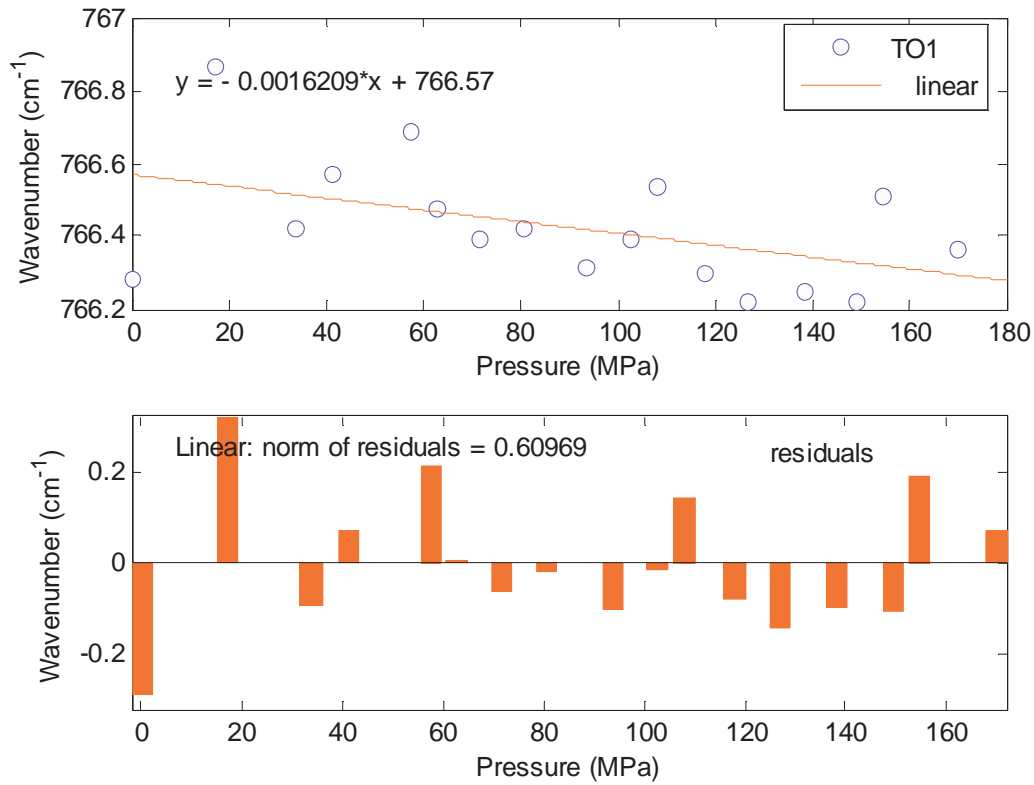


Figure 5.8 The top graph shows the line center of the TO1 peak as a function of uniaxial pressure applied normal to the c-axis of 6H-SiC. The bottom graph shows the residuals of the linear least squares fit to the measured data points.

5.1.5.3 Line Scans. Once the Raman spectra of 6H-SiC were determined for unstressed and stressed crystals, measurements were performed by line scans to collect the Raman spectra at each point on the sample in 5- μm steps using a computer controlled piezoelectric stage. Figure 5.9 (a) shows the location of one line scan across resistor #3. Figure 5.9 (b) shows where resistor #3 is located on the NASA 550 pressure sensor. In Figure 5.9 it can be seen that the scan crosses the edge of the diaphragm which is determined to be a location of residual stress from fabrication procedures.

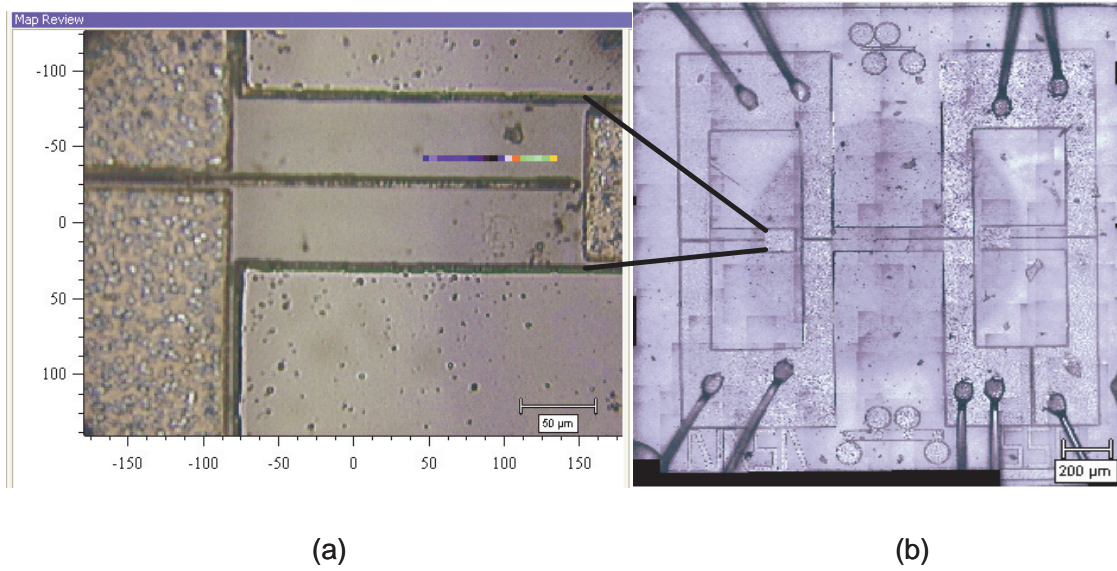


Figure 5.9 (a) Location of line scan on resistor #3. (b) Location of resistor #3 on NASA 550 pressure sensor.

Figure 5.10 was reproduced from the Raman data collected in the line scan depicted in Figure 5.9. At each spatial point, the Raman spectrum was curve fit using a Matlab program (in Appendix C), and the line centers of each Stokes line were determined in reference to the Rayleigh line. This was done to account for thermal drift of the excitation source during the collection time of an experiment. Figure 5.10 shows the TO1 and TO2 mode frequencies as a function of the spatial position of the scan. By comparing Figures 5.9 and 5.10 it can be observed that at an x-position of 80 μm , the scan begins to cross the edge of the diaphragm generating a shift in the positions of both the TO1 and TO2 mode frequencies. In the vice experiment, the change in TO1 mode frequency was not as great as the change TO2 mode frequency. In this separate line scan experiment the TO1 and TO2 mode frequencies changed at different rates from the strain confirming the fact that the TO2 mode is more sensitive to stress (see Figures 5.8 and 5.7).

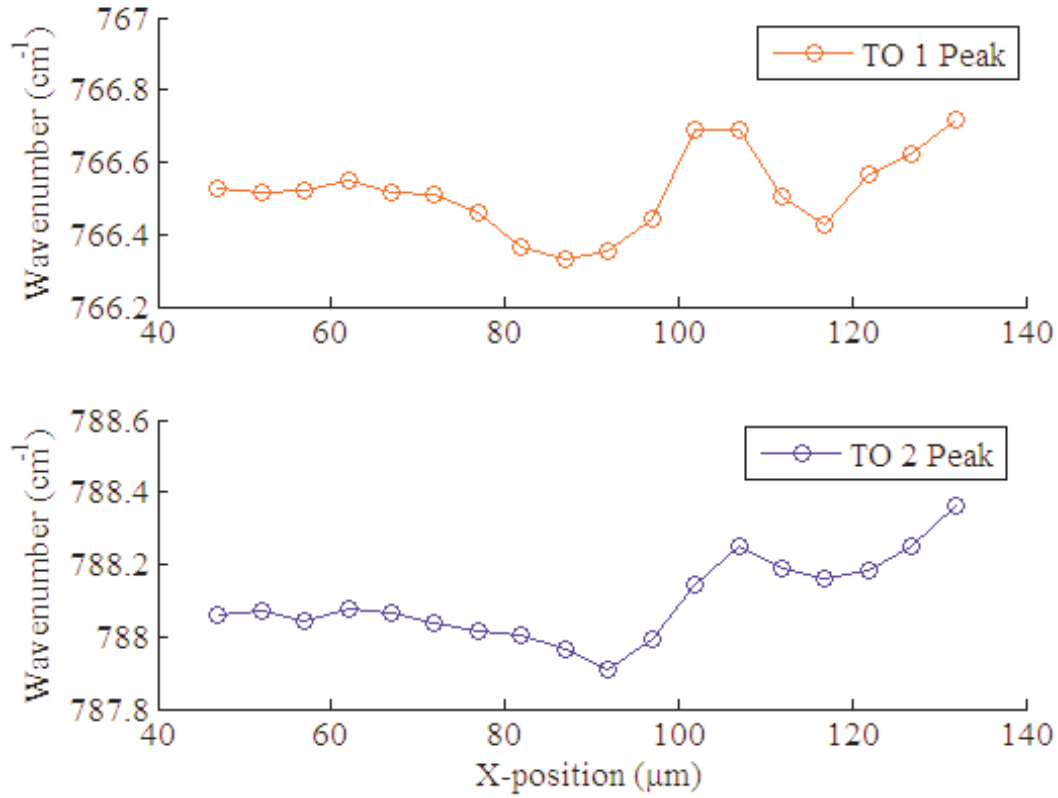


Figure 5.10 The line center of the TO 1 and TO 2 6H-SiC Raman peaks as a function of position.

In order to determine the amount of stress at each position, the linear relationships given in Equation (5.3) were used to map the data shown in Figure 5.10 in terms of residual stress shown in Figure 5.11. Because the fit to the phonon deformation potential data by both linear regressions had some variations, it was necessary to determine the estimator for the variance given by [42]

$$\hat{\sigma}^2 = \frac{SSE}{n - 2} \quad (5.4)$$

where SSE (*sum of the squares error*) is the sum of the squares of the residuals shown graphically on the bottom of Figures 5.8 and 5.7 and n is the number of data points. The standard deviation (STD) was computed as the square root of the variance. The STD was

scaled using the Equation (5.3) and plotted as error bars at each data point seen in Figure 5.11. By inspection of the graphs in Figure 5.11, it is determined the TO2 mode frequency is more accurate of an indicator of the true stress at each point in the line scan. Therefore, any mapping of stresses will be done with the TO2 peak.

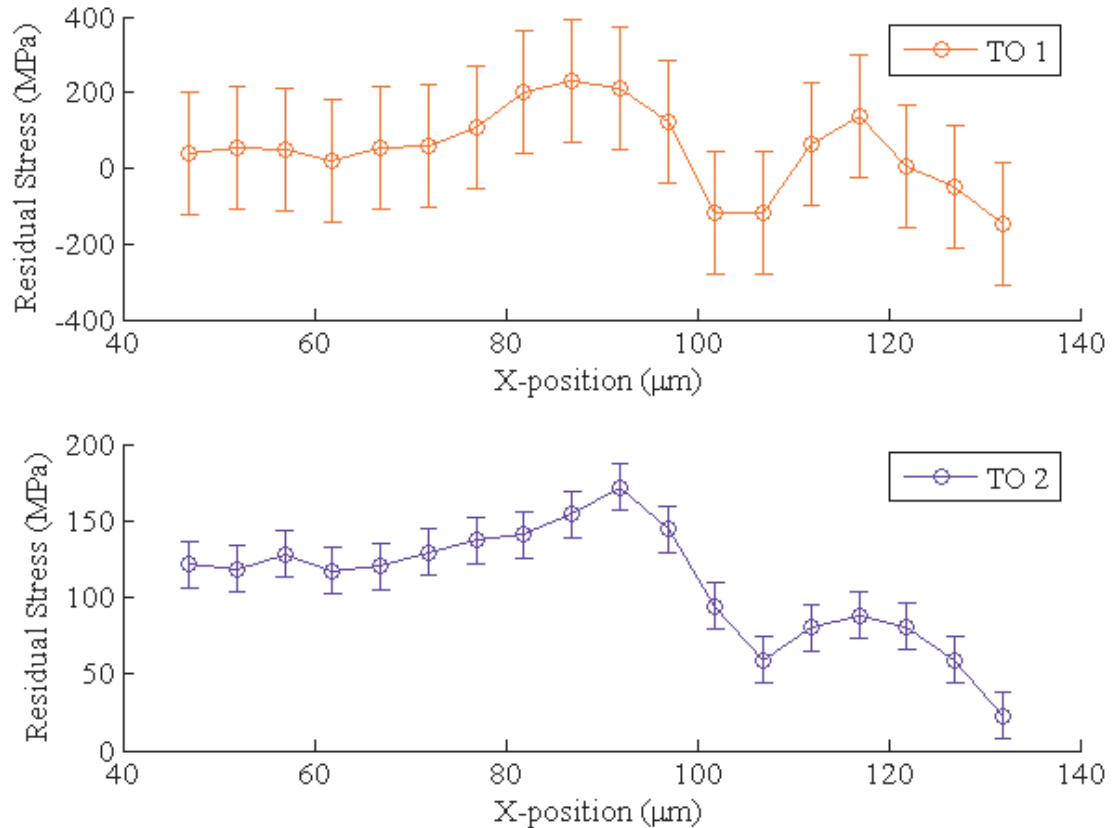


Figure 5.11 The estimated amount of residual stress as a function of position of the line scan shown in Figure 5.9. The estimates were found using phonon deformation potentials for the TO 1 and TO 2 peaks and mapping them to the results shown in Figure 5.10.

The TO1 mode frequency had less reliable results for the tracking of residual stress than the TO2 mode frequency. The main reason is that the baseline shown in Figure 5.12 was raised due to background noise from a foam layer behind the SiC sample (see Figure 4.8). The fact that the baseline was raised added some limitations into the curve fitting

performed by the Wire 2.0[®] software. Fitting the smaller TO1 peak showed slightly more ambiguity in the line center location than the more intense TO2 peak.

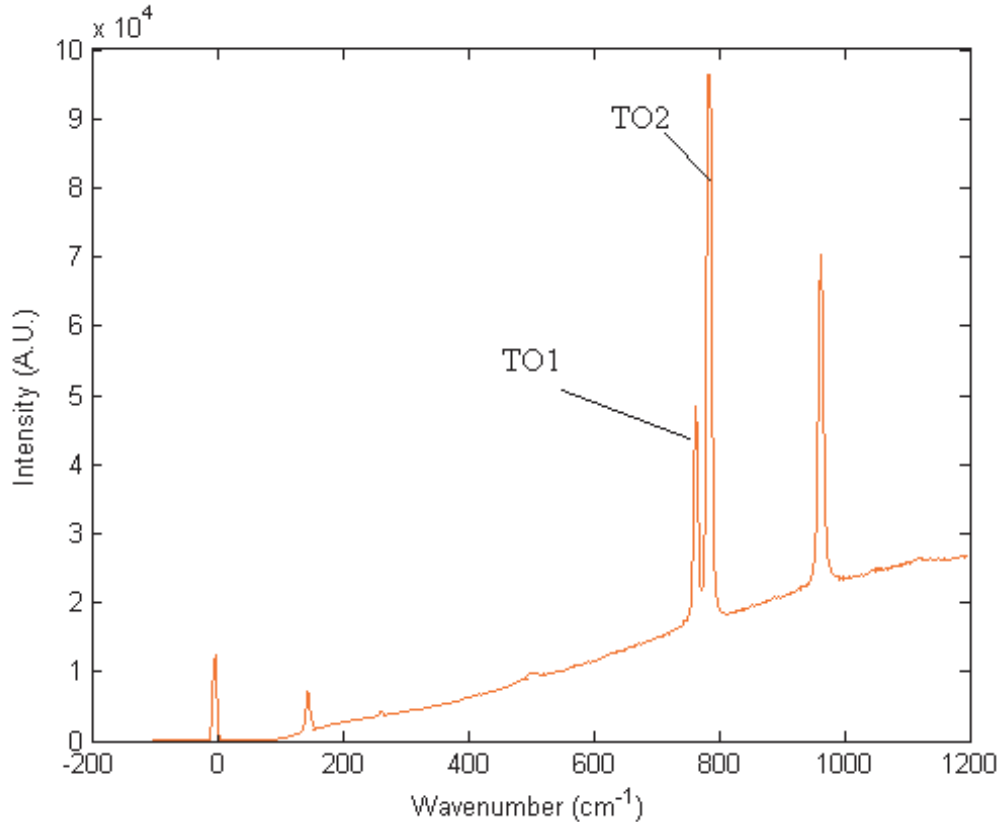


Figure 5.12 Typical Raman spectrum of the 6H-SiC as measured during the determination of the phonon deformation potential. The raised baseline is due to background noise from a piece of foam the sample was placed on.

5.1.6 Raster Maps of Raman Shift. In order to determine if there is residual stress along the entire edge of the diaphragm of the 550 NASA pressure sensor (see Figure 5.13 (b)) as previously indicated by the line scan across resistor #3, a raster scan was performed on an edge of the diaphragm, which can be seen as a change in shade from light to dark grey in Figure 5.13 (a). Using the piezoelectric micropositioning stage, the Raman spectrum at each point was recorded stepping across the surface in 5- μm increments. The Raman spectra were curve fit at each point using the Raman analysis program in Appendix C to determine the line center of each Stokes peak in relation to the Rayleigh peak. The

TO2 mode frequency was recorded at each spatial position and then converted to stress units by Equation (5.3). A map of residual stress along the edge of the diaphragm was then plotted as a function of spatial position as depicted in Figure 5.13 (c).

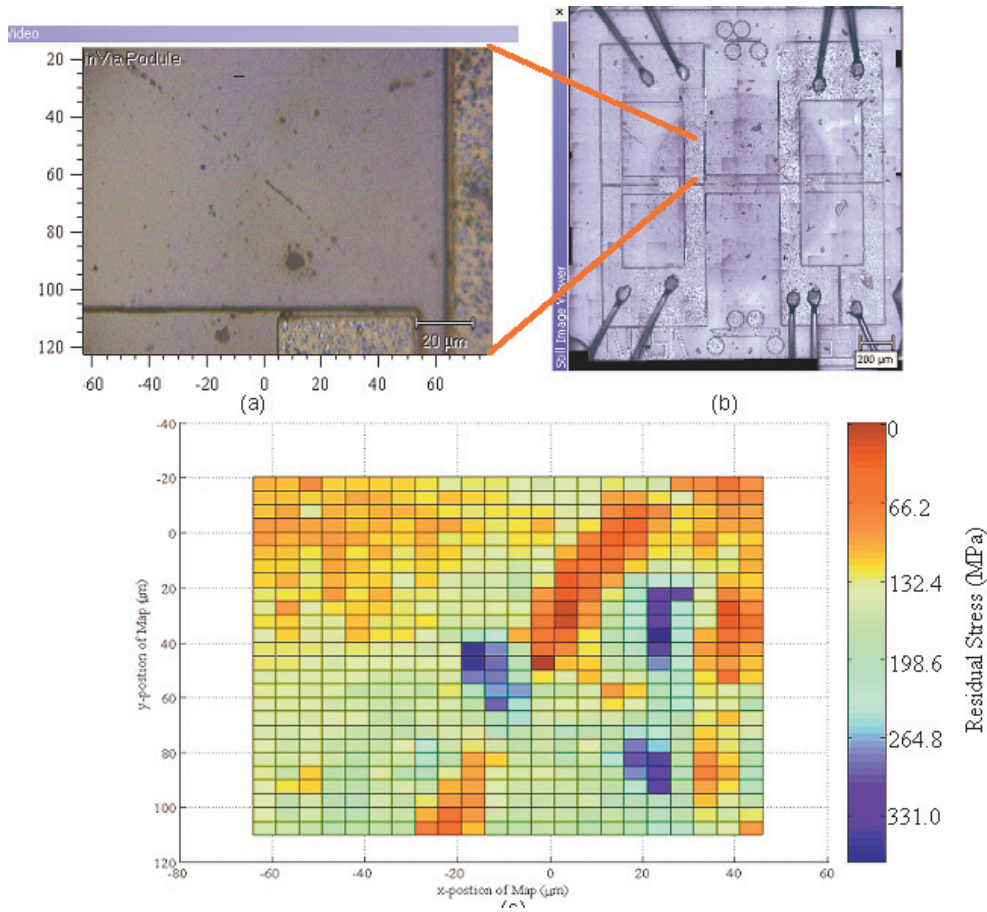


Figure 5.13 (a) Micrograph of diaphragm edge through a 20X objective with a coordinate system that matches the raster map location in (c). (b) Micrograph of the NASA 550 pressure sensor depicting the location of the edge of the diaphragm. (c) The residual stress measured using of a raster scan across the edge of the diaphragm.

5.1.6.1 Raster Scans Across Piezoresistors. From the large variance in resistance of the piezoresistors, the question arose whether residual stresses are playing a part in those measurements. The residual stresses in resistors #2 and #4 were measured, and are shown in Figures 5.14 and 5.15. The scan was performed on the sample (Figure

5.14 (a)) where the red line is pointing to the optical micrograph of the NASA 550 pressure sensor in Figure 5.14 (b). The scan revealed little residual stress in resistor #2.

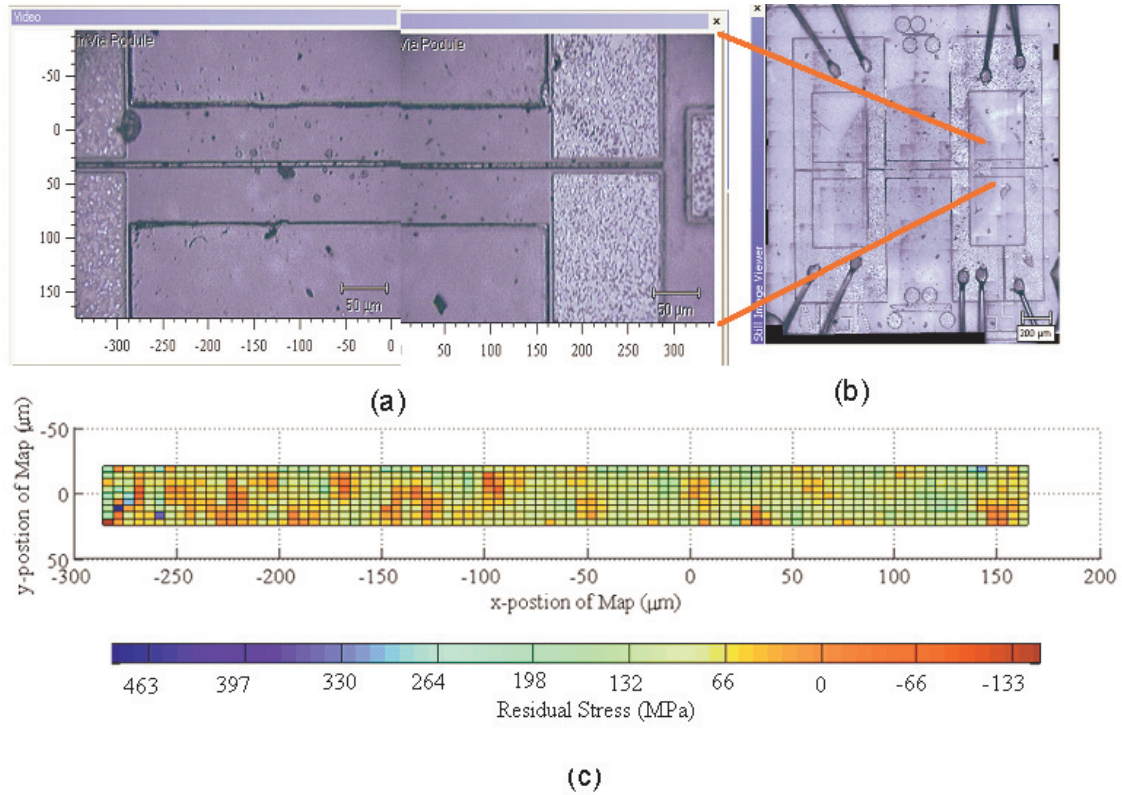


Figure 5.14 (a) Micrograph of resistors #2 and #4 through a 20X objective with a coordinate system that matches the raster map location in (c). (b) Micrograph of the NASA 550 pressure sensor depicting the location of resistors #2 and #4 on the device. (c) The residual stress measured using of a raster scan across resistor #2.

The Raman map of resistor #4 depicted in Figure 5.15 (c) was taken from the location shown in Figure 5.15 (a) that is located where the red line is pointing to the optical micrograph of the NASA 550 pressure sensor in Figure 5.15 (b). From this raster scan, more residual stress was detected, particularly in the x-postion of 200 μm .

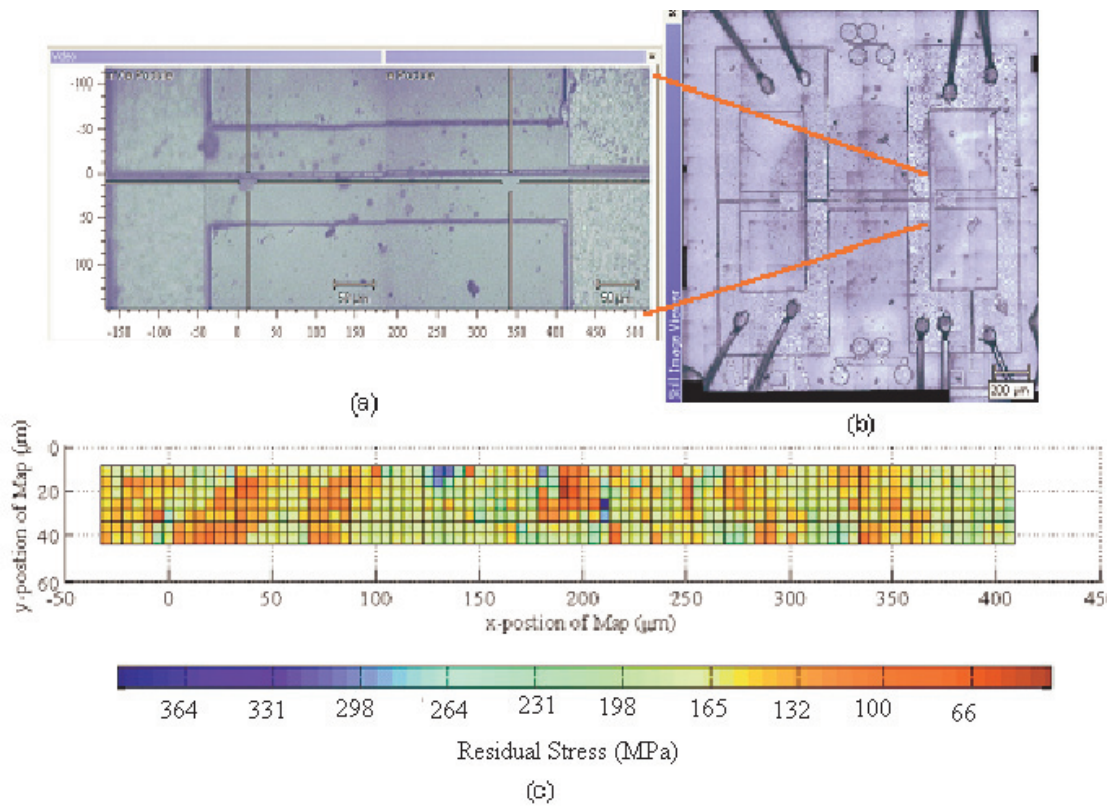


Figure 5.15 (a) Micrograph of resistors #2 and #4 through a 20X objective with a coordinate system that matches the raster map location in (c). (b) Micrograph of the NASA 550 pressure sensor depicting the location of resistors #2 and #4 on the device. (c) The results of a raster scan across resistor #4 showing the amounts of residual stress in the resistor.

A raster scan also identified residual stress in the region around the x-position of 200 μm shown in Figure 5.16 (a). This region is shown as a red box and is magnified in Figure 5.16 (b) with a green oval around the area in which the stress was detected. Due to the transparency of the 6H-SiC from which the piezoresistor was made, the focal plane of the microscope was able to be moved below the piezoresistor top, and revealed a defect in the structure below. The defect can be seen as a change in shade circled in Figure 5.16 (c).

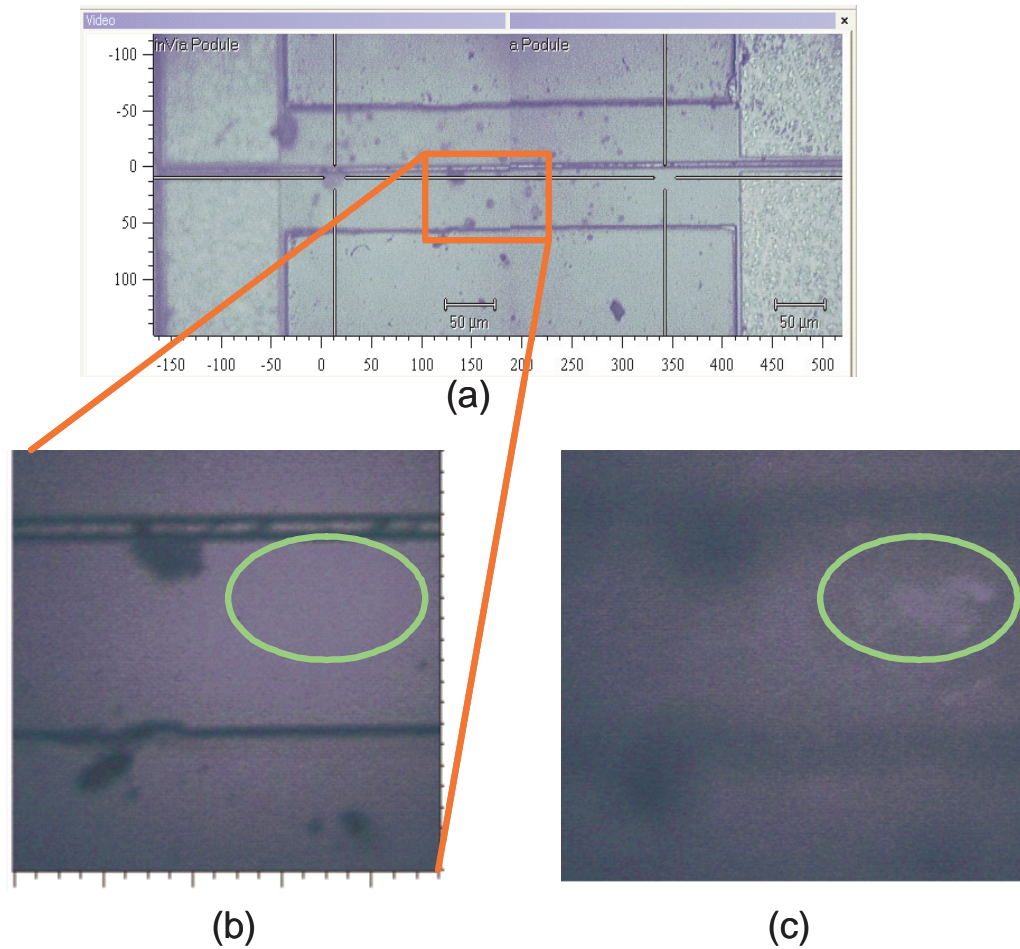


Figure 5.16 (a) and (b) Zoom in on the defect location on resistor #4 identified by Raman mapping (c) Observation of the identified defect optically by changing the depth of focus on the microscope and recording the image.

The technique of using Raman spectroscopy to detect residual stress and defects in 6H-SiC MEMS has been proved to be effective. The phonon deformation potential for the Cree Inc. 6H-SiC wafers that the NASA 550 MEMS structures were fabricated from was demonstrated. Furthermore, the deformation potential are comparable to independent measurements made by Lui *et al.* [28] on a 6H-SiC crystal. The mapping of the residual stress was made possible by the InVia Raman spectrometer with an incorporated piezoelectric stage. The TO2 mode frequency was determined to be the most statistically reliable mode track for mapping the residual stress. With the capability to detect and quan-

tify amounts of residual stress, the next step will be to determine a method of relieving the stress from the fabrication processes.

5.2 Thin Film poly-SiC

Due to the nature of poly-SiC thin films (1.5 to 5 μm), the Raman spectra of the films have proven to be more difficult to characterize than the Raman spectrum from the single-crystal 6H-SiC MEMS devices provided by NASA. Attempts by Capt Stan Ness [39] to identify residual stress in thin film poly-SiC by Raman spectroscopy using a 514-nm excitation source on 1.5 to 2- μm films showed little success. In the experiments outlined in this thesis, a 325-nm excitation source was used and 1.5–5- μm thick poly-SiC films were investigated. The UV photons are well above the bandgap of SiC and are proven to be highly absorptive (refer to in Figure A.1). This provides a resonant Raman effect, reduces the amount of photons reaching the Si substrate, and therefore increases the signal-to-noise ratio (SNR).

Several factors could influence the Raman spectra of the poly-SiC films including possible stacking faults, grain boundaries, impurities and other polytypes found in the poly-SiC. In addition, fluorescence of both the thin film of SiC and the Si substrate can create background noise in the Raman spectrum and decrease the SNR.

5.2.1 325-nm versus 514-nm Excitation–Resonant Raman, Resolution and Luminescence. Raman spectroscopy of the same 1.5- μm poly-SiC thin films on (100) Si substrate that Capt Ness [39] investigated with the 514-nm wavelength laser excitation source was repeated. A cross-section of the sample is shown in Figure 3.4. The 514-nm laser penetrates through the poly-SiC thin film with very little absorption or Raman activity as shown in Figure 3.6, and much of the incident light is Raman scattered by the Si substrate and shows up as the sharp peak at 521-cm^{-1} in Figure 5.17. Some of the incident light is Raman scattered by the poly-SiC and shows up as broadened TO and LO peaks.

For the same 1.5- μm poly-SiC thin films on (100) Si substrate, the 325-nm laser excitation source produced much narrower TO and LO Raman peaks. The Raman spectrum recorded from the poly-SiC is shown in red in Figure 5.17. The characteristic modes of 3C-SiC, TO at 791-cm^{-1} and the LO at 958-cm^{-1} were apparent. The Si mode was also significantly diminished. The improved results using the UV excitation source are attributed to two effects. One effect is the increased absorption of the poly-SiC film preventing much of the incident laser light from reaching the substrate, and therefore reducing the amount of Raman scattering from the substrate. The other effect is a resonant Raman effect which increases the amplitude and sharpens TO and LO intensities as explained in the Section 2.1 for this thesis and further detailed in *Introduction to Raman Spectroscopy*, by Ferraro *et al.* [17].

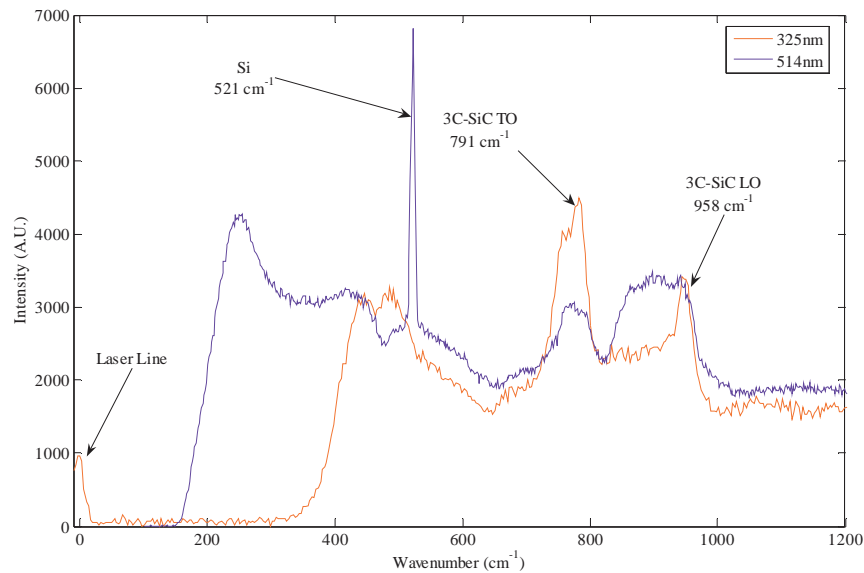


Figure 5.17 The blue spectral lines are from the Raman spectrum of a 1.5- μm poly-SiC layer on a (100) Si substrate measured using a 514-nm excitation source. The red spectral lines are of the same 1.5- μm poly-SiC film with a 325-nm excitation source.

5.2.2 UV Raman Spectroscopy: Si versus SiC on Si. To further substantiate that the peak around 500 cm^{-1} was due to the Si substrate, the Raman spectrum of (100) Si

was measured using the 325-nm excitation source and compared to the spectrum of the poly-Si thin film discussed in the previous section. Both are plotted together in Figure 5.18. Points of interest include the correlation of the two peaks around 500 cm^{-1} , and the raised baseline of both samples that appears to be caused mainly by the Si substrate. The excitation source was a 325-nm wavelength laser, which has a photon energy of 3.81-eV that exceeds both the Si and 3C-SiC bandgap energies of 1.12-eV [20] and 2.36-eV [33], respectively. Attempts were made to subtract the Si spectrum from the SiC-on-Si spectrum, but the noise level could not be reduced.

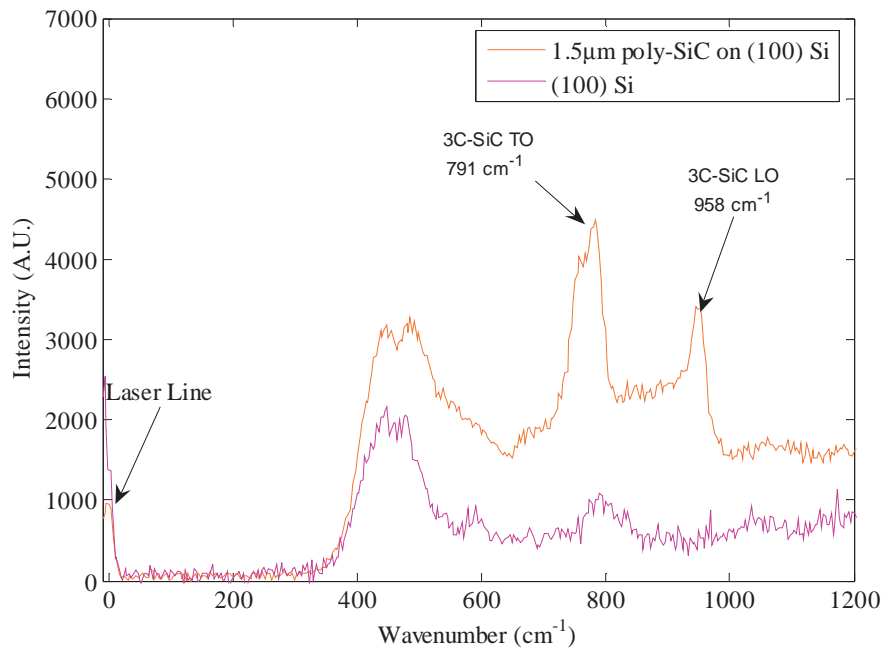


Figure 5.18 The Raman spectrum of a 1.5- μm poly-SiC on a Si (100) substrate is compared with the Raman spectrum of Si (100) both of which were excited by a 325-nm excitation source.

5.2.3 Film Thickness – Absorption. In order to investigate whether the thickness of the poly-SiC film enhanced the Raman spectrum, the Raman spectrum of 1.5- μm and 5.5- μm -thick poly-SiC were compared (samples shown in Figures 3.4 and 3.5 were analyzed). The reason the thicker film enhances the Raman spectrum was that there would be more of a resonant Raman effect and a reduction in the amount of photons that reach

the Raman-active Si substrate. The Raman spectrum of the 5.5- μm poly-SiC was overlaid with the 1.5- μm spectrum in Figure 5.19. Note that the TO and LO spectral lines sharpen and intensify dramatically in the 5.5- μm thin film. However, the Si line also increased, raising the question of whether the sample had a higher quality or the thickness of the film increased the SNR. To understand if thickness is critical in increasing the SNR, more samples with varying thickness would need to be tested. Increased SNR should make it possible to track peaks with respect to an applied strain as demonstrated by Lee *et al.* [1].

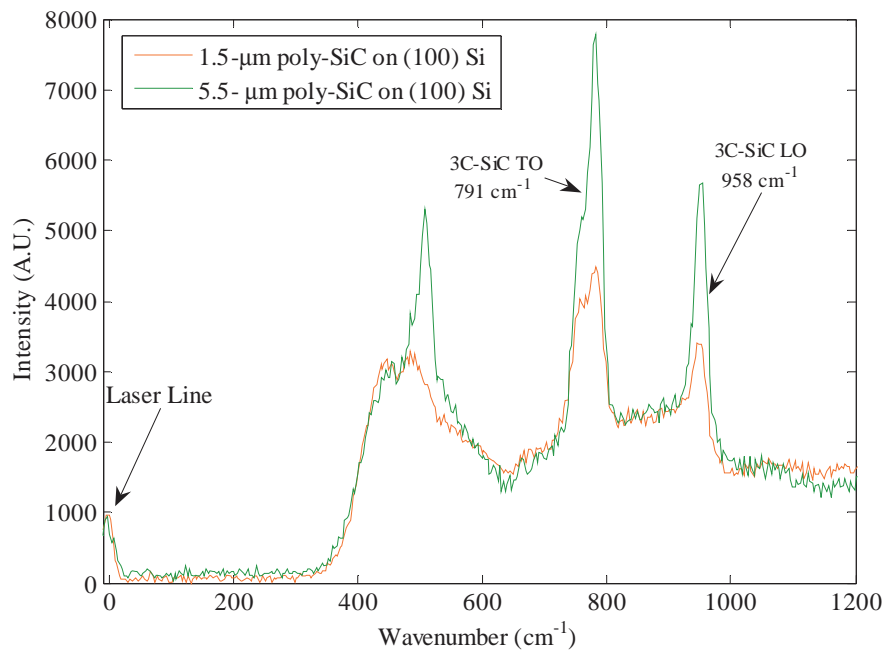


Figure 5.19 Raman spectrum of poly-SiC films of thickness 1.5 μm and 5.5 μm using a 325-nm excitation source.

5.2.4 Substrate Raman Noise. After evaluating the Raman spectrum of the 5.5- μm poly-SiC shown in Figure 5.19, FLX Micro Inc. provided the sample shown in Figure 5.20 (a). In addition, the Renishaw applications and support engineer for Raman products re-calibrated the inVia Raman spectrometer increasing the SNR of every spectrum taken. A 5.5- μm poly-SiC film was grown on a (100) Si substrate (Region 2 in Figure 5.20 (a)). Windows of the Si substrate were anisotropically back-etched producing suspended membranes of poly-SiC (Region 1). Also, portions of the poly-SiC were delaminated,

revealing the Si substrate (Region 3). The delaminated portions were used later in a strain experiment. Region 1 was expected to have no Si underneath the membrane, however, as seen in Figure 5.20 (b), the Raman spectrum of Region 1 and Region 2 were almost identical. It is possible that the spectrum around 520 cm^{-1} is due to fluorescence from SiC, but the Raman spectrum taken in region 3 of the Si substrate matches very closely with these spectral peaks. Attempts were made to do x-ray diffraction on the delaminated films to see if there was any Si present on the surface of the delaminated films. Inconclusive results were obtained and should be further investigated.

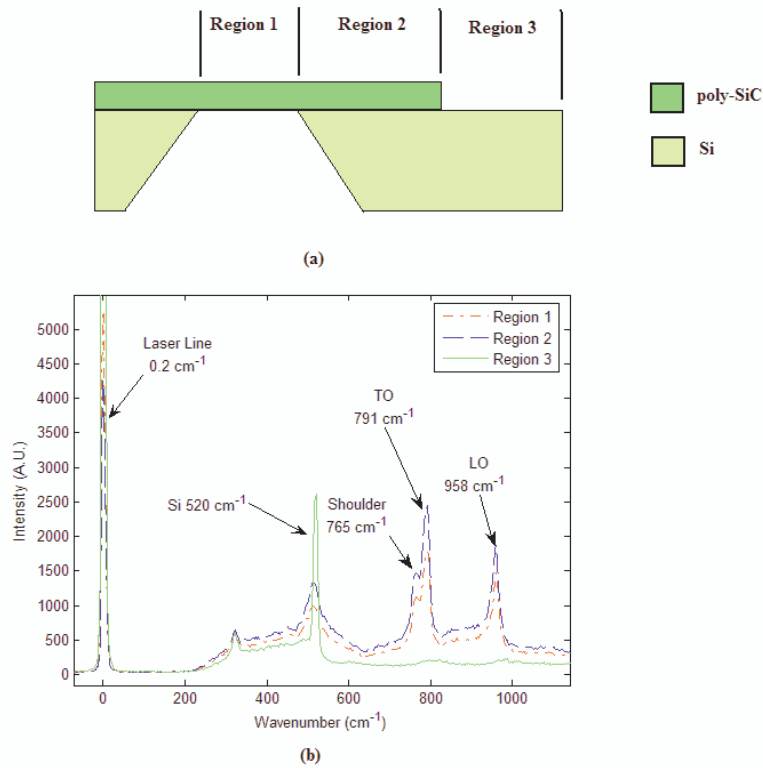


Figure 5.20 (a) A cross-section of a 5.5- μm poly-SiC thin film grown on a (100) Si substrate. Pyramidal pits of the Si substrate were anisotropically back-etched creating suspended membranes of the poly-SiC (Region 1). Portions of the poly-SiC delaminated revealing the Si substrate (Region 3). (b) The Raman spectrum of the three regions shown in the cross-section (a) using a 325-nm excitation source.

5.2.5 Stacking Faults in poly-SiC. FLX Micro Inc. states that the poly-SiC films are primarily 3C-SiC, however, a comparison of the 3C-SiC values with those measured and recorded of the poly-SiC in Figure 5.20 (b) exhibited some mismatches. The FTO mode frequency of 791 cm^{-1} is red shifted 5 cm^{-1} from crystalline 3C-SiC FTO mode frequency and the FLO mode frequency of 958 cm^{-1} is red shifted 14 cm^{-1} (see Figure 2.16). Even though the 325-nm source greatly improved the Raman spectrum, the spectral lines were still broad when compared to crystalline 3C-SiC, and therefore the peak appears as a shoulder on the left half of the FTO peak.

According to Rohmfeld *et al.* [29], the shift in the Raman spectrum, the broadened line widths of the FTO and FLO peaks, and the shoulder to the left of the FTO peak are all a result of stacking faults in poly-SiC thin films. Rohmfeld *et al.* shows how the line width narrows, the shoulder is suppressed and the line center shifts to the crystalline 3C-SiC TO line center when the sample is laser annealed. A computer generated model is used to support the effects of stacking faults. Figure 2.19 shows the TO peak in 3C poly-SiC as deposited, and after laser annealing at 1700 K.

5.2.6 Delaminated poly-SiC. The Raman spectrum of the poly-SiC that delaminated from the (100) Si substrate was compared with the spectrum of the same film on the (100) Si substrate. Note in Figure 5.21 that there was little if any difference between the two spectra. The spectrum of the delaminated film indicates a Si spectral line, which was unexpected and should be investigated further.

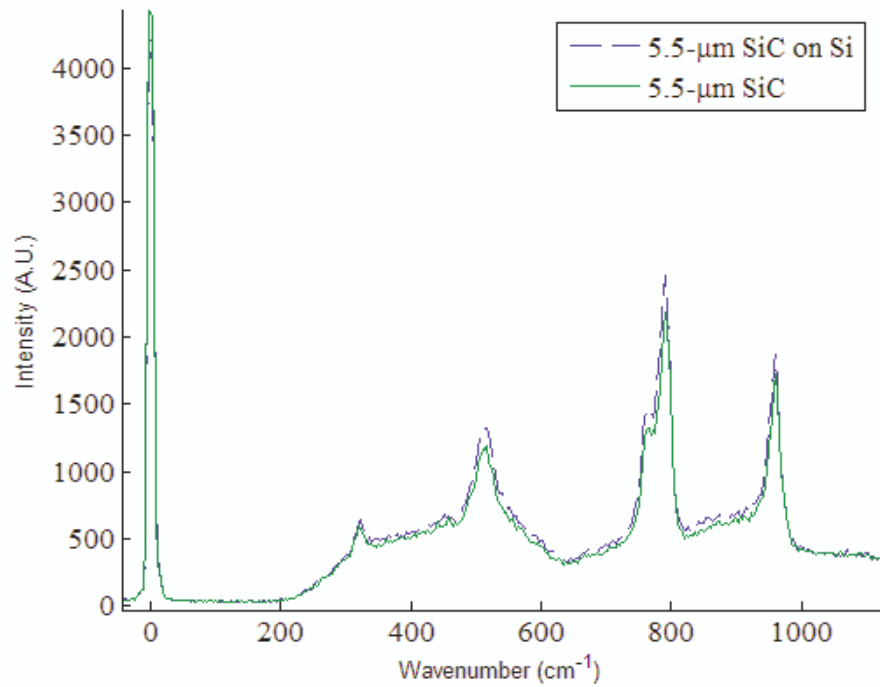


Figure 5.21 The spectrum of 5.5- μm SiC on Si and SiC on Plexiglas.

The poly-SiC film was bonded, along with a strain gauge, to a piece of Plexiglas glass using M-bond 200 adhesive. The assembly was then placed on the 4-point strain fixture, and a uniform compressive stress was applied. The stress was measured by a strain indicator and recorder. The TO, LO and laser line peaks were curve fit using Wire 2.0[®], and the center of the curves were tracked as a function of compressive stress. Unexpectedly, the peak centers did not shift as a function of stress (see Figure 5.22), indicating that either no stress was felt by the film or the phonon modes are not sufficiently sensitive to stress in this poly-SiC to monitor. More experiments should be made to identify the phonon deformation potentials of the poly-SiC.

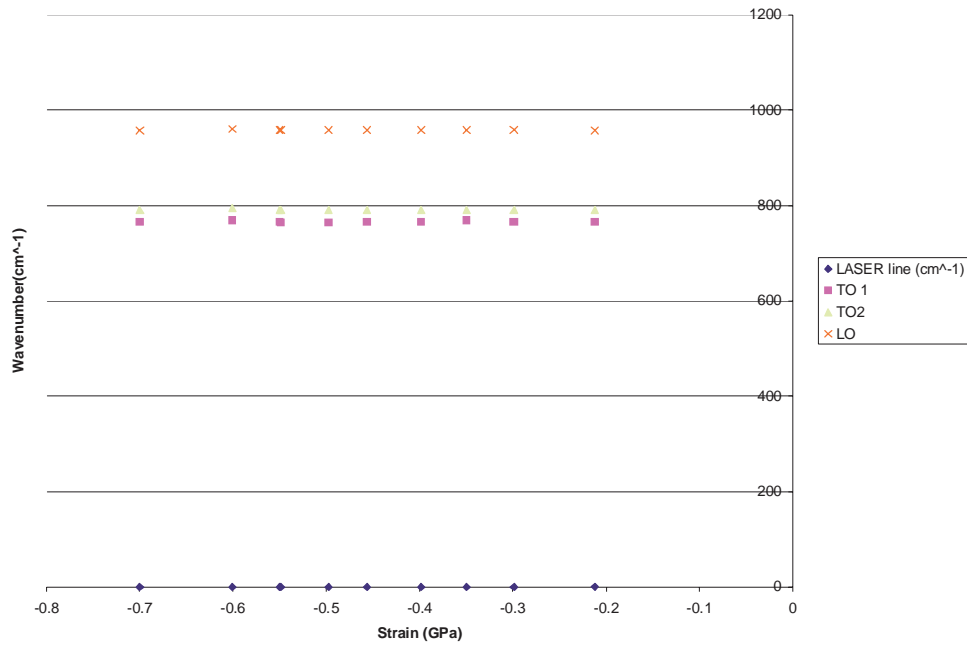


Figure 5.22 The shift of peaks of 5.5- μm poly-SiC as a function of compressive stress

5.3 Chapter Summary

The results of the experiments performed in this research were presented in this chapter showing that the single-crystal 6H-SiC MEMS can be evaluated for defects and stress using Raman spectroscopy. The poly-SiC samples may also be evaluated using similar methods, however more work is needed to develop reliable techniques. The next chapter will presents some conclusions and recommendations as a result of this work.

VI. Conclusions and Recommendations

The objective of this research, to determine a NDE method of identifying residual stress, stress gradients and defects in SiC MEMS, was met. First the phonon deformation potentials, that show a correlation between variations the Raman spectrum of SiC and stress on the crystal structure, were determined. Then a NDE technique was developed that employs the spacial mapping of the Raman spectrum across SiC MEMS allowing for visual identification of areas containing residual stress and defects.

6.1 Conclusions

The evolution of the stress states from raw materials to fabrication of SiC MEMS is very important (i.e., process-induced changes in the microstructure). Baseline measurements allow the understanding of the operation-based evolution of the microstructure due to shock, high temperature, high voltage, ect. μ -Raman spectroscopy is becoming important due to the repeated demonstrations of the ability to measure microstresses in SiC materials. The experiments performed sought to address the underlying problem of defects and microstress associated with SiC MEMS.

This research contributed to the state of the art in the detection and measurement of residual stress in a variety of SiC-based MEMS structures. Raman spectroscopy provides the means to obtain microstructural information. The spectroscopic techniques were adapted and applied to different crystal structures, both single crystalline and polycrystalline, and two different polytypes, 6H and 3C.

To the best of our knowledge, this work is the first study of residual stress corresponding with defects in single crystal SiC MEMS devices. The work is also one of the first studies on stress detection in polycrystalline SiC [20]. The results presented here are important in the understanding of SiC materials. The measurement of deformation potential show linear results that correlate stress to Raman shift. Another important capability of Raman spectroscopy is the mapping of residual stress states in MEMS devices. Defects

and stress networks within the samples were identified by Raman maps. Stacking-fault observations in polycrystalline Raman spectra were evidenced by broadening of the Stokes peaks.

The pioneering work in SiC represents a significant improvement in understanding this development of residual stress in a variety of crystal structures. Raman spectroscopy provides a non-destructive evaluation capability to optimize process output in device fabrication by identifying defects in raw material.

6.2 Recommendations for Future Work

In the work completed for this thesis, Raman spectroscopy has been determined to be an excellent method of locating residual stress and defects in SiC MEMS. The magnitude of residual stress is further quantified by the determination of the phonon deformation potential for 6H-SiC MEMS. To better quantify the relationship between stress and Raman shift for 6H-SiC, a diamond anvil cell setup similar to Liu *et al.* [28] should be used to compare the phonon deformation potential of 3.51° and 0.49° off axis 6H-SiC. With the capability to detect and quantify amounts of residual stress in SiC MEMS, the next step will be to determine a method of relieving the stress induced in the fabrication processes. Some ideas on how to relieve the residual stress in the MEMS structures are with ion implantation, high temperature annealing or by nuclear radiation [43].

Efforts in this research have also indicated that MEMS fabricated from thin-film polycrystalline 3C-SiC on (100) Si substrates can be evaluated for residual stress using UV resonant μ -Raman techniques. Investigation should include the recording of the Raman spectrum of 10- μ m thick poly-SiC film on (100) Si and comparing those results to the Raman spectra of the 5.5- μ m and 1.5- μ m films to understand if thickness is critical in increasing the SNR. The next step in the research into thin film SiC should follow the outline of Capt. Starman's method of characterization of residual stress in thin-film MEMS (see Section 2.3). The phonon deformation potential for 3C-SiC determined by Lee *et al.* [1] should be verified. Some suggested methods are (1) an air pressure device

provided by FLX Micro Inc., (2) a 4-point bending fixture again (see [1]), (3) a vice to induce stress as was used for the 6H-SiC or (4) the use of a diamond anvil cell. Once this is complete, fix-fixed beams and cantilevers could be fabricated out of poly-SiC and residual stress measured before and after release. Then, attempts to relieve stress could be made using some of the techniques listed in the previous paragraph.

Another area of research interest is the identification of the cause of the strong Si Raman mode detected in the delaminated thin films of poly-SiC (see Section 5.2.6). Attempts were made to do x-ray diffraction on the delaminated films to see if there was any Si present on the surface of the film. Inconclusive results were obtained and should be further investigated.

Another interesting area of research related to this work is the investigation of MEMS made from other wide band gap semiconductor materials.

Appendix A. Properties of SiC

The Electron Hall Mobility shown in Figure A.1 is used in the calculation of the resistivity of the piezoresistive elements #2 and #4 on the NASA 550 sample (see Section 3.1.2).

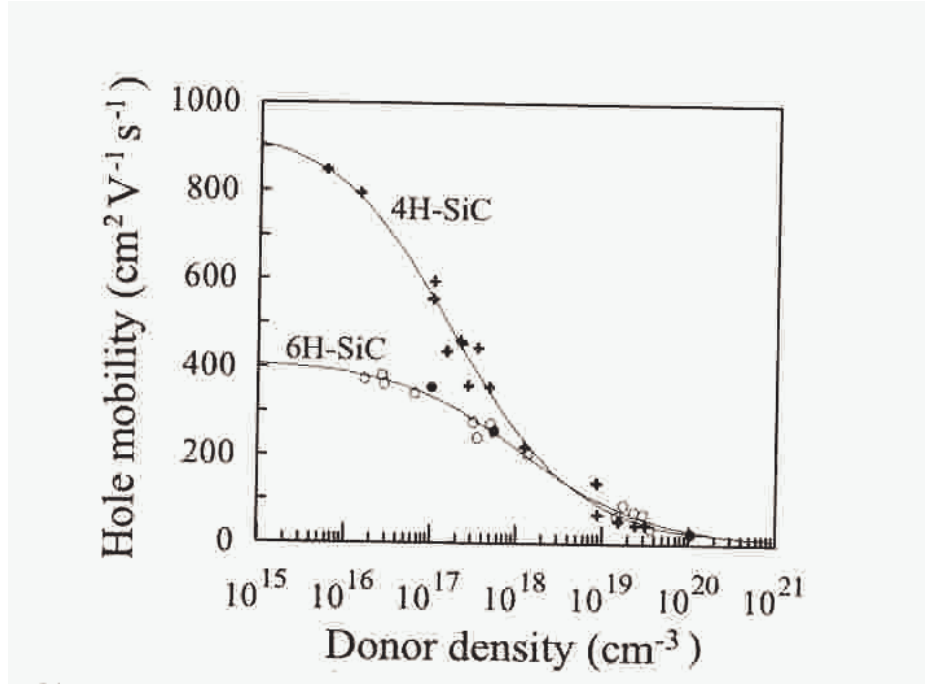


Figure A.1 Electron Hall mobility as a function of donor density [33]. Used to determine resistivity of 6H-SiC piezoresistors.

The absorption coefficients as a function of photon energy shown in Figures A.2 and A.3 were used in Section 3.3.3 to determine the percent of Transmission of light in 6H-SiC as a function of material thickness.

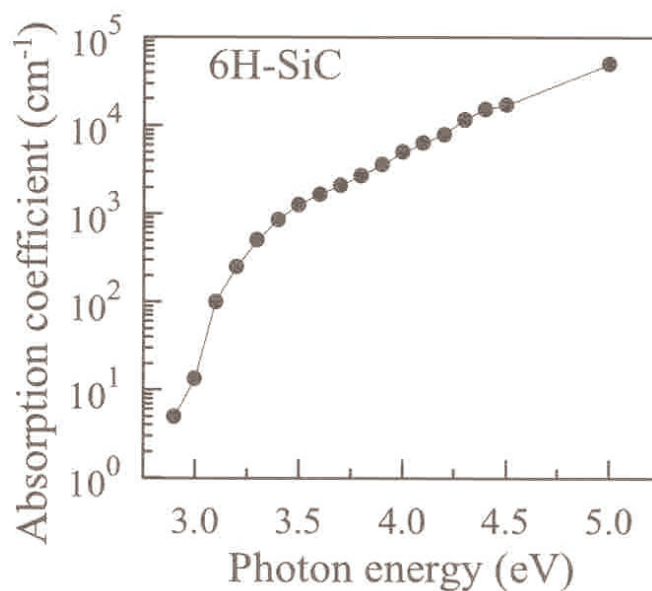


Figure A.2 Absorption coefficient of 6H-SiC as a function of photon energy [44]. Used to determine transmission length of 325-nm photons in crystalline 6H-SiC MEMS.

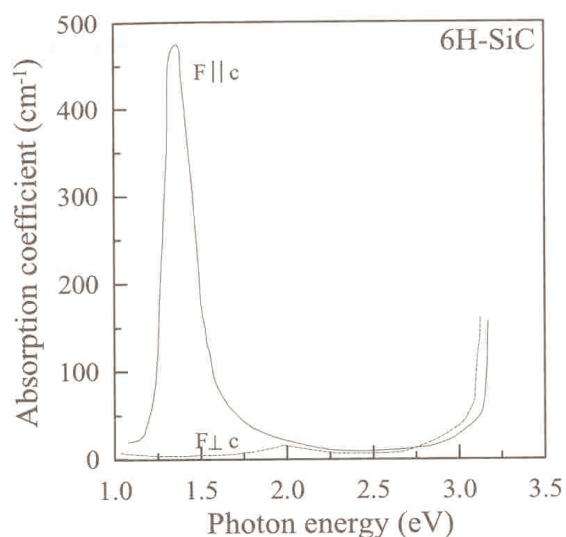


Figure A.3 Absorption coefficient of 6H-SiC as a function of photon energy [45]. Used to determine transmission length of 514-nm photons in crystalline 6H-SiC MEMS.

The absorption coefficients as a function of photon energy shown in Figure A.4 and Table A.1 were used in Section 3.3.3 to determine the percent of Transmission of light in 3C-SiC as a function of material thickness.

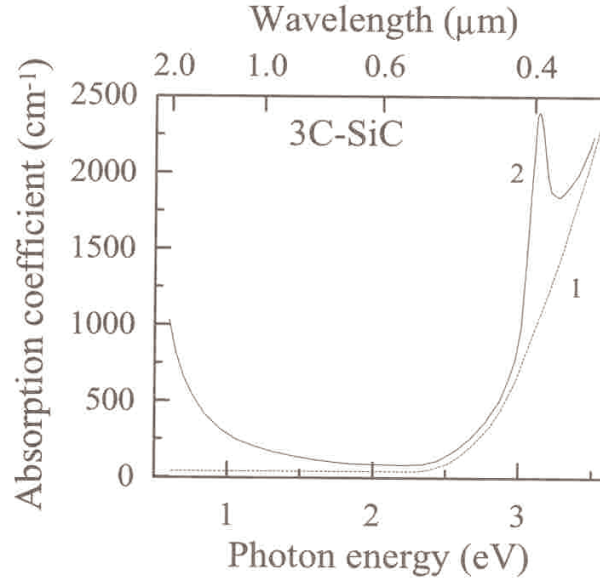


Figure A.4 "The absorption of 3C-SiC (1) and (2) at 300K. 3C-SiC (1) is relatively pure; crystal (2) is strongly n-type (perhaps $10^{19}/cm^3$ donors)" [46].

Table A.1 Absorption coefficients and depth penetration for 3C-SiC [4]

Wavelength(Å)	Laser	3C-SiC			
		300K		2K	
		$\alpha(cm^{-1})$	$\alpha^{-1}(\mu m)$	$\alpha(cm^{-1})$	$\alpha^{-1}(\mu m)$
3250	He-Cd	3660	2.7	3480	2.9
3336	Ar ⁺ ion	3190	3.1	3030	3.3
3371	N ₂ gas	2970	3.4	2860	3.5
3511	Ar ion	2260	3.4	2860	3.5
3540	He-Cd	2260	4.4	2160	4.6
3550	3xQ/Nd:YAG	2120	4.7	2030	4.9
3564	Kr ⁺	2070	4.8	1980	5.1

The band diagram of 3C-SiC in Figure A.5 is referred to in Section 3.3.3 to illustrate the absorption characteristics of 3C -SiC.

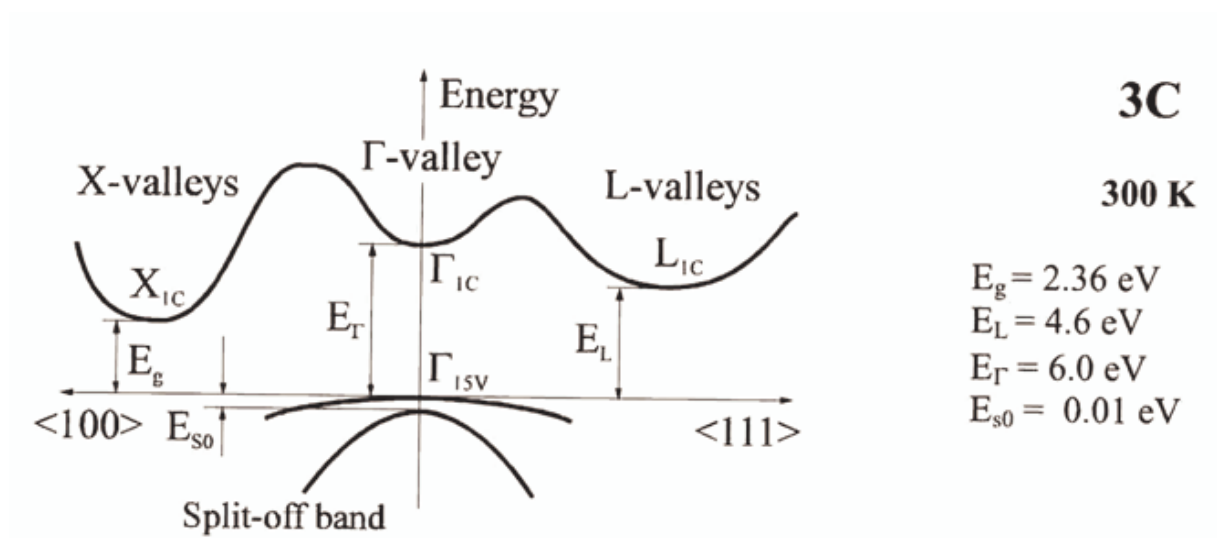


Figure A.5 Band Structure of 3C-SiC. Important minima of the conduction band and maxima of the valence band [47].

Appendix B. Equipment

A diagram of the four-point strain fixture test as a method of inducing stress on the SiC samples is shown in Figure B.1.

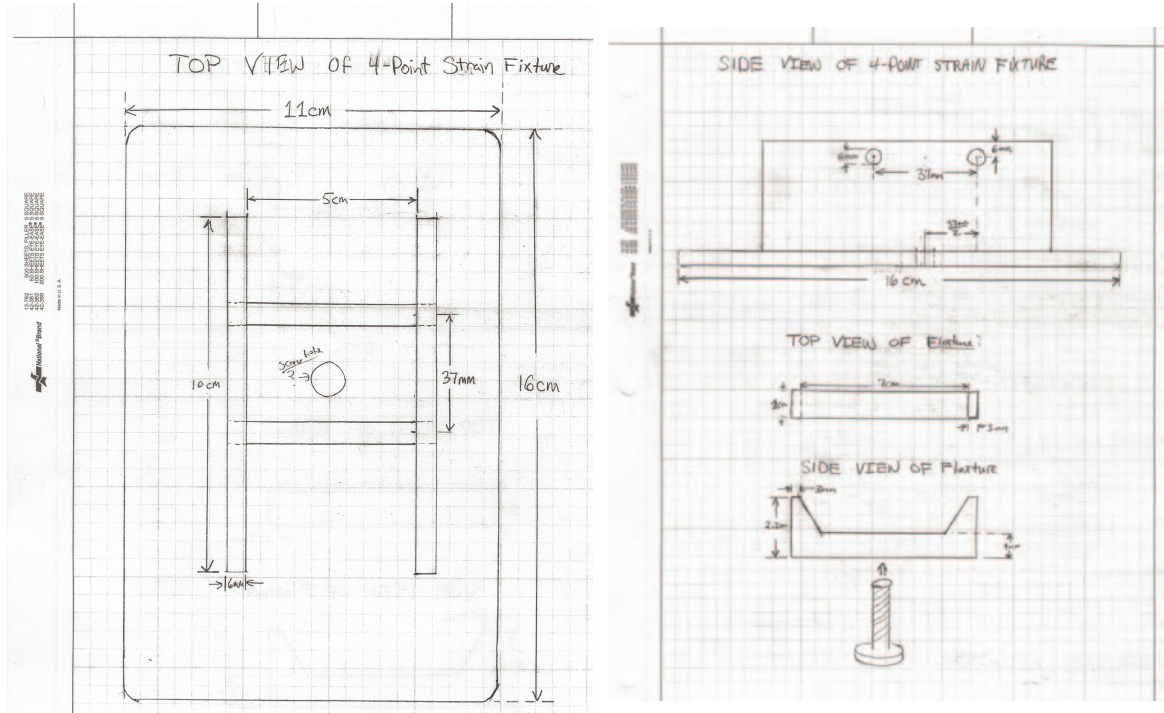


Figure B.1 Four Point Strain Fixture

Pertinent parameters of the InVia Raman Spectrometer for the 514-nm and 325-nm excitations sources are shown in Figures B.2 and B.3.

	A	B	C	D	E	F	G	H	I	J
		Pixel	nm	Abs. cm-1	Grt. Ang.	Deg.	to incident	to exit	eV	mm
1	Chip edge	-288	528.228894	18931.8741						
2	Centre	0	541.851141	18455.25232	0.529230231	30.32265861	45.32265861	15.32265861	2.346744442	-6.336
3	Edge	288	555.379162	18005.71637					2.287746736	0
4	Grating	1800	541.8382395	18453.84715		* SHOULD NOT EXCEED 75 deg			2.232021441	6.336
5	Include angle	30	0.523538775							12.672
6	Wavelength	541.8511	514	<--enter excitation wavelength						
7	Focal length	250								
8	Number of pixels	576		enter static grating center----->	1000	cm-1 shift				
9	Pixel size	0.022								
10	Slit size	0.015								
11	Order	1								
12	Slit focus length	150								
13	Input NA	0.06								
14	F/#	8.333333								
15	Beam width (mm)	10								
16	Footprint on grating	25.8042	<--SHOULD NOT EXCEED 60mm							
17	Edge	287	555.3323828	18007.2337	-1.586738638					
18	Edge	-287	528.2763163	18329.48784	1.639774313					
19										
20										
21										
22										
23	Spectral performance	cm-1	nm	eV						
24	Range	325.4704	27.15027803	0.11472300						
25	cm-1/pixel	1.60672	0.047135899	0.000199172						
26	cm-1/Spot image	1.825818	0.053563522	0.000226332						
27	Grating limited resolution	0.400489	0.011758731							
28										
29	Raman spectral window	Center	-289	289						
30	514	1000	524.07	1449.54						
31										
32										
33	Extended Scan	FROM	TO	Exposure Time (secs)						
34	Scan information	50	3600.00	10.00						
35	Range	3550.00								
36	Average dispersion (cm-1/pixel)	1.60672								
37	Number of data points	2209.471								
38	Scan rate (cm-1/sec)	71.9								
39	Total acquisition time (secs)	49.4								

Figure B.2 Parameters of InVia Raman spectrometer configured for the 514-nm excitation source

	A	B	C	D	E	F	G	H	I	J
		Pixel	nm	Abs. cm-1	Grt. Ang.	Deg.	to incident	to exit	eV	mm
1	Chip edge	-288	325.4881011	30723.08331						
2	Centre	0	335.9173127	23759.23077	0.430494936	24.65554291	39.65554291	9.655542912	3.59439005	-6.336
3	Edge	288	346.3018101	29876.55215					3.630248018	0
4	Grating	2400	335.9524586	29765.02784		* SHOULD NOT EXCEED 75 deg			3.579591192	6.336
5	Include angle	30	0.523538775							12.672
6	Wavelength	335.9173	325	<--enter excitation wavelength						
7	Focal length	250								
8	Number of pixels	576		enter static grating center----->	1000	cm-1 shift				
9	Pixel size	0.022								
10	Slit size	0.015								
11	Order	1								
12	Slit focus length	150								
13	Input NA	0.06								
14	F/#	8.333333								
15	Beam width (mm)	10								
16	Footprint on grating	23.3832	<--SHOULD NOT EXCEED 60mm							
17	Edge	287	346.3656554	29879.56065	-2.938514759					
18	Edge	-287	325.5243682	30719.65641	3.422399495					
19										
20										
21										
22										
23	Spectral performance	cm-1	nm	eV						
24	Range	1945.527	20.81351017	0.223838867						
25	cm-1/pixel	3.205776	0.036134566	0.000397394						
26	cm-1/Spot image	3.642928	0.041062007	0.000451684						
27	Grating limited resolution	0.53045	0.005985732							
28										
29	Raman spectral window	Center	-289	289						
30	325	1000	46.14	1932.67						
31										
32										
33	Extended Scan	FROM	TO	Exposure Time (secs)						
34	Scan information	50	3600.00	10.00						
35	Range	3550.00								
36	Average dispersion (cm-1/pixel)	3.205776								
37	Number of data points	1107.376								
38	Scan rate (cm-1/sec)	117.5								
39	Total acquisition time (secs)	30.2								

Figure B.3 Parameters of InVia Raman spectrometer configured for the 325-nm excitation source

Appendix C. Matlab Code

The following is a list of the Matlabs programs used for modeling characteristics of the SiC samples and for spectral analysis of the Raman data.

C.1 Resistivity Program

```
%*****
% Matlab code to determine carrier concentration and the resistivity ranges
in
% n-type 6H-SiC doped with N 109418 dopants/cm3
%*****
% Version 1.00
% Date: 5 NOV 2004
%
% Authors: Chris Zingarelli (1), and Michael Marciniak (2) Capt Kladitis
(3)
% (2) AFIT/ENG, michael.marciniak@afit.edu, (937) 255-3636 x 4529
%
% References:
% [1] Wolfe, Holnyak, and Stillman, Physical Properties of Semiconduc-
tors
%
% [2] Capt Paul E. Kladitis, PhD., Air Force Institute of Technology,
% EENG 596 Integrated Circuit Technology class notes.
%
% [3] M. Levinshtein, et al., Properties of Advanced Semiconductor Ma-
terials
% GaN, AlN, InN, BN, SiC, SiGe, 2001
clear
clc
k=1.38066e-23; % (J/K) Boltzmann's constant
h=6.62607e-34; % (J-s) Planck's const.
me=9.1094e-31; % (kg) mass of an electron
q=1.60218e-19; % (C) elementary charge
% 6H-SiC constants @ 300K from [3]
T=300; % (K)
Nd=0; Ed=0
Na=0; Ea=0
mn_t=0.42*me % transvers effective electron mass
% mn_l=2.0 % longitudinal effective electron mass
```

```

mp=1; %effective hole mass
Eg0=3.0eV; a=6.5e-4; b=1200;
Eg=Eg0-a*T942/(T+b); %varshney equation
options=foptions;
disp('Ef=Ef-Ev')
Ef=fzero('KFeqns',[0 Eg],[],Nd,Ed,Na,Ea,Eg,T,mn_t,mp,N)

% % Authors: Chris Zingarelli (1), and Michael Marciniak (2) Capt Kla-
diti (3)
%KFeqns.m
%This funtion is called by 6H_Si_resitivity
function F=Keqns(Ef,Nd,Ed,Na,Ea,Eg,T,mn_t,mp,N);
k=1.38066e-23; %(J/K) boltzmans constant
h=6.62607e-34; %(J-s) planks const.
q=1.60218e23; %(C) elementaty charge
Ev=0;
Ec=Eg;
Nc=1.73E16*T94(3/2); %cm94-3
Nv=4.8E15*T94(3/2); %cm94-3
n=Nc*exp((Ef-Ec)/(k*q)/T);
p=Nv*exp((Ev-Ef)/(k*q)/T);
Naa=Na./(1+4*exp((Ev+Ea-Ef)/(k*q)/T));
Ndd=Nd./(1+2*exp((Ef-(Ec-Ed))/(k*q)/T));
F=p-n+Ndd-Naa;

```

C.2 Transmission Program

```

%%%%%%%%%%%%%%%%%%%%%%%%%%%%%%%%%%%%%%%%%%%%%%%%%%%%%%%%%%%%%%%%%%%%%%%%
% Plots the Transmission curves for 6H and 3C SiC
% By Chris Zingarelli
%%%%%%%%%%%%%%%%%%%%%%%%%%%%%%%%%%%%%%%%%%%%%%%%%%%%%%%%%%%%%%%%%%%%%%%%
d=0:.1:1000; %um
%Style
set(0,'DefaultAxesFontName','times new roman')
set(0,'DefaultAxesFontSize',16)
set(0,'DefaultAxesFontWeight','normal')
set(0,'DefaultAxesLineWidth',2)
set(0,'DefaultTextFontName','times new roman')
set(0,'DefaultTextFontSize',16)
set(0,'DefaultTextFontWeight','normal')
set(0,'DefaultLineLineWidth',3)

```

```

% Absorption (um94-1)
alpha_3C_325 = 3600e-4;
alpha_3C_514 = 1.0e-2;
alpha_6H_325 = 5000e-4;
alpha_6H_514 = 2e-3;
%transmission
T_3C_325=exp(-alpha_3C_325*d);
T_3C_514=exp(-alpha_3C_514*d);
T_6H_325=exp(-alpha_6H_325*d);
T_6H_514=exp(-alpha_6H_514*d);
semilogx(d,T_3C_325*100,'-',d,T_3C_514*100,'-',d...
,T_6H_325*100,':',d,T_6H_514*100,'-');
xlabel('SiC film thickness (\mum)');
ylabel('Percent of light transitted');
legend('3C-SiC at 325nm','3C-SiC at 514nm'...
,'6H-SiC at 325nm','6H-SiC at 514nm');

```

C.3 Raman Analysis Program

```

% *****
% Micro-Raman Data Analysis Program (MRDAP)
% *****
% Version 2.10
% Date: 04 January 2005
% Changes: Add 3rd line in window, change tracking, add error analysis,
% use own LSQ code.
% S - folded (symmetry)
% 0 Rayleigh
% 126250 Fresnel lens line
% 766.00 sto x = 1
% 788.00 sto x = 1/3
% 796.00 sto x = 0 (zone-centered)
% 966.00 slo x = 0
% Authors: Jason Foley(1), Chris Zingarelli (2), and Michael Marciniak
(2)
% (1) AFRL/MNMF, jason.foley@eglin.af.mil, (850) 883-0584
% (2) AFIT/ENG, michael.marciniak@afit.edu, (937) 255-3636 x 4529
%
% References:
% [1] Timucin, Dogan A., 2004, "A new computational framework for
% atmospheric and surface remote sensing," Proc. ESTC 2004, B9P1,
% pp. 1-7.

```



```

% [2] Puerta, Julio, and Martin, Pablo, 1981, "Three and four
% generalized Lorentzian approximations for the Voigt
% line shape," Appl. Opt., 20 (22), pp. 3923-3928.
% [3] Foley, Jason R., et al., 2005, "Data reduction for micro-Raman
% spectroscopy experiments," in preparation for submission to J.
% Raman Spectroscopy.
%
function main()
dbstop if error
clc;
clear all;
figure(1);
clf;
% Pseudocode
% 1. Data Import
% a. Baseline data file
% b. Comparative data file(s)
% 2. Plot
% 3. Curve fitting
% a. Gaussian + Lorentzian = Voigt!
%------%
% DATA IMPORT %
%------%
% File selection for data importation (GUI Codelet)
% Set the default directory
cd('D:\Thesis\Zinger\Raman Spectrum');
for idf = 1:2 % Two passes: once for baseline, once for the rest of the data
% Begin GUI codelet to select the data files
dirchange = true;
while dirchange
% Import data... dialog for file name
currdir = cd;
d = dir;
str = {d.name};
isdir = [d.isdir];
dirindices = find(isdir == true);
dialogstr = str;
for ii = 1:length(dirindices)
dialogstr(ii) = {'<',char(str(ii)), '>'};
end
if idf == 1;
% SELECT BASELINE

```

```

[s,v] = listdlg('PromptString','Select BASELINE data file:',...
'SelectionMode','single',...
'ListString',dialogstr);
else
% SELECT DATA FILES (allow multiple files)
[s,v] = listdlg('PromptString','Select COMPARISON data file(s):',...
'SelectionMode','multiple',...
'ListString',dialogstr);
end
if strcmp( '..',char(str(s)))
% Chosen is directory... want to go up a level
lastslash = max(findstr(currdir,'\'));
currdir(lastslash+1:end) = [];
cd(currdir);
elseif strcmp( '.',char(str(s)))
% Chosen is directory... want to refresh current directory... just
% don't allow anything to happen, as it will repopulate at
% beginning of while loop
elseif isdir(s)
% Chosen is subdirectory... append to current path and start over
currdir = [currdir,'\ ',char(str(s))];
cd(currdir);
else
dirchange = false;
end
end
% Read in data file(s)
for iis = 1:length(s)
filename{iis+idf-1} = d(s(iis)).name;
if idf == 1;
disp(sprintf('Baseline file selected: %s.',filename{iis+idf-1}));
else
disp(sprintf('Comparison file selected: %s.',filename{iis+idf-1}));
end
% Open the file
filecontents = importdata(filename{iis+idf-1});
% try
% head = file.textdata;
% filedata = file.data;
% colname = file.colheaders;
% catch
filedata = filecontents;

```

```

% end
[nrows,ncols] = size(filedata);
switch ncols
case 2
% Point scan
scantype{iis+idf-1} = 'point';
Nscans{iis+idf-1} = 1;
data{iis+idf-1} = filedata(end:-1:1,1:2);
case 4
% X
% Long vector of all positions...
xvec{iis+idf-1} = filedata(end:-1:1,1);
% Vector of unique positions (i.e., number of scans in the
% x-direction)
xscanpos{iis+idf-1} = unique(xvec{iis+idf-1});
% Number of x's that comprise each scan
Nxscanpos{iis+idf-1} = length(xscanpos{iis+idf-1});
% Y
% Long vector of all positions...
yvec{iis+idf-1} = filedata(end:-1:1,2);
% Vector of unique positions (i.e., number of scans in the
% y-direction)
yscanpos{iis+idf-1} = unique(yvec{iis+idf-1});
% Number of y's that comprise each scan
Nyscanpos{iis+idf-1} = length(yscanpos{iis+idf-1});
if Nxscanpos{iis+idf-1} == 1
% A vertical line
scantype{iis+idf-1} = 'yline';
elseif Nyscanpos{iis+idf-1} == 1
% A horizontal line
scantype{iis+idf-1} = 'xline';
else
% Area scan (raster, circle, or other)
scantype{iis+idf-1} = 'area';
end
% And in summary...
Nscans{iis+idf-1} = Nxscanpos{iis+idf-1}*Nyscanpos{iis+idf-1};
data{iis+idf-1} = filedata(end:-1:1,3:4);
end
end
end
Ndatafiles = length(data);

```

```

%------%
% END DATA IMPORT %
%------%
% plot(filedata(:,1),filedata(:,2))
% ribbon, waterfall, surf, surfl
% DATA ANALYSIS
% Algorithm for the data analysis
% For each data file...
% 1. Fit Rayleigh peak and calculate the relative wavenumber shift,
% which is stored as dkappaR
% 2. Shift the wavenumber component of the data by this quantity,
% i.e., kappa(i) <- kappa(i) + dkappaR.
%
for iis = 1:Ndatafiles
% For each scan within each data file...
Nds = Nscans{iis};
Nk = length(data{iis}(:,1))/Nds;
for isn = 1:Nds
kscan = data{iis}(1+(isn-1)*Nk:isn*Nk,1);
dscan = data{iis}(1+(isn-1)*Nk:isn*Nk,2);
%
plot(data{2}(:,1),data{2}(:,2));
xlabel('Wavenumber k (m94{-1})');
switch scantype{iis}
case 'point'
% No need to do anything special... just give it x = 0 and
% y = 0 coordinates.
xscan{iis,isn} = 0;
yscan{iis,isn} = 0;
case 'xline'
xscan{iis,isn} = xvec{iis}(1+(isn-1)*Nk,1);
yscan{iis,isn} = yvec{iis}(1,1);
case 'yline'
yscan{iis,isn} = yvec{iis}(1+(isn-1)*Nk,1);
xscan{iis,isn} = xvec{iis}(1,1);
case 'area'
xscan{iis,isn} = xvec{iis}(1+(isn-1)*Nk,1);
yscan{iis,isn} = yvec{iis}(1+(isn-1)*Nk,1);
end
% Scan structure
scanwin = {
% Peak N

```

```

% kmin kmax Npeaks Name Center Sigma RelAmp
-50 50 1 'Rayleigh' 0 1 1 ...
" 0 1 0 ...
" 0 1 0
100 200 1 'STA' 150.5 3 1 ...
" 0 1 0 ...
" 0 1 0
680 860 3 'STO I,x=1' 766.0 2 0.4 ...
'STO II,x=1/3' 788.0 2 1 ...
'STO III,x=0' 796.0 3 0.3
900 1050 1 'SLO' 966.0 2 1 ...
" 0 1 0 ...
" 0 1 0
};
[Nwin,dum] = size(scanwin);
for iw = 1:Nwin;
% LINE WINDOW
kmin = cell2mat(scanwin(iw,1)); % cm94-1
kmax = cell2mat(scanwin(iw,2)); % cm94-1
a = min( find( kscan > kmin ) ); % minimum index
b = max( find( kscan < kmax ) ); % maximum index
Npeaks = cell2mat(scanwin(iw,3)); % Number of peaks
% PLOT DATA
% Add to quick plot
plot(kscan(a:b,1),dscan(a:b,1),'-r');
% LINE DATA
k = kscan(a:b,1); % wavenumber data
d = dscan(a:b,1); % intensity data
% Estimate the noise in the sample from background data, i.e., the
% 10 pts near the ends of the window for this peak
idx = 10;
bgydata = [d(1:idx,1);d(end-idx:end)];
bgkdata = [k(1:idx,1);k(end-idx:end)];
sigmad = std(bgydata);
Rd = 1./sigmad;
% Also, estimate the background from these points
bgline = polyfit(bgkdata,bgydata,1);
bgslope = bgline(1);
bgoffset = bgline(2);
% Estimate the peak values...
pkpos = k(floor(mean(find(d == max(d))))); % finds middle of saturated
zone

```

```

pkA = max(d);
% Set initial guesses and optimization parameters for the
% LINE(s)
params = {}; % Clear the params variable
for iin = 1:Npeaks
    linename = char(scanwin(iw,4 + 4*(iin-1)));
    k0 = cell2mat(scanwin(iw,5 + 4*(iin-1)));
    sigmak0 = cell2mat(scanwin(iw,6 + 4*(iin-1)));
    A0 = pkA*cell2mat(scanwin(iw,7 + 4*(iin-1)));
    params(1+(iin-1)*4:iin*4,:) = {
        % MIN MAX S(1) S(0) SIGMAS0 NAME
        0 1e6 A0 A0 Inf [linename,' amp']
        k0-sigmak0 k0-sigmak0 k0 k0 1 [linename,' k0']
        0 50 5 5 0.5 [linename,' sigmaG']
        0 2 1 1 0.5 [linename,' sigmaL']
    };
end
smin{iis,isn,iw} = cell2mat(params(:,1));
smax{iis,isn,iw} = cell2mat(params(:,2));
Ns = length(smin{iis,isn,iw});
s1{iis,isn,iw} = cell2mat(params(:,3));
s0{iis,isn,iw} = cell2mat(params(:,4));
Rs0{iis,isn,iw} = 1./(cell2mat(params(:,5)));
sname{iis,isn,iw} = char(params(:,6));
% Use MARQUARDT function
lambda0 = 1e-4;
mincurv = 1e-5;
minstep = 8e-7;
maxiter = 100;
lambdamin = 1e-14;
opts = [lambda0 mincurv minstep maxiter lambdamin];
tic;
% [X, info, perf] = marquardt(fun, x0, opts, p1,p2,...)
% [fvec,dfds] = Rayleigh_LSQ_obj_func(s,k,d,Rdvec,s0r,Rs0vec);
disp('Fitting peaks...');
[strace{iis,isn,iw}, info{iis,isn,iw}, perf{iis,isn,iw}] =...
marquardt(@LSQ_obj_func,s1{iis,isn,iw}...
,opts,@linemodel,k,d,Rd,s0{iis,isn,iw},Rs0{iis,isn,iw},smin{iis,isn,iw}...
,smax{iis,isn,iw},Npeaks,bgoffset,bgslope);
shat{iis,isn,iw} = strace{iis,isn,iw}(:,end);
if info{iis,isn,iw}(6) == 1
    disp(sprintf('...fit complete by small gradient in %g s',toc));

```

```

elseif info{iis,isn,iw}(6) == 2
disp(sprintf('...fit complete by small step in %g s',toc));
elseif info{iis,isn,iw}(6) == 3
disp(sprintf('...fit complete by max iterations in %g s',toc));
end
[fhat{iis,isn,iw},Jhat{iis,isn,iw}] = LSQ_obj_func(shat{iis,isn,iw},...
@linemodel,k,d,Rd,s0{iis,isn,iw},Rs0{iis,isn,iw},...
smin{iis,isn,iw},smax{iis,isn,iw},Npeaks,bgoffset,bgslope);
% Perform error analysis
lastwarn(''); % clear all warnings
% Mean square error for a MAP estimator is...
MSE{iis,isn,iw} = inv( Jhat{iis,isn,iw}(1:end-Ns,:).'*Jhat{iis,isn,iw}(1:end-
Ns,:) + ...
diag(Rs0{iis,isn,iw}).'*diag(Rs0{iis,isn,iw} ) );
if 126strcmp(lastwarn,'');
try
disp(sprintf('MSE is not well-conditioned: %g',cond(MSE)));
catch
try
MSE{iis,isn,iw} = pinv( Jhat{iis,isn,iw}(1:end-Ns,:).'*Jhat{iis,isn,iw}(1:end-
Ns,:) + ...
diag(Rs0{iis,isn,iw}).'*diag(Rs0{iis,isn,iw} ) );
catch
MSE{iis,isn,iw} = zeros(Ns,Ns);
end
end
end
scaled_covariance{iis,isn,iw} = MSE{iis,isn,iw};
sigmashat{iis,isn,iw} = diag(sqrt(MSE{iis,isn,iw}));
sigmashat{iis,isn,iw}(find(sigmashat{iis,isn,iw}==0),1) = eps;
for is = 1:Ns;
scaled_covariance{iis,isn,iw}(is,:) = ...
scaled_covariance{iis,isn,iw}(is,:)/sigmashat{iis,isn,iw}(is);
scaled_covariance{iis,isn,iw}(:,is) = ...
scaled_covariance{iis,isn,iw}(:,is)/sigmashat{iis,isn,iw}(is);
end
% Report estimation results
for is = 1:Ns
disp(sprintf('%s = %g +/- %g; s(1) = %g.',deblank(sname{iis,isn,iw}(is,:)),...
shat{iis,isn,iw}(is),sigmashat{iis,isn,iw}(is),s1{iis,isn,iw}(is)));
end
if iw == 1;

```

```

% 2. Shift the wavenumber component of the data by this quantity,
% i.e., kappa(i) <- kappa(i) + dkappaR.
dkappaR{iis,isn,iw} = shat{iis,isn,iw}(2,1);
kscan = kscan - dkappaR{iis,isn,iw}; % reloads each scan, so this is safe
end
end
end
end
%
% SAVE RESULTS
for iis = 2:Ndatafiles
% SAVE TO DATA FILE
Nds = Nscans{iis};
% Find the starting index of the file extension
strstart = findstr(filename{iis},'.');
% Replace the file extension with a *.DAT file extension
datfilename = [filename{iis}(1:strstart),'dat'];
% Write the header, which contains:
% Line 1) the baseline data filename
fid = fopen(datfilename,'w');
HeaderString = ['Baseline data file: ',filename{1}];
fprintf(fid,'%s\n',HeaderString);
fprintf(fid,'\n');
% Line 2) the column headers
DataColumnHeaders{1} = 'x';
DataColumnHeaders{2} = 'y';
count = 3;
for iw = 1:Nwin;
Ns = length(smin{1,1,iw});
for is = 1:Ns
DataColumnHeaders{count} = deblank(sname{1,1,iw}(is,:));
count = count + 1;
end
end
%
for ilf = 1:(length(DataColumnHeaders)-1)
fprintf(fid,'%s, ',DataColumnHeaders{ilf});
end
fprintf(fid,'%s',DataColumnHeaders{ilf+1}); % don't need a comma
fprintf(fid,'\n');
for isn = 1:Nds
DataColumnValues(1) = xscan{iis,isn};

```



```

DataColumnValues(2) = yscan{iis,isn};
count = 3;
for iw = 1:Nwin;
Ns = length(smin{iis,isn,iw});
for is = 1:Ns
DataColumnValues(count) = shat{iis,isn,iw}(is,:);
count = count + 1;
end
end
for idv = 1:length(DataColumnValues)-1
fprintf(fid,'%g, ',DataColumnValues(idv));
end
fprintf(fid,'%g\n',DataColumnValues(end));
end % Loop over scans
fclose(fid);
edit(datfilename);
end
dbc clear all
keyboard
return
% *****
% #####
% LEAST SQUARES OBJECTIVE FUNCTION V 2.0
%
function [fvec,dfds] = LSQ_obj_func(s,func,k,d,Rdvec,s0,Rs0vec,...
smin,smax,Npeaks,bgoffset,bgslope);
% Bayesian maximum a posteriori (LSBMAP) vectorized objective func-
tion
% This function is the objective for the minimizer used to find the
% parameters for the Raman lines that match the provided data.
% X - Unknown optimization parameters
% K - Wavenumber coordinates
% Y - Spectral intensity data
% Input parameters
%
% Output parameters
% fvec : vectorized pdf of model with respect to the data
Nd = length(d);
Ns = length(s);
fvec = zeros(Ns + Nd,1);
dfds = zeros(Nd+Ns,Ns);
% M = Misfit function over all data sets

```

```

% This hold since we assume the experiments are uncorrelated; the
% off-diagonal terms between subsequent experiments are identically zero.
[y0,r] = feval(func,s,k,d,Npeaks,bgoffset,bgslope);
fvec(1:Nd,1) = Rdvec.*r;
% S = Preference function
Ns = length(s);
method = 'pdp';
switch method
case 'normprior'
% Normal (Gaussian) prior
fvec(Nd+1:Nd+Ns,1) = Rs0vec.*(s - s0);
case 'pdp'
% Partially diffuse prior
for is = 1:Ns
if (Rs0vec(is) == 0)
fvec(Nd+is,1) = 0;
else
sigmas(is) = 1./Rs0vec(is);
C = 1/(smax(is) - smin(is) + sqrt(2*pi)*sigmas(is));
if s(is) < smin(is)
fvec(Nd+is,1) = log(C) - 0.5*((s(is)-smin(is))^2)/(sigmas(is)^2);
dfds(Nd+is,is) = -((s(is)-smin(is)))/(sigmas(is)^2);
elseif s(is) > smax(is)
fvec(Nd+is,1) = log(C) - 0.5*((s(is)-smax(is))^2)/(sigmas(is)^2);
dfds(Nd+is,is) = -((s(is)-smax(is)))/(sigmas(is)^2);
else % s on interval (smin,smax)
fvec(Nd+is,1) = log(C);
dfds(Nd+is,is) = 0;
end
end
end
end
if nargout > 1
for is = 1:Ns
sp = s;
eps_s = 0.0001;
if sp(is,1) == 0;
ds = eps;
else
ds = eps_s*sp(is,1);
end
sp(is,1) = sp(is,1) + ds;

```

```

[yp,rp] = feval(func,sp,k,d,Npeaks,bgoffset,bgslope);
dfds(1:Nd,is) = Rdvec.*(yp - y0)/ds;
end
end
%
return
#####
#####
function [y,r] = linemodel(s,k,d,Npeaks,bgoffset,bgslope);
% This function calculates the intensity profile of an arbitrary number of
% peaks (given the parameters S) over the wavenumber range specified by
% K. The residual (R) is also calculated by this code given the data
% vector D.
% Be sure to deal the estimated parameters into the right place
% s = [
% A % Nth peak amplitude
% k0 % Nth peak center
% sigmaG % Nth peak Gaussian width
% sigmaL % Nth peak Lorentzian width
%
% 0 % Baseline slope
% 0.05*max(ycomp{iis}) % Baseline offset
% ];
% Superposition of each of the spectral lines...
for Ni = 1:Npeaks
A = s(4*(Ni-1)+1);
k0 = s(4*(Ni-1)+2);
sigmaG = s(4*(Ni-1)+3);
sigmaL = s(4*(Ni-1)+4);
linei = voigt(k,k0,sigmaG,sigmaL,A);
lines(:,Ni) = linei(:);
end
% ...and the linear model of the background...
background = bgslope.*k + bgoffset;
% ...gives the net intensity distribution
y = sum(lines,2) + background(:);
% Apply a saturation filter to both the data and the Rayleigh line
satvalue = 90e3; % 75,000 counts
y( find( y > satvalue ) ) = satvalue;
d( find( d > satvalue ) ) = satvalue;
% Calculate the residual of the model with respect to the theory
r = ( y - d(:) );

```



```

% mu = opts(1) * max(A0(i,i)) with A0 = J(x0)'*J(x0)
% opts(2:4) used in stopping criteria:
% ||F'||inf <= opts(2) or
% ||dx||2 <= opts(3)*(opts(3) + ||x||2) or
% no. of iteration steps exceeds opts(4) .
% opts(5) lower bound on mu:
% mu = opts(5) * max(A(i,i)) with A = J(x)'*J(x)
% Default opts = [1e-3 1e-4 1e-8 100 1e-14]
% If the input opts has less than 5 elements, it is
% augmented by the default values.
% p1,p2,.. are passed directly to the function FUN .
%
% Output parameters
% X : If perf is present, then array, holding the iterates
% columnwise. Otherwise, computed solution vector.
% info : Performance information, vector with 6 elements:
% info(1:4) = final values of
% [F(x) ||F'||inf ||dx||2 mu/max(A(i,i))] ,
% where A = J(x)'*J(x) .
% info(5) = no. of iteration steps
% info(6) = 1 : Stopped by small gradient
% 2 : Stopped by small x-step
% 3 : No. of iteration steps exceeded
% -1 : x is not a real valued vector
% -2 : f is not a real valued column vector
% -3 : J is not a real valued matrix
% -4 : Dimension mismatch in x, f, J
% -5 : Overflow during computation
% perf : Array, holding
% perf(1,:) = values of F(x)
% perf(2,:) = values of || F'(x) ||inf
% perf(3,:) = mu-values.
%
% Method
% Gauss-Newton with Levenberg-Marquardt damping, see eg
% H.B. Nielsen, "Damping parameter in Marquardt's method",
% IMM-REP-1999-05, IMM, DTU, April 1999.
% Version 04.05.18. hbn(a)imm.dtu.dk
% Check parameters and function call
if nargin < 3, opts = []; end
opts = checkopts(opts, [1e-3 1e-4 1e-8 100 1e-14]);
if nargin < 2, stop = -1;

```

```

else
[stop x n] = checkx(x0);
if 126stop, [stop F f J] = checkfJ(fun,x0,varargin{:}); end
end
if 126stop
g = J'*f; ng = norm(g,inf); A = J'*J;
if isinf(ng) | isinf(norm(A(:),inf)), stop = -5; end
else
F = NaN; ng = NaN;
end
if stop
X = x0; perf = []; info = [F ng 0 opts(1) 0 stop];
return
end
% Finish initialization
mu = opts(1) * max(diag(A)); kmax = opts(4);
Trace = nargout > 2;
if Trace
X = repmat(x,1,kmax+1);
perf = repmat([F; ng; mu],1,kmax+1);
end
k = 1; nu = 2; nh = 0; stop = 0;
% Iterate
while 126stop
if ng <= opts(2), stop = 1;
else
mu = max(mu, opts(5)*max(diag(A)));
[h mu] = geth(A,g,mu);
nh = norm(h); nx = opts(3) + norm(x);
if nh <= opts(3)*nx, stop = 2; end
end
if 126stop
xnew = x + h; h = xnew - x; dL = (h'*(mu*h - g))/2;
[stop Fn fn Jn] = checkfJ(fun, xnew, varargin{:});
if 126stop
k = k + 1; dF = F - Fn;
if Trace
X(:,k) = xnew; perf(:,k) = [Fn norm(Jn'*fn,inf) mu]'; end
if (dL > 0) & (dF > 0) % Update x and modify mu
x = xnew; F = Fn; J = Jn; f = fn;
A = J'*J; g = J'*f; ng = norm(g,inf);
mu = mu * max(1/3, 1 - (2*dF/dL - 1)^943); nu = 2;

```

```

else % Same x, increase mu
mu = mu*nu; nu = 2*nu;
end
if k > kmax, stop = 3;
elseif isinf(ng) | isinf(norm(A(:),inf)), stop = -5; end
end
end
% Set return values
if Trace
X = X(:,1:k); perf = perf(:,1:k);
else, X = x; end
if stop < 0, F = NaN; ng = NaN; end
info = [F ng nh mu/max(diag(A)) k-1 stop];
return
%%%%%%%%%%%%%%%%%%%%%%%%%%%%%%%%%%%%%%%%%%%%%%%%%%%%%%%%%%%%%%%%%%%%%%%%%%
function opts = checkopts(opts, default)
%CHECKOPTS Replace illegal values by default values.
% Version 04.01.25. hbn@imm.dtu.dk
a = default; la = length(a); lo = length(opts);
for i = 1 : min(la,lo)
oi = opts(i);
if isreal(oi) & 126isinf(oi) & 126isnan(oi) & oi > 0
a(i) = opts(i);
end
end
if lo > la, a = [a 1]; end % for linesearch purpose
opts = a;
return
%%%%%%%%%%%%%%%%%%%%%%%%%%%%%%%%%%%%%%%%%%%%%%%%%%%%%%%%%%%%%%%%%%%%%%%%%%
function [err, x,n] = checkx(x0)
%CHECKX Check vector
% Version 04.01.25. hbn@imm.dtu.dk
err = 0; sx = size(x0); n = max(sx);
if (min(sx) 126= 1) | 126isreal(x0) | any(isnan(x0(:))) | isinf(norm(x0(:)))
err = -1; x = [];
else
x = x0(:);
end
return
%%%%%%%%%%%%%%%%%%%%%%%%%%%%%%%%%%%%%%%%%%%%%%%%%%%%%%%%%%%%%%%%%%%%%%%%%%
function [err, F,f,J] = checkfJ(fun,x,varargin)

```



```

%CHECKFJ Check Matlab function which is called by a
% nonlinear least squares solver.
% Version 04.01.25. hbn@imm.dtu.dk
err = 0; F = NaN; n = length(x);
if nargin > 3 % Check f and J
[f J] = feval(fun,x,varargin{:});
sf = size(f); sJ = size(J);
if sf(2) 126= 1 | 126isreal(f) | any(isnan(f(:))) | any(isinf(f(:)))
err = -2; return, end
if 126isreal(J) | any(isnan(J(:))) | any(isinf(J(:)))
err = -3; return, end
if sJ(1) 126= sf(1) | sJ(2) 126= n
err = -4; return, end
else % only check f
f = feval(fun,x,varargin{:});
sf = size(f);
if sf(2) 126= 1 | 126isreal(f) | any(isnan(f(:))) | any(isinf(f(:)))
err = -2; return, end
end
% Objective function
F = (f'*f)/2;
if isinf(F), err = -5; end
return
%%%%%%%%%%%%%%%%%%%%%%%%%%%%%%%%%%%%%%%%%%%%%%%%%%%%%%%%%%%%%%%%%%%%%%%%
function [h, mu] = geth(A,g,mu)
% Solve (Ah + mu*I)h = -g with possible adjustment of mu
% Version 04.01.24. hbn@imm.dtu.dk
% Factorize with check of pos. def.
n = size(A,1); chp = 1;
while chp
[R chp] = chol(A + mu*eye(n));
if chp == 0 % check for near singularity
chp = rcond(R) < 1e-15;
end
if chp, mu = 10*mu; end
end
% Solve (R'*R)h = -g
h = R \ (R' \ (-g));
return
%%%%%%%%%%%%%%%%%%%%%%%%%%%%%%%%%%%%%%%%%%%%%%%%%%%%%%%%%%%%%%%%%%%%%%%%
% % % % %
% TRASH %

```

```

% % % % %
% % % %
% CAN %
% % % %
% #####
% RAYLEIGH OBJECTIVE FUNCTION
%-----
function F = rayobjfunc(x,k,y);
% This function is the objective for the minimizer used to find the
% parameters for the Raman lines that match the provided data.
% X - Unknown optimization parameters
% K - Wavenumber coordinates
% Y - Spectral intensity data
% Deal the estimated parameters into the right place
% s0 = [
% 1 % 1st peak amplitude
% 720 % 1st peak center
% 20 % 1st peak Gaussian width
% 10 % 1st peak Lorentzian width
%
% 0 % Baseline slope
% 0.05*max(ycomp{iis}) % Baseline offset
% ];
% Superposition of the Rayleigh line, modeled as a Voigt peak
A(1) = x(1);
k0(1) = x(2);
sigmaG(1) = x(3);
sigmaL(1) = x(4);
rayline = voigt(k,k0(1),sigmaG(1),sigmaL(1),A(1));
% ...and the linear model of the background...
background = x(5).*k + x(6);
% ...give the net intensity distribution
ytheory = rayline(:) + background(:);
% Apply a saturation filter to both the data and the Rayleigh line
satvalue = 75e3; % 75,000 counts
ytheory( find( ytheory > satvalue ) ) = satvalue;
y( find( y > satvalue ) ) = satvalue;
% Overall figure of merit is then least squares estimate for the fit to
% the data set we have calculated versus the provided data set.
r = y(:) - ytheory;
F = r.*r;
figure(99);

```

```

plot(k,y,'ok',k,ytheory,'-r');
xlabel('Wavenumber (cm94{-1})');
ylabel('Intensity (A.U.)');
pause(0.001);
return
%#####
%#####
function [y,r] = stokestripletmodel(s,k,d);
% This function calculates the intensity profile of a triplet of Stokes
% peaks (given the parameters X) over the wavenumber range specified
by K.
% The residual (R) is also calculated by this code given the D(ata) vector.
% Be sure to deal the estimated parameters into the right place
% s = [
% 1 % 1st peak amplitude
% 720 % 1st peak center
% 20 % 1st peak Gaussian width
% 10 % 1st peak Lorentzian width
%
% 1 % 2nd peak amplitude
% 600 % 2nd peak center
% 10 % 2nd peak Gaussian width
% 10 % 2nd peak Lorentzian width
%
% 1 % 3rd peak amplitude
% 600 % 3rd peak center
% 10 % 3rd peak Gaussian width
% 10 % 3rd peak Lorentzian width
%
% 0 % Baseline slope
% 0.05*max(ycomp{iis}) % Baseline offset
% ];
% Superposition of line 1,...
A(1) = s(1);
k0(1) = s(2);
sigmaG(1) = s(3);
sigmaL(1) = s(4);
line1 = voigt(k,k0(1),sigmaG(1),sigmaL(1),A(1));
% ...line 2,...
A(2) = s(5);
k0(2) = s(6);
sigmaG(2) = s(7);

```

```

sigmaL(2) = s(8);
line2 = voigt(k,k0(2),sigmaG(2),sigmaL(2),A(2));
% ...line 3,...
A(3) = s(9);
k0(3) = s(10);
sigmaG(3) = s(11);
sigmaL(3) = s(12);
line3 = voigt(k,k0(3),sigmaG(3),sigmaL(3),A(3));
% ...and the linear model of the background...
background = s(13).*k + s(14);
% ...give the net intensity distribution
y = line1(:) + line2(:) + line3(:) + background(:);
% Apply a saturation filter to both the data and the Rayleigh line
satvalue = 90e3; % 75,000 counts
y( find( y > satvalue ) ) = satvalue;
d( find( d > satvalue ) ) = satvalue;
% Overall figure of merit is then least squares estimate for the fit to
% the data set we have calculated versus the provided data set.
r = d(:) - y;
plot(k,d,'ok',k,y,'-r');
xlabel('Wavenumber (cm94{-1})');
ylabel('Intensity (A.U.)');
pause(0.001);
return
#####
#####
function [y,r] = raymodel(s,k,d);
% This function calculates the intensity profile of the Rayleigh peak (given
% the parameters X) over the wavenumber range specified by K. The
residual
% (R) is also calculated by this code given the DATA vector.
% Be sure to deal the estimated parameters into the right place
% s = [
% 1 % 1st peak amplitude
% 720 % 1st peak center
% 20 % 1st peak Gaussian width
% 10 % 1st peak Lorentzian width
%
% 0 % Baseline slope
% 0.05*max(ycomp{iis}) % Baseline offset
% ];
% Superposition of the Rayleigh line, modeled as a Voigt peak

```

```

A(1) = s(1);
k0(1) = s(2);
sigmaG(1) = s(3);
sigmaL(1) = s(4);
rayline = voigt(k,k0(1),sigmaG(1),sigmaL(1),A(1));
% ...and the linear model of the background...
background = s(5).*k + s(6);
% ...give the net intensity distribution
y = rayline(:) + background(:);
% Apply a saturation filter to both the data and the Rayleigh line
satvalue = 75e3; % 75,000 counts
y( find( y > satvalue ) ) = satvalue;
d( find( d > satvalue ) ) = satvalue;
% Overall figure of merit is then least squares estimate for the fit to
% the data set we have calculated versus the provided data set.
r = d(:) - y;
plot(k,d,'ok',k,y,'-r');
xlabel('Wavenumber (cm94{-1})');
ylabel('Intensity (A.U.)');
pause(0.001);
return
%#####
% ERFW (VOIGT OR COMPLEX SCALED ERROR FUNCTION)
%-----
function erfw = erfw(z)
%ERFW Scaled error function for complex inputs
% f = erfw(z) is the scaled error function, also called
% the Faddeeva function, for the elements of z:
% erfw(z) = exp(z942)*(1-erf(z));
% Z may be complex and of any size.
%
% Original erfz code by Godfrey. Accuracy is better than 12
% significant digits.
%
% Usage: f = erfw(z)
%
% References:
% FADDEEVA, V. N., AND THERENT'EV, N. N. Tables of values of the
% function  $w(z) = e^{-Z^2}(1 + 2i/126f126et2 dr)$  for complex argument.
% Gosud. Izdat. Teh.-Teor. Lit., Moscow, 1954; English transl.,
% Pergamon Press, New York, 1961.
% POPPE, G. P. M., and WIJERS, C. M. J., 1990, ACM Trans. Math.

```



```

%ERFZ Error function for complex inputs
% f = erfz(z) is the error function for the elements of z.
% Z may be complex and of any size.
% Accuracy is better than 12 significant digits.
%
% Usage: f = erfz(z)
%
% Ref: Abramowitz & Stegun section 7.1
% equations 7.1.9, 7.1.23, and 7.1.29
%
% Tested under version 5.3.1
%
% See also erf, erfc, erfcx, erfinc, erfcore
% Main author Paul Godfrey <pgodfrey@intersil.com>
% Small changes by Peter J. Acklam <jacklam@math.uio.no>
% 09-26-01
error(nargchk(1, 1, nargin));
% quick exit for empty input
if isempty(zz)
f = zz;
return;
end
twopi = 2*pi;
sqrtpi=1.772453850905516027298;
f = zeros(size(zz));
ff=f;
az=abs(zz);
p1=find(az<=8);
p2=find(az> 8);
if 126isempty(p1)
z=zz(p1);
nn = 32;
x = real(z);
y = imag(z);
k1 = 2 / pi * exp(-x.*x);
k2 = exp(-i*2*x.*y);
s1 = erf(x);
s2 = zeros(size(x));
k = x 126= 0; % when x is non-zero
s2(k) = k1(k) ./ (4*x(k)) .* (1 - k2(k));
k = 126k; % when x is zero
s2(k) = i / pi * y(k);

```

```

f = s1 + s2;
k = y/126; % when y is non-zero
xk = x(k);
yk = y(k);
s5 = 0;
for n = 1 : nn
    s3 = exp(-n*n/4) ./ (n*n + 4*xk.*xk);
    s4 = 2*xk - k2(k).*(2*xk.*cosh(n*yk) - i*n*sinh(n*yk));
    s5 = s5 + s3.*s4;
end
s6 = k1(k) .* s5;
f(k) = f(k) + s6;
ff(p1)=f;
end
if 126isempty(p2)
    z=zz(p2);
    pn=find(real(z)<0);
    if 126isempty(pn)
        z(pn)=-z(pn);
    end
    nmax=193;
    s=1;
    y=2*z.*z;
    for n=nmax:-2:1
        s=1-n.*(s./y);
    end
    f=1.0-s.*exp(-z.*z)./(sqrt(pi)*z);
    if 126isempty(pn)
        f(pn)=-f(pn);
    end
    pa=find(real(z)==0);
    % fix along i axis problem
    if 126isempty(pa)
        f(pa)=f(pa)-1;
    end
    ff(p2)=f;
end
f=ff;
return
% %a demo of this function is
% x = -4:0.125:4;
% y = x;

```



```

% kminr kmaxr 788 788 03 'Stokes II [STO,x=1/3] line center wavenum-
ber'
% 0 50 5 4 Inf 'Stokes II [STO,x=1/3] line Gaussian width'
% 0 50 1 1 Inf 'Stokes II [STO,x=1/3] line Lorentzian width'
% % Stokes line III – 796 STO (x = 0)
% 0 1e6 pkAIII pkAIII Inf 'Stokes III [STO,x=0] line amplitude'
% kminr kmaxr 796 796 03 'Stokes III [STO,x=0] line center wavenum-
ber'
% 0 50 5 4 Inf 'Stokes III [STO,x=0] line Gaussian width'
% 0 50 1 1 Inf 'Stokes III [STO,x=0] line Lorentzian width'
% % Background
% -Inf Inf 0 0 1 'Stokes line background slope'
% -Inf Inf bgoff bgoff 0.1*bgoff 'Stokes line background offset'
% };
%
%
%
% smin{iis,isn} = cell2mat(params(:,1));
% smax{iis,isn} = cell2mat(params(:,2));
% Ns = length(smin{iis,isn});
% if iis == 1
% s1{iis,isn} = cell2mat(params(:,3));
% else
% s1{iis,isn} = shat{iis-1};
% end
% s0{iis,isn} = cell2mat(params(:,4));
% Rs0{iis,isn} = 1./(cell2mat(params(:,5)));
% sname{iis,isn} = char(params(:,6));
%
% % Use MARQUARDT function
% tic;
% % [X, info, perf] = marquardt(fun, x0, opts, p1,p2,...)
% % [fvec,dfds] = Rayleigh_LSQ_obj_func(s,k,d,Rdvec,s0r,Rs0vec);
% [strace{iis,isn}, info{iis,isn}, perf{iis,isn}] = marquardt...
(@LSQ_obj_func,s1{iis,isn}...
,opts,@linemodel,k,d,Rd,s0{iis,isn},Rs0{iis,isn},Npeaks);
% toc;
% shat{iis,isn} = strace{iis,isn}(:,end);
% [fhat{iis,isn},Jhat{iis,isn}] = LSQ_obj_func(shat{iis,isn},@linemodel,k,d...
,Rd,s0{iis,isn},Rs0{iis,isn},Npeaks);
% % Perform error analysis
% lastwarn(''); % clear all warnings

```

```

% % Mean square error for a MAP estimator is...
% MSE{iis,isn} = inv( Jhat{iis,isn}(1:end-Nsr,:).'*Jhat{iis,isn}(1:end-Nsr,:)
+ ...
% diag(Rs0{iis,isn}).'*diag(Rs0{iis,isn}) );
% if 126strcmp(lastwarn,"");
% try
% disp(sprintf('MSE is not well-conditioned: %g',cond(MSE)));
% catch
% try
% MSE{iis,isn} = pinv( Jhat{iis,isn}(1:end-Nsr,:).'*Jhat{iis,isn}(1:end-
Nsr,:) + ...
% diag(Rs0{iis,isn}).'*diag(Rs0{iis,isn}) );
% catch
% MSE{iis,isn} = zeros(Ns,Ns);
% end
% end
% end
% scaled_covariance{iis,isn} = MSE{iis,isn};
% sigmashat{iis,isn} = diag(sqrt(MSE{iis,isn}));
% for is = 1:Ns;
% scaled_covariance{iis,isn}(is,:) = scaled_covariance{iis,isn}(is,:)...
/sigmashat{iis,isn}(is);
% scaled_covariance{iis,isn}(:,is) = scaled_covariance{iis,isn}(:,is)...
/sigmashat{iis,isn}(is);
% end
% % Report estimation results
% for is = 1:Ns
% disp(sprintf('%s = %g +/- %g; s(1) = %g.',deblank(sname{iis,isn}(is,:))...
,shat{iis,isn}(is),sigmashat{iis,isn}(is),s1{iis,isn}(is)));
% end
% % _LINE_1__LINE_1__LINE_1__LINE_1__
%
%
%
%
% % Peak centers are in 2 and 6... shift is then shat{1}(2)-shat{2+}(2)
etc.
% kramanshift1{iis,isn} = shat{iis,isn}(2) - shat{1,1}(2);
% disp(sprintf('Shift for 1st peak from scan %g from %s is %g'...
,isn,filename{iis},kramanshift1{iis,isn}));
% kramanshift2{iis,isn} = shat{iis,isn}(6) - shat{1,1}(6);
% disp(sprintf('Shift for 2nd peak from scan %g from %s is %g'...

```

```

,isn,filename{iis},kramanshift2{iis,isn}));
% kramanshift3{iis,isn} = shat{iis,isn}(10) - shat{1,1}(10);
% disp(sprintf('Shift for 3rd peak from scan %g from %s is %g'...
,isn,filename{iis},kramanshift2{iis,isn}));
% disp(' ');
%
%
% % PLOT THE INFORMATION
% switch scantype{iis}
% case 'point'
% % No plots
% case 'xline'
% % PLOT
% Nx = Nxscanpos{iis};
% for ix = 1:Nx
% xx(ix) = xscan{iis,ix};
% raman1(ix) = kramanshift1{iis,ix};
% raman2(ix) = kramanshift2{iis,ix};
% raman3(ix) = kramanshift3{iis,ix};
% end
% figure;
% plot(xx,raman1,xx,raman2,xx,raman3);
% xlabel('x (\it\mu\rmm)');
% ylabel('Raman shift (cm94{-1})');
% title(filename{iis},'Interpreter','none');
% case 'yline'
% Ny = Nyscanpos{iis};
% for iy = 1:Ny
% yy(iy) = yscan{iis,iy};
% raman1(iy) = kramanshift1{iis,iy};
% raman2(iy) = kramanshift2{iis,iy};
% raman3(iy) = kramanshift3{iis,iy};
% end
% figure;
% plot(yy,raman1,yy,raman2,yy,raman3);
% xlabel('x (\it\mu\rmm)');
% ylabel('Raman shift (cm94{-1})');
% title(filename{iis},'Interpreter','none');
% case 'area'
% Nx = Nxscanpos{iis};
% Ny = Nyscanpos{iis};
% for ix = 1:Nx

```

```

% for iy = 1:Ny
% isn = iy + (ix-1)*Ny
% xx(iy,ix) = xscan{iis,isn};
% yy(iy,ix) = yscan{iis,isn};
% raman1(iy,ix) = kramanshift1{iis,isn};
% raman2(iy,ix) = kramanshift2{iis,isn};
% raman3(iy,ix) = kramanshift3{iis,isn};
% end
% end
% figure;
% surf(xx,yy,raman1);
% xlabel('x (\it\mu\rmm)');
% ylabel('y (\it\mu\rmm)');
% zlabel('Raman shift (cm94{-1})');
% title(filename{iis},'Interpreter','none');
% end

```

Bibliography

- [1.] C. Lee, G. Pezzotti, Y. Okui, and S. Nishino, "Raman microprobe mapping of residual microstresses in 3C-SiC film epitaxial lateral grown on patterned Si (100)," *Applied Surface Science*, vol. 228, pp. 10–16, 2004.
- [2.] P. C. Rounsavall, *Controlled-Stress Large-Area Pulsed Laser Deposition of Yttria Stabilized Zirconia*. PhD thesis, Air Force Institute of Technology, 2003.
- [3.] "Case western reserve university–CWRU." <http://mems.cwrs.edu/SiC>.
- [4.] S. Sridhara, T. Eperjesi, R. Devaty, and W. Choyke., "Penetration depths in the ultraviolet for 4H, 6H and 3C silicon carbide at seven comon laser pumping wavelengths," *Elsevier Science S.A.*, 1999.
- [5.] C. A. Zorman and M. Mehregany, "Silicon carbide for MEMS and NEMS – an overview," *IEEE*, pp. 1109–1114, 2002.
- [6.] J. M. Melzak, "Silicon carbide for RF MEMS," *IEEE MTT-S Digest*, pp. 1629–1632, 2003.
- [7.] M. Mehregany, C. A. Zorman, N. Rajan, and C. H. Wu, "Silicon carbide MEMS for harsh environments," *IEEE*, vol. 86, pp. 1594–1610, August 1998.
- [8.] A. R. Atwell, *Silicon Carbide MEMS Devices for Harsh Enviroments*. PhD thesis, Cornell University, August 2002.
- [9.] P. G. Neudeck, "Silicon carbide electronic devices," *Encyclopedia of Materials-Science and Technology*, pp. pp 8508–8519, 2001.
- [10.] P. G. Neudeck, "SiC technology," 1998. nASA Lewis Research Center, M.S. 77-1, 21000 Brookpark Road, Cleaveland, OH 44135, neudeck@lerc.nasa.gov.
- [11.] D. Nakamura, I. Gunjishima, S. Yamaguchi, T. Ito, A. Okamoto, H. Hodo, S. Onda, and K. Takatori, "Ultra high-quality silicon carbide single crystals," *Nature*, vol. 430, pp. 1009–1012, 2004.
- [12.] N. Rajan and et Al, "Fabrication and testing of micromachined silicon carbide and nickel fuel atomizers for gas turbine engines," *IEEE*, pp. 251–257, 1999.
- [13.] M. Marciniak, "Proposal for micro-raman spectroscopy of SiC," 2004.
- [14.] R. Okojie, "Design considerations for bulk micromachined 6H-SiC high-g piezoresistive accelerometers," *Tech. Digest 15th IEEE Intl. Conf. on MEMS*, pp. 618–622, January 2002.
- [15.] E. Martin, J. Jimenez, and M. Chafai, "Microraman study of crystallographic defects in SiC crystals," *Solid-State Electronics*, vol. 42, pp. 2309–2314, 1998.

- [16.] L. Starman, *Characterization of Residual Stress in Microelectromechanical Systems (MEMS) Devices Using Raman Spectroscopy*. PhD thesis, Air Force Institute of Technology, April 2002.
- [17.] J. R. Ferraro and K. Nakamoto, *Introductory Raman Spectroscopy*. Academic Press, 1994.
- [18.] D. J. Brink, T. Maurice, S. Blanque, H. Kunert, J. Camassel, and J. Pascual, "Depth profiling of high-energy hydrogen-impanted 6H-SiC," *Applied Optics*, vol. 43, no. 6, pp. 1275–1280, 20 February 2004.
- [19.] "What is silicon carbide?," tech. rep., NASA Jet Propulsion Laboratory, January 2003. <http://vshields.jpl.nasa.gov/SiC/CubicHex.html>.
- [20.] S. Sze, *Semiconductor Devices: Physics and Technology*. John Wiley & Sons, 2002.
- [21.] M. E. Zvanut, "Electron paramagnetic resonance of electronic-grade SiC substrates," *Journal of Physics: Condensed Matter*, vol. 16, pp. 1341–1367, 2004.
- [22.] B. El-Kareh, *Fundamentals of Semiconductors Processing Technologies*. Boston: Kluwer Academic, 1995.
- [23.] C. A. Wert and R. M. Thomson, *Physics of Solids*. McGraw-Hill, 1964.
- [24.] R. Madar, "Silicon carbide in contention," *Nature*, vol. 430, pp. 974–975, 2004.
- [25.] D. W. Feldman, J. H. Parker, W. Choyke, and L. Patrick, "Raman scattering in 6H-SiC," *Physical Review*, vol. 170, no. 3, pp. 698–704, 15 June 1968.
- [26.] T. Tomoita, S. Saito, M. Baba, M. Hundhausen, T. Suemoto, and S. Nakashima, "Selective resonance effects of the folded longitudinal phonon modes in the Raman spectra of SiC," *Physical Review B*, vol. 62, 15 November 2000.
- [27.] S. Ferrero and et al, "Defect characterization of 4H-SiC wafers for power electronic device applications," January 2003. http://www2.polito.it/research/thinfims/papers/Bo_def.pdf.
- [28.] J. Liu and Y. K. Vohra, "Raman modes of 6H polytype of silicon carbide to ultrahigh pressures: A comparison with silicon and diamond," *Physical review letters*, vol. 72, pp. 4105–4108, 27 June 1994.
- [29.] S. Rohmfeld, M. Hundhausen, and L. Ley, "Raman scattering in polycrystalline 3C-SiC: Influence of stacking faults," *Physical Review B*, vol. 58, no. 15, pp. 9858–9862, 15 October 1998.
- [30.] K. Bradley, J. Foley, A. Cash, S. Roberson, A. Beliveau, and R. Okojie, "Testing and analysis of piezoresistive signals from silicon carbide MEMS accelerometers with application to penetration fuzing," Air Force Research Labs, Applied Research Associates, NASA Glenn Research Center, NDIA Fuze Conference-Charlotte, NC, 2004.

- [31.] J. Foley. Personal Correspondance, Air Force Munitions Labratory; Muntions Directorate Fuzes Branch (AFRL/MNMF), Jason.Foley@eglin.af.mil.
- [32.] Cree Inc, *Silicon Carbide Substrates*, 1998. Product Specifications: 4H Silicon Carbide (n/p-type, Semi-Insulating); 6H Silicon Carbide (n/p-type).
- [33.] M. E. Levinshtein, S. L. Rumyantsev, and M. S. Shur, *Properties of Advanced Semiconductor Material: GaN, AlN, InN, BN, SiC, SiGe*. John Wiley & Sons, 2001.
- [34.] Wolfe, Holonyak, and Stillman, *Physical Properties of Semiconductors*.
- [35.] P. E. Kladitis, "EENG 596 intergrated ciruit technology lecture notes," Fall 2003. Midterm Soln. to Problem #3.
- [36.] J. Melzak. Flx Microweb site: www.flxmicro.com.
- [37.] [Http://Www.Cp.Umist.Ac.Uk/CPC/Facilities/Electron](http://Www.Cp.Umist.Ac.Uk/CPC/Facilities/Electron), "Corrosion & protection centre: Research facilities:scanning electron microscopy."
- [38.] Z. Corporation, *NewView 5000 Operating Manual OMP-0423H*, 2002.
- [39.] S. Ness, "Stress analysis of silicon carbide microelectromechanical systems (MEMS) devices using raman spectroscopy," Master's thesis, Air Force Institute of Technology, March 2003.
- [40.] V. Micro-Measurements, *Model P3 Strain Indicator and Recorder: Instruction Manual*. Vishay Micro-Measurements P.O. Box 27777 Raleigh, NC 27611 USA Telephone: (919) 365-3800 Facsimile: (919) 365-3945 www.vishaymg.com micro-measurements@vishay.com, September 2003.
- [41.] W. Sharp, B. Yuan, R. Vaidyanathan, and R. Edwards, "Measurements of young's modulus, poisson's ratio, and the tensile strength of polysilicon," *Proceedings of the Tenth Annual Workshop of Micro Electro Mechanical Systems*, pp. 424–429, 1997.
- [42.] J. S. Milton and J. C. Arnold, *Introduction to Probability and Statistics Principles and Application for Engineering and the Computing Sciences*. New York, New York: McGraw Hill, 2003.
- [43.] D. Petrosky, "Personal correspondence." Suggestion that Nuclear Radiation could relieve stress in SiC, 2004.
- [44.] H. R. Philipp and E. Taft, *Silicon Carbide – a High Temperature Semiconductor*. Oxford: Pergamon Press, 1960.
- [45.] E. I. Radovanova, *Ph.D. Thesis*. PhD thesis, The Ioffe Institute of Russian Academy of Science, 1970.
- [46.] L. Patrick and W. Choyke, "Optical absorption in n-type cubic SiC," *Physical Review*, vol. 186, pp. 775–777, 15 October 1969.
- [47.] C. Persson and U. Lindefelt, "Relativistic band structure calculation of cubic and hexagonal SiC polytypes," *J. Appl. Phys.*, pp. 5496–5508., 1997.

REPORT DOCUMENTATION PAGE					<i>Form Approved OMB No. 0704-0188</i>	
The public reporting burden for this collection of information is estimated to average 1 hour per response, including the time for reviewing instructions, searching existing data sources, gathering and maintaining the data needed, and completing and reviewing the collection of information. Send comments regarding this burden estimate or any other aspect of this collection of information, including suggestions for reducing the burden, to the Department of Defense, Executive Services and Communications Directorate (0704-0188). Respondents should be aware that notwithstanding any other provision of law, no person shall be subject to any penalty for failing to comply with a collection of information if it does not display a currently valid OMB control number.						
PLEASE DO NOT RETURN YOUR FORM TO THE ABOVE ORGANIZATION.						
1. REPORT DATE (DD-MM-YYYY) 22-03-2005		2. REPORT TYPE Master's Thesis			3. DATES COVERED (From - To) Feb 2004-Mar 2005	
4. TITLE AND SUBTITLE Detection of Residual Stress in SiC MEMS Using μ -Raman Spectroscopy					5a. CONTRACT NUMBER	
					5b. GRANT NUMBER	
					5c. PROGRAM ELEMENT NUMBER	
					5d. PROJECT NUMBER	
6. AUTHOR(S) Zingarelli, John, C. 1Lt USAF					5e. TASK NUMBER	
					5f. WORK UNIT NUMBER	
7. PERFORMING ORGANIZATION NAME(S) AND ADDRESS(ES) Air Force Institute of Technology, Graduate School of Engineering and Management (AFIT/EN), 2950 Hobson Way, WPAFB OH 45433-7765.					8. PERFORMING ORGANIZATION REPORT NUMBER AFIT/GEO/ENP/05-06	
9. SPONSORING/MONITORING AGENCY NAME(S) AND ADDRESS(ES) Jason R. Foley, Mechanical Engineer AFRL/MNMF 306 W. Eglin Blvd., Bldg 432 Eglin AFB, FL 32542-5430					10. SPONSOR/MONITOR'S ACRONYM(S)	
					11. SPONSOR/MONITOR'S REPORT NUMBER(S)	
12. DISTRIBUTION/AVAILABILITY STATEMENT APPROVED FOR PUBLIC RELEASE; DISTRIBUTION UNLIMITED						
13. SUPPLEMENTARY NOTES						
14. ABSTRACT Micro-Raman (μ -Raman) spectroscopy is used to measure residual stress in two silicon carbide (SiC) poly-types: single-crystal, hexagonally symmetric 6H-SiC, and polycrystalline, cubic 3C-SiC thin films deposited on Si substrates. Both are used in micro-electrical-mechanical systems (MEMS) devices. By employing an incorporated piezoelectric stage with submicron positioning capabilities along with the Raman spectral acquisition, spatial scans are performed to reveal areas in the 6H-SiC MEMS structures that contain residual stress. Shifts in the transverse optical (TO) Stokes peaks of up to 2 cm^{-1} are correlated to the material strain induced by the MEMS fabrication process through the development of phonon deformation potential curves for this material. The 3C-SiC films, with thicknesses ranging from $1.5\text{--}5\text{ }\mu\text{m}$, are deposited by CVD on (100) Si substrates and are also investigated to determine their residual stress. An ultraviolet excitation source ($\nu = 325\text{ nm}$, $h\nu = 3.82\text{ eV}$) was determined to be more effective for the detection of Raman shifts in these thin films than the 514-nm source, since the absorption coefficient in SiC at 300 K at 325 nm is 3660 cm^{-1} , while that at 514 nm is less than 100 cm^{-1} .						
15. SUBJECT TERMS Micro-electro-mechanical Systems, MEMS, Raman Spectroscopy, Silicon Carbide, 3C-SiC, 6H-SiC, Residual Stress						
16. SECURITY CLASSIFICATION OF:			17. LIMITATION OF ABSTRACT	18. NUMBER OF PAGES	19a. NAME OF RESPONSIBLE PERSON	
a. REPORT	b. ABSTRACT	c. THIS PAGE			Marciniak, Michael A Civ AFIT/ENP	
U	U	U	UU	137	19b. TELEPHONE NUMBER (Include area code) (937)255-3636 ext.4529	